

**CHARACTERIZATION OF A THIN HARD LAYER ON  
A SOFT SUBSTRATE – THEORY AND ITS  
APPLICATION ON A SURFACE-MODIFIED PDMS**

by

Dong Hee Lee

A dissertation submitted in partial fulfillment  
of the requirements for the degree of  
Doctor of Philosophy  
(Mechanical Engineering)  
in The University of Michigan  
2008

Doctoral Committee:

Professor James R. Barber, Co-Chair  
Professor Michael D. Thouless, Co-Chair  
Professor Nicolas Triantafyllidis  
Associate Professor Wei Lu  
Associate Professor Shuichi Takayama

© Dong Hee Lee  

---

All Rights Reserved  
2008

To my family

## ACKNOWLEDGEMENTS

First and foremost, I would like to thank my advisors Professor Barber and Professor Thouless for their insight, expertise, and guidance throughout my Ph.D course. I would like to thank Professor Triantafyllidis for his advice and guidance to solve problems in my dissertation. I also appreciate many comments and advices from Professor Takayama and Professor Lu.

I would like to thank all people whom I met in Ann Arbor. I also thank Youngju, Jeongseok, Yunju and Hyung-ju from PNU. I would like to thank my brothers, sister and their families for their support. Especially, I would like to thank my elder brother Chunghee for his supports and advices in every ways.

I would like to give my special thank and respect to my wife Eunah. I couldn't make this academic achievement without her support, encouragement, and sacrifices. I also would like to express my love to my beloved daughters, Jisue and Suemin. They are the sources of power to overcome the obstacles in life and research. Finally, I'm forever indebted to my parents Sangwoo Lee and Ahnsoon Han for their endless support and innumerable sacrifices.

## TABLE OF CONTENTS

<b>DEDICATION</b> . . . . .	<b>ii</b>
<b>ACKNOWLEDGEMENTS</b> . . . . .	<b>iii</b>
<b>LIST OF FIGURES</b> . . . . .	<b>vii</b>
<b>LIST OF TABLES</b> . . . . .	<b>xii</b>
<b>ABSTRACT</b> . . . . .	<b>xiii</b>
<b>CHAPTER</b>	
<b>I. INTRODUCTION</b> . . . . .	<b>1</b>
1.1 Motivation . . . . .	1
1.2 Characterization of a modified layer on a substrate . . . . .	4
1.2.1 Characterization of the modified layer by chemical methods . . . . .	4
1.2.2 Characterization of the modified layer using AFM . . . . .	6
1.3 Characterization of a thin layer by Indentation . . . . .	7
1.3.1 Estimation of the local material properties by nanoindentation . . . . .	8
1.3.2 Theoretical studies of indentation . . . . .	10
1.3.3 Numerical analyses of the indentation . . . . .	12
1.3.4 Estimation of the residual stress/strain in thin films by indentation . . . . .	14
1.4 Surface instability–wrinkling . . . . .	15
1.4.1 Experimental techniques to form spontaneous patterns using wrinkles in a thin film . . . . .	15
1.4.2 Patterning wrinkles by mechanical deformation . . . . .	17
1.4.3 Theoretical studies of instability–buckling/wrinkling . . . . .	18
1.5 Organization of the dissertation . . . . .	21
<b>II. SURFACE INSTABILITY OF AN ELASTIC HALF SPACE WITH MATERIAL PROPERTIES VARYING WITH DEPTH</b> . . . . .	<b>24</b>

2.1	Introduction . . . . .	24
2.2	General theory of the instability . . . . .	26
2.2.1	Nature of the loading . . . . .	28
2.2.2	Analysis . . . . .	29
2.2.3	Numerical solution . . . . .	33
2.3	Results . . . . .	35
2.3.1	Convergence and validation . . . . .	35
2.3.2	Graded materials . . . . .	36
2.3.3	Effect of Poisson's ratio . . . . .	41
2.3.4	Thermoelastic wrinkling . . . . .	41
2.4	Conclusions . . . . .	44

**III. ESTIMATION OF THE PROPERTIES OF A THIN HARD LAYER ON A SOFT SUBSTRATE BY INDENTATION . . . . . 45**

3.1	Introduction . . . . .	45
3.2	Indentation into a homogeneous plate on a half space . . . . .	47
3.2.1	Indentation into a plate on an elastic half space without friction / adhesion . . . . .	49
3.2.2	Indentation into a plate bonded to an elastic half space . . . . .	50
3.2.3	Finite element analysis of the indentation into a plate on an elastic substrate . . . . .	52
3.2.4	Estimation of the modulus of the surface-modified layer of PDMS . . . . .	59
3.3	Indentation into an elastic half space with graded material properties . . . . .	61
3.3.1	Indentation by a cylindrical punch . . . . .	61
3.3.2	Indentation by a power-law shaped punch . . . . .	65
3.3.3	Finite-element analysis of the indentation into an elastic half space with power law grading modulus . . . . .	69
3.4	Estimation of the modulus of an oxidized PDMS . . . . .	79
3.4.1	Iterative procedure to determine the modulus of oxidized layer . . . . .	79
3.4.2	Effect of residual strain . . . . .	82
3.5	Conclusions . . . . .	85

**IV. WRINKLING IN A SURFACE-MODIFIED LAYER OF POLY (DIMETHYL-SILOXANE) . . . . . 86**

4.1	Introduction . . . . .	86
4.2	Experimental Methods and Observations . . . . .	87
4.2.1	Producing wrinkles by a compressive load . . . . .	87
4.2.2	Producing wrinkles by tensile loading . . . . .	90
4.3	Wrinkling in a surface-modified layer . . . . .	94
4.3.1	Effect of Poisson's ratio mismatch . . . . .	94

4.3.2	Stresses produced by compressive and tensile loading .	97
4.4	Effect of cracks . . . . .	100
4.4.1	Stress relaxation between cracks . . . . .	101
4.4.2	Stress field induced by crack opening . . . . .	105
4.4.3	Effect of graded modulus . . . . .	108
4.5	Conclusions . . . . .	108
<b>V. CONCLUSIONS AND FUTURE WORK . . . . .</b>		<b>112</b>
5.1	Conclusions . . . . .	112
5.2	Future Work . . . . .	114
<b>APPENDIX . . . . .</b>		<b>115</b>
<b>BIBLIOGRAPHY . . . . .</b>		<b>132</b>

## LIST OF FIGURES

Figure		
1.1	Typical fabrication process of PDMS microchip (Fujii, 2002) . . . . .	2
2.1	Schematic of a half space subjected to a compressive load . . . . .	24
2.2	The graded layer subjected to a compressive load . . . . .	27
2.3	Critical strain and wavelength for a homogeneous layer on a dissimilar substrate. The solid lines are taken from Huang <i>et al.</i> (2005). . . . .	37
2.4	Examples of variable modulus: — exponential grading, - - - error function grading . . . . .	38
2.5	Critical strain and dimensionless wavenumber for exponential grading. The solid line represents a homogeneous layer approximation using Eqs. (2.24) and (2.25). . . . .	39
2.6	Critical strain and dimensionless wavenumber for error function grading. The solid line represents a homogeneous layer approximation using Eqs. (2.24) and (2.25). . . . .	40
2.7	Effect of Poisson's ratio; (○) $\nu = 0$ and uniform, (□) $\nu = 0.49$ and uniform, (◇) Eq. (2.26) with $\nu_0 = 0, \nu_s = 0.49$ . . . . .	42
3.1	Load versus Indentation depth relation for the compliant cantilever ( $k = 0.58$ N/m) indenting on (a) unoxidized and (b) 4-minute oxidized PDMS (Reproduced from Mills <i>et al.</i> (2007)) . . . . .	46
3.2	Possible deformation of a plate by a point force and a rigid indenter . . . . .	48
3.3	Schematic of indentation into a plate on elastic half space. $E$ is the elastic modulus, and $\nu$ is Poisson's ratio. $f$ and $s$ in the subscripts mean the plate and substrate, respectively. $H_f$ is the thickness of the plate. . . . .	49
3.4	Geometry and boundary conditions for the finite element simulation . . . . .	53

3.5	Mesh configuration near the indenter tip . . . . .	54
3.6	Comparison of the load-indentation depth curve between the plate theory and FE simulation; (–) the plate theory, (○) the FE simulation. . . . .	55
3.7	Comparison between the plate theory and the FE simulation with various modulus ratios; (– – –) the plate theory, (—) the FE simulation, $E_f/E_s =$ (○) 10, (□) 100, (◇) 1000. $\nu_f = \nu_s = 0.5$ . . . . .	56
3.8	A sample comparison of the load-indentation depth curve between the modified plate theory and the FE simulation; (– – –) modified plate theory, (–) FE simulation. $E_f/E_s = 100, \nu_f = \nu_s = 0.5$ . . . . .	58
3.9	Effective range of the modified plate theory. The steps near $a/H_f = 0.01$ may be caused by the minimum mesh sizes in the finite element simulation. . . . .	58
3.10	Comparison between the results of the FE simulation and the nanoindentation experiments done by Mills <i>et al.</i> (2007); $E_f/E_s =$ (□) 10, (○) 30, (◇) 40, (△) 50, (+) 100. Solid lines are experimental results. $\nu_f = \nu_s = 0.5$ . . . . .	60
3.11	Graphic model of a simple power law $E = E_0(z/H)^\lambda$ ( $-1 \leq \lambda \leq 1$ ) . . . . .	68
3.12	Schematic of the simple truncation method. The value of the surface modulus ( $E_0$ ) is used for the first layers. This is a non-scaled picture to show the truncation and discretization methods. . . . .	70
3.13	Discretization of the body to apply the graded material properties. Numbers in right side are the ratio of each layer to the total thickness ( $h_i/H_{tot}$ ), where $h_i$ is thickness of $i$ -th layer. This is a non-scaled picture. . . . .	71
3.14	Non-dimensional force-indentation depth relationship for the inverse power law ( $\lambda = -1$ ). The constant truncation method is used for the FE simulation. . . . .	72
3.15	Comparison of the force-indentation depth relationship between the power law and FE simulation. The solid line is the power law and the circular symbols are the results of the FE simulation. $CH = 0.025, E_f/E_s = 100, \nu = 0.5$ . . . . .	73
3.16	Schematic of the quadratic truncation method. This is non-scaled picture to show the truncation method. . . . .	74

3.17	Nondimensional force-indentation depth curves of the quadratic truncation with respect to the length scales; $CH = (\bigcirc) 1.25, (\square) 0.75, (\diamond) 0.25, (\triangle) 0.125,$ and $(+) 0.025. \nu = 0.5$ . . . . .	75
3.18	Comparison of the force-indentation depth relations between the truncation methods; $(\bigcirc)$ the constant truncation, $(\square)$ the quadratic truncation. The bar in each symbol means the errors caused by the power-law fitting. . . . .	75
3.19	Graphic model of the error function. . . . .	76
3.20	Force-Indentation depth curves for the error function; $E_0/E_s = (\bigcirc) 10, (\square) 10^2, (\diamond) 10^3, (\triangle) 10^4$ and $(+) 10^5. CH = 0.025, \nu = 0.5$ . . . . .	77
3.21	Force-Indentation depth relationships for the error function. $CH = (\bigcirc) 0.025, (\square) 0.05, (\diamond) 0.1, (\triangle) 0.5, (\times) 1.0.$ The bar in each symbol means the errors caused by the power-law fitting. . . . .	78
3.22	Comparison of the force-indentation depth relationships between the power law (quadratic truncation) and the error function; $(\bigcirc)$ the error function, $(\square)$ the power law with quadratic truncation. The bar in each symbol means the errors caused by the power-law fitting. . . . .	78
3.23	Dimensionless wavenumbers for error function grading. The solid line represents a homogeneous layer approximation using Eqs. (2.24) and (2.25). . . . .	80
3.24	Flow chart for the iterative procedure to estimate surface modulus and thickness of the oxidized layer of PDMS . . . . .	81
3.25	Estimation of residual strain from the geometry of cracks that is produced by releasing 10 % tensile strain produced by Mills <i>et al.</i> (2007) . . . . .	84
4.1	Surface buckling after relaxation of a 4 % tensile strain imposed during a 40-minute oxidation. The left-hand image is a 2-D projection of the image shown on the right. . . . .	89
4.2	Distribution of the wavelengths produced by compressive loading produced by pre-stretching. At 30-second oxidation, wrinkles were not found. . . . .	89
4.3	Schematic for the process to produce wrinkles on an oxidized surface of PDMS using two loading methods . . . . .	91
4.4	Measurement of the surface topology of the oxidized PDMS subjected to tensile load using replica mold . . . . .	92

4.5	Wrinkles produced by a 10 % tensile strain applied after a 40-minute oxidation. The left-hand image is a 2-D presentation of the data shown in the right. Both images are inverted from the raw data obtained from the AFM from the replica, so the cracks appear as cracks not hillocks. . . . .	93
4.6	Wavelengths of wrinkles produced by tensile loading ( $\square$ ). Wavelengths produced by compressive loading ( $\triangle$ ) are added for comparison . . . . .	93
4.7	Layered structure subjected to a lateral load. The $f$ and $s$ in superscripts and subscripts mean film and substrate, respectively. $H_f$ and $H_s$ are thickness of the film layer and substrate, respectively. . . . .	95
4.8	The ratios of critical strains and wavelengths with respect to Poisson's ratios; ( $\square$ ) $\nu_f = 0.0$ , ( $\circ$ ) $\nu_f = 0.3$ . $\nu_s = 0.49$ is used in the numerical calculations. $H_s/H_f = 100.0$ . . . . .	99
4.9	Schematic for crack opening and assumption of vertical planes . . . . .	100
4.10	Possible types of stress relaxation between cracks . . . . .	101
4.11	Geometry to calculate the decay length . . . . .	102
4.12	Graphic model of the decay length ( $d$ ). It is defined by a length that the magnitude of stress in the film layer becomes half of the input value. . . . .	102
4.13	Comparison between nondimensional decay lengths and crack spacings at different oxidation time. (a) 4, (b) 20, (c) 40, (d) 60 minutes. ( $\circ$ ) nondimensional decay lengths calculated by FE simulations, ( $\square, \triangle, \times$ ) nondimensional crack spacings estimated from the experiment results. Critical strains ( $x$ -axis) are assumed to estimate the ratio of the crack spacing to the film thickness. . . . .	104
4.14	AFM image of 60-minute oxidized PDMS (left) and contour map of the amplitude between selected cracks (right). Horizontal line in left image is same with the $x$ -axis in right image. White parts of the left image are the top of the wrinkles and dark parts are the bottoms. . . . .	105
4.15	Modeling the stress relaxation in the film layer by crack opening. The minus and plus sign in superscripts are used to denote the states before and after crack opening, respectively. . . . .	106

4.16	Effect of crack opening on the ratios of critical strains and wavelengths; $\nu_f = 0.3, \nu_s = 0.49, H_s/H_f = 100.0$ . $E_f$ and $E_s$ are the modulus of the surface-modified layer and substrate, respectively. . . . .	109
4.17	Effect of graded modulus on the ratios of critical strains and wavelengths. $\nu = 0.49$ for entire system. $E_0$ is the modulus at the surface of a modified layer. $E_s$ is the modulus of substrate. . . . .	110
A.1	Elastic structures involving singular points. . . . .	116
A.2	Asymptotic problem corresponding to the point $A$ in Figure 1.1(c). . . . .	120
A.3	Flow chart for the automated eigenvalue solver. . . . .	124
A.4	Geometry of the asymptotic problem of Figure A.2. . . . .	125
A.5	Input window for the first wedge. . . . .	126
A.6	Geometry of the problem with boundaries and interfaces identified. . . . .	127
A.7	Data input window for Boundary 1 from Figure A.6. . . . .	128
A.8	The visual root finder. . . . .	129
A.9	Contour plot of eigenvalues for the problem of Figure A.2. . . . .	130

## LIST OF TABLES

### Table

3.1	Power-law relationships of the FE simulation . . . . .	60
3.2	The surface modulus and length scale estimated by the iterative FE simulation . . . . .	83
3.3	Homogeneous layer approximation of the results of the iterative FE simulations . . . . .	83
3.4	Crack spaces and widths obtained by a nanoindentation experiment. The question marks mean no data has been obtained. . . . .	84
4.1	Average crack spacings used in the comparison . . . . .	103

## ABSTRACT

### CHARACTERIZATION OF A THIN HARD LAYER ON A SOFT SUBSTRATE – THEORY AND ITS APPLICATION ON A SURFACE-MODIFIED PDMS

by  
Dong Hee Lee

Co-Chairs: James R. Barber and Michael D. Thouless

This dissertation presents theoretical investigations to estimate the graded properties of a hard thin layer on a soft substrate. For this purpose, theoretical approaches have been made to explain experimental phenomena that can be observed in the surface-modified layer of PDMS.

A general strategy is presented, which can be used to determine the critical strain and the corresponding wave number for the wrinkling instability of a half space or thick layer loaded in compression, when the elastic properties vary with depth. Results exhibit dependence on modulus ratios similar to those observed when a homogeneous stiff surface layer is bonded to a more flexible substrate (*i.e.* where the elastic properties are piecewise constant).

Indentation theories are explored to explain the linear force-indentation depth relationships obtained from nanoindentation experiments. The plate theory and bi-layer system are considered as a theoretical model for the indentation problem at first. After examining

the theory using the finite-element simulation, we conclude that the theory may not be an adequate model for the indentation by a rigid indenter. A theoretical model is suggested, which considers the indentation into a half space with graded modulus by a rigid indenter. The force-indentation depth relationships very close to linear is obtained when the error function is used as a modulus function. Based on these results, we suggested an iterative method to determine the modulus of a surface-modified PDMS. The effect of residual strains is considered in the iterative method. With the residual strain, the method gives reasonable order of the modulus values.

We did two types of experiments to produce wrinkling in a modified-surface of PDMS. In each experiment, a discrepancy in the wavelengths is observed between the loading methods. To reveal this discrepancy, analytical models to describe the stress field in the system is suggested. The effect of Poisson's ratio mismatch, crack opening, and graded modulus is considered. While qualitative estimations for the discrepancy can be obtained with the effect of crack opening and graded modulus, quantitative estimations are not made in this research.

# CHAPTER I

## INTRODUCTION

### 1.1 Motivation

Poly(dimethylsiloxane) (PDMS) is a clear, elastomeric polymer and has been a valuable material for producing commercial goods, and in many research areas since it was first introduced in the 1960s. For example, PDMS is an important component in making most sealant products, adhesives, silicon caulks. Silicon grease, silicon-based lubricants, cosmetics, and hair conditioner are other forms of its applications. It is also used as an important experimental platform for cutting-edge research in areas such as biomedical engineering (Zhu *et al.*, 2005), electronics and semiconductors (Loo *et al.*, 2002), and microfluidics (Anderson *et al.*, 2000; Fujii, 2002). It has many interesting characteristics, among which, the ease of manufacturability and chemical inertness may be the major attractions to researchers and engineers. PDMS is produced from the base monomer and catalytic agent in liquid state. The production process can be done by pouring the monomer-agent mixture into a mold, and then curing the mixture by heating. Small scale structures can be produced from the PDMS using the same process. Thus, conventional machining processes do not need to be included to the production process. The absence of the machining process is helpful for producing micro-/nano-scale structures. Due to their very small scale, the machining process is naturally not applicable in the production of micro-/nano-

scale structures. Figure 1.1 shows an example of a typical process to fabricate a PDMS microchip (Fujii, 2002).

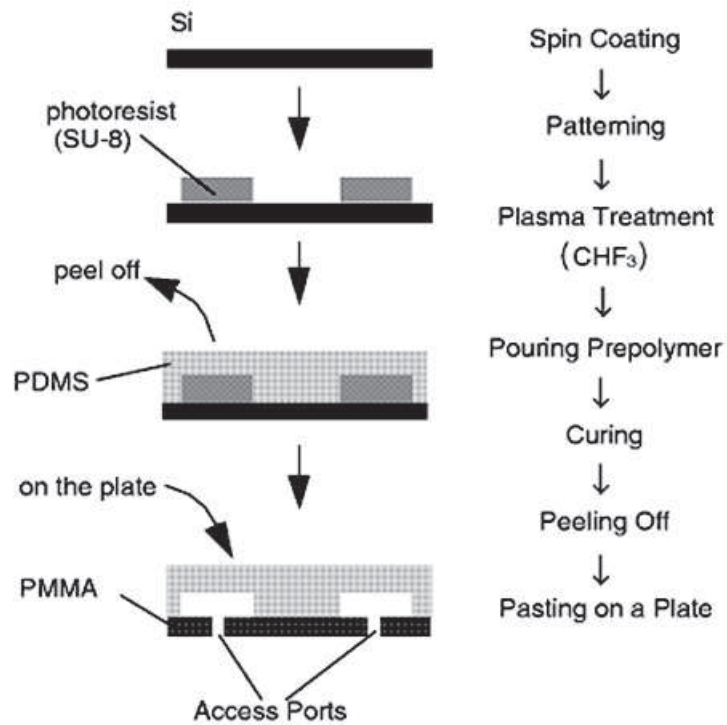


Figure 1.1: Typical fabrication process of PDMS microchip (Fujii, 2002)

After polymerization and cross-linking (*i.e.* the mixing and heating process to produce solid PDMS), a hydrophobic surface is formed on the solid PDMS. The hydrophobic surface maintains good chemical resistance against solvents that could infiltrate and make the material swell. This chemical inertness of PDMS has allowed it to be used as indoor/outdoor electric insulators. With the ease of manufacturability, the hydrophobicity is also an important property in cutting-edge technologies such as biomedical applications or biochemistry dealing with toxic liquids and gases in small scale channels. However, the hydrophobicity becomes an obstacle in some areas such as micro-fluidics and soft lithography, which require great wettability. The hydrophobicity can be diminished temporarily

when PDMS is exposed to severe weather conditions, electrical discharge or contamination. More methods have been found for developing a hydrophilic surface on PDMS. Typical examples of the methods are oxygen plasma, corona discharges, or UV/UVO treatment. After the surface of the PDMS is exposed to these treatments, the hydrophobic surface becomes hydrophilic, and a thin, hard layer is formed as a by-product. While many surface treatment techniques have been introduced and employed to develop the hydrophilic surface on bulk PDMS, the modified layers characteristics, such as chemical structure, thickness, elastic modulus, are unidentified.

Many studies using techniques of chemical analysis have revealed the decrease of the carbon content and increase in the oxygen content in a modified layer. This change of chemical structure caused a thin and brittle layer. Chemical techniques have been used to measure the thickness of the modified layer. Though experimental studies report that the thickness of the layer reaches up to hundreds of nanometers, the reports are suspect due to the uncertainties included in the treatment techniques. The treatment techniques include a diffusion process of ions (oxygen or ozone ions). Because precise control of the diffusion process is hard, the thickness has to be measured under specific treatment conditions. So in that vein, the qualitative analysis, which indicates the thickness is very thin, is generally accepted.

Mechanical techniques have been utilized to measure these properties directly using indentation as well as indirectly using a measurable property such as wavelength of the surface wrinkling, which is produced by external perturbation. Though indentation has been used as a standard method to measure mechanical properties of a material, it is still in the realm of ongoing research due to the very thin layer. Some researchers have used the wrinkling phenomenon to build the relation among the wave length and amplitude of wrinkles, the layer thickness and the elastic modulus. To account for the relation, they as-

sumed a discrete bi-layer system that consists of two layers with uniform thicknesses and uniform material properties in each layer. However, due to the uncertainty of the diffusion process, there is no evidence that the properties are uniform. Therefore, to understand and utilize the modified layer properly, a new method or theory should be developed for the characterization of a layer with graded properties.

## **1.2 Characterization of a modified layer on a substrate**

After observing natural modifications of the surface of a silicon rubber, researchers have tried to develop techniques to re-create the phenomenon in laboratory: Corona discharge, UV/UVO treatment and oxidation by oxygen plasma are well known methods for the surface treatment.

### **1.2.1 Characterization of the modified layer by chemical methods**

The effect of plasma oxidation has been explored by Hansen *et al.* (1965). Through a series of experiments, they generated highly oxidized layers on the surface of polyethylene and polypropylene. They, however, didn't give further details about the oxidized layer, but shown that these oxidized surface layers had remarkably low contact angles with water. This change of surface property was examined by chemical characterization methods (Hollahan and Carlson, 1970). They found  $\text{CH}_2\text{OH}$  groups in the modified-surface of PDMS that was treated by oxygen plasma and corona discharge using Fourier Transform Infrared Spectroscopy (FTIR) characterization. The effectiveness of the modified surface of PDMS was demonstrated by Bodö and Sundgren (1986). They tested the effect of pre-treatments— $\text{Ar}^+$  bombardment and oxygen plasma treatment—to the enhancement of adhesion of titanium film on a PDMS surface. Using scanning electron microscopy

(SEM) and X-ray photoelectron spectroscopy (XPS), they revealed that the pre-treatment resulted in cross-linking on the surface of PDMS and an increased strength of the substrate surface.

These chemical methods also have been used to reveal the mechanism of hydrophobic recovery. Morra *et al.* (1990) performed aging experiment of oxygen plasma-treated PDMS in air and water. Using several surface-sensitive measurements—XPS, static secondary ion mass spectroscopy, and contact angle measurements—they suggested that the mechanism of hydrophobic recovery is a combination of diffusion of polar groups and consequent crosslinking on the contact angle-probed layer. Hillborg and Gedde (1998) explored the hydrophobicity recovery of a high-temperature vulcanized silicone elastomer exposed to corona discharges. They showed that the thickness of the modified surface produced by corona discharge is at least 10 ~ 12 nm using XPS. They found that a small mechanical deformation (< 1% strain) after corona exposure exhibited a faster hydrophobic recovery. They further suggested that it was a mechanical stress that caused a cracking of the brittle silica-like layer, which facilitated the transport of low molar mass PDMS to the surface. Previous studies, which mentioned the mechanism of hydrophobic recovery under different types of surface treatment, were reviewed by Hillborg and Gedde (1999). According to them, most results reported that the migration of the low molar mass species is the major cause of the hydrophobic recovery. Bowden *et al.* (1999) measured the thickness of the plasma-oxidized layer using scanning electron microscope (SEM). They reported that the thickness reached up to 0.5  $\mu\text{m}$  with 15-minute oxidation, and estimated the modulus of the modified surface to be  $E_s \sim 720$  MPa. Ouyang *et al.* (2000) performed experiments to transform cross-linked polysiloxanes to siliconoxide ( $\text{SiO}_x$ ) through the application of a room-temperature UV/ozone conversion process. They reported that a hard film is formed on PDMS substrates, which is limited to a thickness on the order of 20 ~ 30

nm. Hillborg *et al.* (2000) measured the thickness of the oxidized surface using neutron reflectometry and XPS. They reported that the oxygen plasma led to a smooth ( $< 10$  nm) oxidized surface layer with a thickness of  $130 \sim 160$  nm, and the cause of hydrophobic recovery was migration of low molar mass PDMS species to the surface. Efimenko *et al.* (2002) studied the effect of UV and UVO treatments on the modification of a PDMS network. They reported that the material density within the first  $\sim 5$  nm of Sylgard-184 reached about 50% of that of silica. This means that the presence of the silica fillers does not alter the surface properties of the UVO- and UV -modified Sylgard-184 specimens. Feinberg and Brennan (2003) reported an increase in the modulus from  $1.5 \pm 0.8$  MPa to  $3.0 \pm 0.9$  MPa when exposing a cross-linked PDMS to an argon-plasma.

### **1.2.2 Characterization of the modified layer using AFM**

Atomic force microscopy (AFM) is a well known surface characterization method, which contains two operation modes; tapping mode and contact mode. In tapping mode, a small cantilever is oscillated at near its resonant frequency. Images of extremely small surface structures can be obtained using the interaction between the tip and a layer formed on a surface. In contact mode, the tip of the cantilever is brought towards the surface and the static deflection of the cantilever is monitored as a function of scanner displacement. The contact mode is often used as a means of nanoindentation.

The surface morphology is the primary output which can be obtained from tapping mode AFM (TMAFM). TMAFM gives additional output known as phase imaging. Some researchers show that the phase image can be interpreted as the difference of material properties. Magonov *et al.* (1997) showed that the phase image from AFM can be used to distinguish different surface features of both multi component materials and one-component

systems with different density distribution. From this result, Bar *et al.* (2001) used tapping mode AFM to monitor the change of the stiffness in plasma-treated PDMS surface. By performing distance-sweep (Z-sweep) TMAFM and numerical simulation, they argued that a longer oxidation time leads to a greater positive phase shift, which means that the modulus of the oxidized PDMS surface increases with increasing oxidation time. Mills *et al.* (2007) used the phase imaging technique on the 4-minute plasma oxidized PDMS. To estimate the thickness, they bonded two surface-modified PDMS slabs, which were oxidized for different times—1 minute and 4 minutes—than broke the bonded structure. Using tapping mode AFM, they were able to gauge the phase angle of the modified and unmodified section of each PDMS slab. The analysis of the phase image allowed them to report that the thickness of the modified layer is as high as 200 nm.

### **1.3 Characterization of a thin layer by Indentation**

Since it was introduced in the early 1900s, indentation tests have been a standard method to characterize a material. Well-known types of the tests and the tip shape of each test are as follow;

- Brinell hardness test: Sphere
- Berkovich: Pyramid of triangular base
- Rockwell scale: Conical shape
- Knoop hardness test : Pyramid of rhomboid base
- Vickers hardness test: Pyramid of square base

Among these tests, Vickers hardness test is popular one due to its ease and speed with which it can be carried out. Because hardness, defined as the average pressure on the punch (*i.e.* force per projected contact area), is the basic property that can be obtained from the test, the indentation is often called an indentation hardness test. The indentation hardness test is performed by pressing a hard indenter into the bulk material to be examined. By measuring the impression marked by the indenter, hardness can be calculated. However, this technique is limited due to large and varied tip shapes, with indenter rigs that do not have very good spatial resolution (*i.e.* the location of the area to be indented is very hard to specify accurately).

### **1.3.1 Estimation of the local material properties by nanoindentation**

Rapid changes in modern technology and the ever-increasing importance of thin coatings demand more sophisticated indentation methods to characterize new materials — especially in thin layers such as wear resistance coatings—and small-scale structures, smaller than a micron scale. In that sense, we can say the development of nano-indenter (Pethica *et al.*, 1983), which can record both the load and the depth of indenter penetration continuously during the test, opened a new era for the characterization of thin film and small scale structures. Doerner and Nix (1986) suggested a method to interpret data from depth-sensing indentation instruments. They suggested a method to determine elastic properties such as Young's modulus as well as hardness. By assuming linear unloading, they calculated plastic depth, which affects the size of projected area. Oliver and Pharr (1992) suggested a new method to determine hardness and elastic modulus from indentation load-displacement data based on their observation that the unloading part of the curve is not linear for some materials. Instead of using the slope of the unloading curve, they es-

estimate the hardness and the elastic modulus using curvature in the unloading data and the contact area from the indenter shape function. Their method has been used as an important reference for the estimation of the mechanical properties using nanoindentation (Brun *et al.*, 2001; Chowdhury and Laugier, 2004; Huang and Pelegri, 2005). Yeo and Polycarpou (2007) discussed a method to retrieve the magnitude of the elastic recovery from low-force load-unload curves. By calibrating the tip shape function, they demonstrated that the indentation experiment on a fused quartz standard sample showed more accurate results than Oliver and Pharr's method at very shallow ( $< 3\text{nm}$ ) indentation.

Many researchers have used AFM as a means of nanoindentation. Contact mode, one of its basic operation mode, can generate force-displacement curves, and force-indentation depth relations can be deduced from these curves. Due to its high resolution that can measure the order of a few pico-Newtons, it is widely used to measure properties of very soft materials with a vertical distance resolution of better than 0.1 nanometer. Xu *et al.* (1998) introduced a method to interpret the force-displacement curves. They expanded Oliver and Pharr's concept to characterize the mechanical properties of thin polymer films using scanning probe microscopy (STM). By probing the deflection of the cantilever, the force between the tip and sample is measured via a laser beam. Then, the force can be calculated as a function of the indentation depth. Similar to the method suggested by Oliver and Pharr, the elastic modulus was calculated from the early stage of the unloading curve of the force-indentation depth data. Chien *et al.* (2000) used AFM to measure the elastic modulus and ion penetration depth caused by the ion bombardment of  $\alpha$ -particles on polymer composites. They reported that the elastic modulus changed from 1.5 to 3.5 MPa. Brun *et al.* (2001) reported exponential decrease of modulus versus penetration depth in a polypropylene modified by  $\text{He}^+$  particle implantation. Hillborg *et al.* (2004) probed the changes in the normalized modulus of UV/Ozone treated PDMS using indentation map-

ping. Instead of direct interpretation of the probe values, they normalized the values with respect to the modulus of the unexposed PDMS. They found that the normalized modulus increase linearly with respect to the oxidation time and also found that a  $< 50$ -nm level is oxidized homogeneously after exposure.

### **1.3.2 Theoretical studies of indentation**

The relationship between indentation force and depth has been studied over centuries theoretically, and contact mechanics forms the basis of the analytical studies. Hertz (1882) suggested a theory about the relation between two spherical surfaces with different radii and elastic properties. Based on his work, numerous studies have been made to find the stress/strain fields, displacement of the surface, and contact area for various indenter shapes. Boussinesq (1885) suggested a method to determine the stress and deformation fields in elastic homogeneous solids subject to rigid, axisymmetric punch based on potential theory. Sneddon (1965) expanded Boussinesq's theory and suggested general relationships among the load, displacement and contact area for any punch that can be described as a solid of revolution of a smooth function. These studies considered indentation into a homogeneous half space by point forces or axisymmetric punches.

Another vein of studies has dealt with the problem of indentation into a system consisting a thin layer and thick substrate with different material properties. A layered system consisting of two or more layers was first mentioned by Burmister (1945a,b,c) in foundation engineering. His research was related to a project for airport design and construction, so he was interested in the stress distribution and settlement in layered soil deposits of the runway. By assuming each layer to be homogeneous, isotropic, elastic material, he solved a boundary value problem, and obtained the stress distribution in each layer and

a relationship between force and displacement at the surface of the upper layer. He assumed that the upper layer is infinite in the horizontal direction with a finite thickness while the lower layer is infinite in both horizontal and vertical directions. Timoshenko and Woinowsky-Krieger (1959) suggested a solution of the indentation problem into a plate on an elastic foundation (*i.e.* half space). Ol'shanskii (1987) suggested a modified solution of Timoshenko and Woinowsky-Kriegers. He suggested the non-dimensional displacement and pressure as the form of series, which originally expressed as integral forms in Timoshenko and Woinowsky-Krieger's solution. Chen and Engel (1972) analyzed the contact problem in a multilayer medium based on classical elasticity theory. King (1987) analyzed indentation problems into a layered isotropic elastic half space by flat-ended cylindrical, quadrilateral and triangular punches using a basis function technique and a singular integral equation. Using numerical technique, he obtained load-deflection relations via a series of values of the ratio of Young's modulus between the layer and substrate.

A special case of layered systems is the case of a medium that has continuously varying material properties along its thickness. Soil is a typical example of this medium, and many researchers in civil engineering have dug into the problem of indentation into a half space with varying material properties. Calladine and Greenwood (1978) analyzed an incompressible material whose modulus increases with increasing distance from the free surface. They found that the solution is similar to that of the Winkler foundation and suggested a simple formula for the Winkler stiffness of the half space. In a series of papers, Giannakopoulos and Suresh (1997a,b) suggested analytical solutions for the effect of graded material properties on the evolution of stress and displacement fields for a semi-infinite elastic solid indented by either a point force or an axisymmetric indenter. Though a general power law was adopted as a modulus distribution, they only considered a modulus increasing with depth.

### 1.3.3 Numerical analyses of the indentation

Though indentation test have been widely used in experiments and many researchers have contributed theoretical analyses, the analysis of indentation by sharp indenters has been considered one of the hardest problem due to its inherent difficulties: the unavoidable 3-dimensional problem, non-linearity, and stress concentration. Thus, numerical techniques such as finite-element methods have been used to analyze the indentation problem with a sharp indenter. Bhattacharya and Nix (1988a,b) demonstrated that the continuum-based finite-element approach can be applied to determine the load-indentation depth relation for different types of materials and thin films on a substrate. They also revealed that the contact area at the unloading process can be assumed to be linear for a bulk material, but the area is not constant for a thin film. Based on their study, Laursen and Simo (1992) explored the mechanics of the microindentation process using the finite-element method. By investigating several characteristics, such as the actual contact area, that are difficult to evaluate experimentally for either bulk materials or thin film systems, they reported that the finite-element method can be an effective tool for the characterization of the indentation process. They also reported that the contact area is not constant during the unloading process for a thin-film/substrate system.

The adoption of numerical techniques raised a hidden problem in indentation tests, the contact area obtained from tests is not exact due to the pile-up or sink-down effects. Chen and Vlassak (2001) investigated the effect of substrate and pile-up on hardness and stiffness measurements for a variety of thin-film systems, as well as bulk materials, using the finite-element method. Important conclusions that they have made are; 1) the pile-up height in a bulk material scales linearly with indentation depth; 2) the influence of the substrate is not appreciable until pile-up height is greater than the half of film thickness for a soft film on a hard substrate, and the yield stress of a film can be measured from the rela-

tion  $H = P/A$ , as long as the indentation depth is less than the half of the film thickness;

3) if the yield strength of the film is higher than that of the substrate, the substrate effect is inevitable even for indentation depths less than 10-20% of the film thickness. Larsson and Peterson (2002) did numerical analyses concerning microindentation for a homogeneous, isotropic, elastic-plastic thin film (or ribbon) that is perfectly clamped on a hard substrate with the assumption of frictionless contact between the indenter and the material using a commercial finite-element code. They found that bulk behavior can be assumed for indentation depths up to 25% of the film thickness despite the known film/substrate effect. However, their investigation is limited to the case of a deforming (soft) film on a hard (nondeforming) substrate. He and Veprek (2003) suggested a new range of indentation to avoid the substrate effect. They suggested 5% instead of the 10% rule-of-thumb for superhard surface coatings (> 40 GPa) on a relatively soft substrate, such as steel. Other studies of the indentation problem using numerical techniques have been reported by many researchers;

- Analyze of Vickers indentation (Giannakopoulos *et al.*, 1994)
- Analysis of Berkovich indentation (Larsson *et al.*, 1996)
- Numerical study for the elastic contact problem of a layered semi infinite solid compressed by a rigid surface (Komvopoulos, 1988)
- Elastic-plastic finite-element analysis for the axisymmetric problem with a harder and stiffer layer (Kral *et al.*, 1995)
- Develop a procedure to estimate the mechanical properties of implanted layers and thin films on dissimilar substrate using commercial finite-element code (Knapp, 1997)

#### 1.3.4 Estimation of the residual stress/strain in thin films by indentation

Most previous research has concentrated on the measurement of static mechanical properties of thin films, but researchers also have considered the measurement of residual stress in a thin film using indentation. Tsui *et al.* (1996) reported a study of the influences of sample stress on nanoindentation hardness measurements using a sharp Berkovich indenter. They reported that the hardness determined by standard nanoindentation techniques is affected by stress, increasing in compression and decreasing in tension. However, subsequent finite-element simulation (Bolshakov *et al.*, 1996) revealed that the changes in hardness are not correct because standard nanoindentation techniques can not measure the contact area directly. And the contact area was changed by variations in the pile-up geometry. Suresh and Giannakopoulos (1998) suggested a theoretical method to estimate surface residual stress and residual plastic strains using sharp indentation. By assuming equibiaxial residual stresses and residual plastic strains, with a uniform distribution over depth, they did theoretical analyses and suggested practical procedures to determine residual stresses or strains at the surface of bulk materials and in thin films and bulk materials with unknown mechanical properties. However, no experimental verification of the method was provided. Based on their method, Swandener *et al.* (2001) introduced an experimental technique that can measure biaxial residual stress using nanoindentation with a spherical indenter.

Knapp *et al.* (1998) suggested a procedure to determine iteratively mechanical properties for thin, hard films and ion-beam-modified layers on soft substrate. By fitting the result of a finite- element simulation to the experimental force at one or more fixed depths, they demonstrated that they could determine the yield stress and Youngs modulus of Ni sample implanted with Ti and C. Though they reported that the method can be applied to a thin hard layer on a soft substrate, the substrates in their examples were still relatively

hard materials such as Ni or Si.

## **1.4 Surface instability–wrinkling**

Wrinkling is a natural phenomenon which can be observed in a wide range of length scales from carbon nano tubes (Lourie *et al.*, 1998) to folds in rocks (Huddleston and Lan, 1993). Human skins, cloths, skin of dried fruit are typical examples of wrinkling in human life. Generally the instabilities such as buckling or wrinkling have been considered as a nuisance to avoid in engineering area. The Euler beam is a very famous example of instability, and railroads are notorious examples of wrinkling caused by the mismatch of thermal expansion between the steel rod and the soil. However, the exploration of wrinkling on soft substrates has been studied considerably in many applications which need to form small, micro or nano, scale structures.

Lithographic patterning is a well known microfabrication technique that has been used to provide structures to materials on a fine scale. Photolithography is a branch of lithographic patterning techniques and is often applied to semiconductor manufacturing of microchip and fabrication of MEMS devices. However, spontaneous patterning techniques, which utilize wrinkling on an elastomeric polymer, have been intensively studied during past years because they are relatively simple and cost-effective comparing to conventional lithography.

### **1.4.1 Experimental techniques to form spontaneous patterns using wrinkles in a thin film**

Bowden *et al.* (1998) introduced an experimental method to produce a complex, ordered structures on an elastomer substrate. They deposited a gold film from the vapor

phase on a thermally expanded PDMS. Subsequent cooling creates compressive stress in the gold film that is relieved by wrinkling with a uniform wavelength of 20 ~ 50 micrometers. To obtain ordered wrinkles, they created bas-relief patterns before heating. However, the result wrinkles were not ordered globally, but locally at regions near the bas-relief. In the successive paper, they demonstrated similar experiments using a surface layer modified with oxygen plasma on PDMS, instead of metal films (Bowden *et al.*, 1999). Through the observation of similar patterns in the oxidized layer, they reported that the simpler oxidation method can be used to produce ordered pattern of wrinkles. Using a simple model, they found that the wavelength of a wrinkle reaches up to 5  $\mu\text{m}$  and is larger near the edge rather than the middle of specimen. Another experiment performed by Chua *et al.* (2000) also showed that an oxidized surface of PDMS can show similar behavior to the result of Bowden and coworker's. They calculated the thickness of the silica-like layer using measured periodicity of the wrinkles; it ranges between 5.68 and 51.65 nm. They reported that the wavelengths would go up with increasing oxidation time and power. Huck *et al.* (2000) demonstrated a new method to form ordered patterns of buckles in a film of gold deposited on the surface of PDMS. To obtain ordered patterns, they used UV irradiation on the surface, which is covered by mask, than the gold film is deposited on both exposed and unexposed areas of the PDMS surface. In subsequent cooling, the difference of stiffness of the PDMS surface caused ordered pattern in UV exposed area. You *et al.* (2002) used mechanical stress to produce ordered wrinkles. By simply placing PDMS mold on the surface of the film and heating the entire structure, they obtained a highly ordered pattern of wrinkles. These techniques to produce wrinkles have been used in various fields;

- Electronics : Electroactive polymer actuators (Watanabe, 2005), Stretchable interconnectors (Lacour *et al.*, 2004)

- Optical device : Diffraction gratings (Harrison *et al.*, 2004)
- Bio-engineering or life science : Microfluidic sieves (Efimenko *et al.*, 2005), Topographic matrices for cell alignment (Teixeira *et al.*, 2003)

#### 1.4.2 Patterning wrinkles by mechanical deformation

It was not easy to obtain highly ordered patterns with the wrinkling method using thermal expansion mismatch. Thus, some researchers reported a method that applied mechanical deformation instead of thermal expansion. Volynskii *et al.* (2000) used a mechanical strain to produce striped wrinkles in deposited gold film on poly(ethylene terephthalate). Before depositing the gold film, they stretched the substrate and then released the film/substrate structure to produce wrinkles. Without any external treatment such as bas-relief, they got ordered stripe pattern in the gold film. Lacour *et al.* (2004) and Watanabe (2005) also used similar technique to produce ordered strip patterns in a thin film. This technique is simple and easy to apply and obtain ordered pattern over a wide area ( $> 2\text{cm}^2$ , Watanabe (2005)). Ohzono and Shimomura (2004) demonstrated a process to generate stripe patterns in a Pt film deposited on a PDMS slab by controlling compressive strain using a small vice under an optical microscope. From observing the compression-relaxation cycles, they concluded that the formation of wrinkles is reproducible. However, the hysteresis between the cycles may hint the existence of plastic deformation at the time of sample preparation.

An important potential of the wrinkling is that it can be used to determine the properties of a thin layer on a substrate. Stafford *et al.* (2004) suggested an experimental metrology for measuring the elastic modulus of polymeric thin films based on the surface buckling. With placing a thin film of a given thickness and unknown modulus on top of an elastomeric

foundation of known modulus and with measuring the wrinkle wavelength upon stretching the bilayer beyond the critical strain, the unknown modulus can be determined using a classic theory of beam on an elastic foundation. However, to determine the elastic modulus of the film, Poisson's ratio and the thickness of the film should be known. In a successive paper, Wilder *et al.* (2006) demonstrated that this method can be used to determine the properties of substrate based on the buckling in the thin hard film with known properties. They also demonstrated that this method can be used to determine the modulus of gradient substrates, which are prepared by casting three different monomer-curing agent ratios of PDMS (*i.e.* three discrete layers of PDMS). They observed different wavelengths in each layer and proposed a possibility that this method can be used to generate a modulus map across the gradient specimen.

### **1.4.3 Theoretical studies of instability–buckling/wrinkling**

Though many researchers reported techniques and the possibility that ordered spontaneous patterns can be obtained by wrinkling, the mechanism of wrinkling is still under investigation. The problem of instability in elastic solids was first mentioned by Koiter (1945). He formulated buckling as a bifurcation problem associated with the principal solution and provided an asymptotic technique to follow the post-bifurcation equilibrium paths. With the development of large strain continuum mechanics in the early 1950s, Koiter's work was subsequently applied to a vast array of structural buckling problems in mechanics. Budiansky (1974) gave the variational formulation for buckling problems in elastic solids that have a potential energy. The connection between the loss of stability of the principal solution at the lowest load bifurcation in elastic systems is also well explained in this article. The most general variational formulation of the buckling and post-buckling

problem of conservative elastic systems can be found in Triantafyllidis and Peek (1992).

For the analysis of wrinkles in a thin film, many researchers have used classical theories about the beam/plate on an elastic foundation that date back to Biot (1937). Among the theories, recent analyses of wrinkling of thin hard layers have been mostly performed based on the linear perturbation analysis which had operated by Allen (1969). He first analyzed sandwich panels consisting soft core material between two hard panels subjected to compressive load and then defined three modes of deformation then he suggested the expression of critical stresses for each deformation mode. He showed the critical membrane force that depends on the modulus of the substrate. Niu and Talreja (1999) reviewed the linear perturbation theory and suggested a unified model for three face wrinkling modes suggested by Allen. They derived a single expression of the buckling stress from long to short wavelengths. Based on the classic plate theory and energy minimization, Groenewold (2001) derived expressions for the wave length and amplitude for both unidirectional and isotropic wrinkling in a hard plate on a soft substrate. Using the model, he analyzed Bowden and coworker's experiments quantitatively. Though the results were well matched with experiments, they used assumed values of modulus and Poisson's ratio for the thin film. Using similar concept with Groenewold (2001), Cerda and Mahadevan (2003) suggested simple scaling laws for the wave length ( $\lambda$ ) and amplitude ( $A$ ) of wrinkles.

$$\lambda \sim \left(\frac{B}{K}\right)^{-1/4}, \quad A \sim \lambda \left(\frac{\Delta}{w}\right)^{1/2}$$

where  $B$  is the bending stiffness of the plate,  $K$  is the stiffness of the effective elastic foundation, and  $(\Delta/w)$  is an imposed compressive strain. By taking several examples, they implied that the wavelength measurements could be a sensitive technique for the characterization of thin solid films. Chen and Hutchinson (2004) provided analysis re-

sults for the uni-directional compression and buckling patterns in a thin gold film on a PDMS substrate. Among the patterns considered, they reported that the herringbone mode is associated with the lowest average elastic energy of the film/substrate system for films stressed well above critical stress. Huang *et al.* (2004) studied the evolution of wrinkle patterns on a substrate by modeling the film as an elastic nonlinear plate and the substrate as a viscoelastic foundation. Using spectral method and finite element simulation, they found that labyrinth patterns are formed when the initial membrane strains are isotropic, and aligned herringbone or stripe pattern are formed when the initial membrane strains are anisotropic. Huang *et al.* (2005) expanded Chen and Hutchinson's analysis for a structure consisting of a thin layer and a soft substrate with finite thickness. They declared a relation between the amplitude and wavelength of the sinusoidal wrinkles as a function of the modulus and thickness of the substrate that, similar to Chen and Hutchinsons analysis, assumed an infinite elastic substrate. Theories and applications of wrinkling were well reviewed by Genzer and Groenewold (2006). Starting from the human skin, they introduced the history of wrinkling/buckling, theories and applications in various areas and length scales.

All analyses discussed thus far were based on classic plate theory and energy minimization. Thus, the film, or modified layer, was assumed as a homogeneous layer with uniform material properties on an infinite homogeneous elastic foundation. However, there is not known evidence that the properties of a modified layer should be uniform. Moreover, there is no known method to measure the thickness of the modified layer, and the analyses using classic plate theory may be simplified, thus, the estimated wavelengths were not matched with the measured wavelengths (Chen and Hutchinson, 2004). Therefore, there is still a challenge to explore the wrinkling mechanism of a hard layer which has graded material properties on a soft substrate.

## 1.5 Organization of the dissertation

The oxidized PDMS has many advantages for various applications and research areas especially areas that need to deal with very small scale structures. Though many studies have been done to understand and utilize the characteristics of the modified surface, a general method or procedure to determine the graded characteristic of the modified layer is not known. Therefore, to understand and utilize the modified layer more effectively, a method or procedure to characterize the modified surface should be implemented. This is the basic objective of this research. However, a general approach will be considered, instead of a specific study only for the analysis of the modified PDMS. In each chapter, general theories will be introduced first and specific examples will be presented using the oxidized PDMS as an example.

### Chapter 2:

For the objective, a theoretical model was developed, which can analyze the surface instability of an elastic half space that has varying material properties with depth, as well as a layered system with uniform material properties. Using this model, critical conditions (critical strain and wavelength) that generate the surface instability will be discussed for an elastic half space with two grading functions. Critical conditions, which are produced by non-mechanical perturbation, also will be discussed. The proposed model will be verified by comparing with the results of a previous study.

### Chapter 3:

Indentation will be considered as a means to characterize a hard thin film on a soft substrate. Theories of indentation will be explored, first based on the linear force-indentation depth relationship that resulted from experimental observation done by Mills *et al.* (2007). For a bi-layer system, plate theories will be explored, then, a power law and the error function will be considered to investigate the possibility of graded elastic modulus. Based on these analyses, an iterative procedure will be introduced, which can estimate the thickness of the layer, the modulus at surface and its profile. The procedure combines the indentation theory and the relationship between modulus ratio and wave length that are obtained in Chapter II. The effect of residual strains will be discussed.

### Chapter 4:

An experiment to produce wrinkles in the surface-modified layer of PDMS will be introduced. The response of the oxidized surface will be explored according to the different loading method; tensile and compressive loading. The discrepancy of the wavelengths between the loading methods will be discussed based on the knowledge obtained in previous chapters.

### Chapter 5:

Based on the results from previous chapters, conclusions and an outline of the future work will be presented.

### Appendix:

A paper is added in the appendix, which introduces an engineering analysis program. The program is a tool that helps to find the stress and displacement fields near wedges

and is developed based on Williams asymptotic method. While it is not related to current research directly, it could be used to study the stress fields near the crack tip.

## CHAPTER II

# SURFACE INSTABILITY OF AN ELASTIC HALF SPACE WITH MATERIAL PROPERTIES VARYING WITH DEPTH

### 2.1 Introduction

If a structure consisting of a thin stiff layer and a more flexible substrate is subjected to a sufficiently large compressive load, a buckling or wrinkling surface instability can occur, as shown in Figure 2.1.

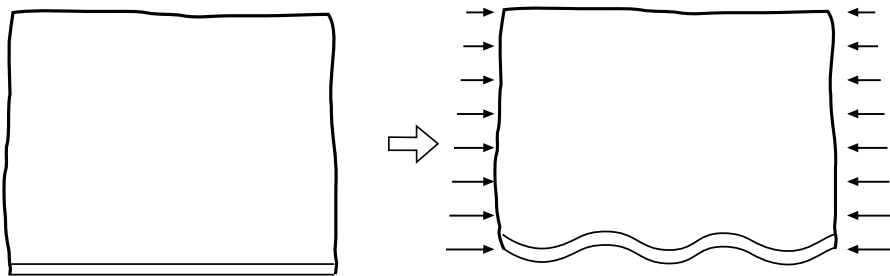


Figure 2.1: Schematic of a half space subjected to a compressive load

Generally, surface wrinkling has been considered as an undesirable phenomenon to be avoided. However, in emerging areas such as micro/nano-fabrication and bio-engineering, wrinkling can be used to produce controlled nano-scale features (Bowden *et al.*, 1999; Moon *et al.*, 2007; Efimenko *et al.*, 2005). It has been proposed that these may be useful for applications such as diffraction gratings, patterned platforms for cell adhesion or

nano-fluidic channels. Surface wrinkling may also provide a way of probing the surface characteristics of the materials Stafford *et al.* (2004).

Chen and Hutchinson (2004) developed a closed-form solution for the wrinkling of a gold layer deposited on an elastomer substrate. They modeled the structure as a plate on a linear elastic foundation with infinite thickness. The same methodology was extended to the case of a thin elastic layer on a substrate of finite thickness by Huang *et al.* (2005). These solutions most naturally relate to the situation in which a thin stiff film is deposited on a more flexible substrate, so that there is a sharp discontinuity in elastic modulus at the interface. However, similar effects should be anticipated in cases where the elastic modulus of the material is graded continuously from the surface to a lower substrate value.

The present work was motivated by observations of micron-scale buckling on oxidized poly(methylsiloxane) (PDMS) in which a stiff surface-modified layer was formed by exposure to an oxygen plasma. The surface layer in this material is formed by a diffusive process, so we anticipate a gradation of mechanical properties from the surface. The absence in the literature of any discussion of surface wrinkling under these conditions prompted the question of how the mechanics of wrinkling might be affected by the graded properties. The intent of this paper is to establish the general mechanics framework for the study of such problems. In particular, we develop a bifurcation method to analyze the onset of surface wrinkling of an elastic layer with elastic properties that are arbitrary functions of depth. The analysis is sufficiently general to allow for an arbitrary distribution of applied compressive strain with depth. In addition to cases of functionally graded elastic modulus, it can therefore be applied to situations where a non-uniform distribution of eigenstrain is generated by thermal expansion or other mechanisms such as a change in lattice parameters due to variable concentration of a diffusive species (Larché and Cahn, 1982). The method is validated by comparison with the results of Huang *et al.* (2005).

It is then used to determine the critical compressive strain at which wrinkling occurs and the associated wavelength for different distributions of elastic moduli. A subsequent paper will examine some specific examples of buckling associated with cracking in oxidized PDMS.

## 2.2 General theory of the instability

The study of buckling (*i.e.* the sudden change of deformation pattern upon increase of the externally applied load) in elastic structures and solids is a classical problem in solid mechanics, dating back two and a half centuries to Euler and his celebrated study of the problem of the elastica. Restricting attention to conservative elastic systems, the key ingredients for the appearance of buckling are the non-linearity of the system's governing equations and the symmetries inherent in its fundamental solution (*i.e.* the solution which exists at small load levels, prior to the appearance of buckling). These features are present in the problem at hand, as will be explained below.

For elastic solids, Koiter (1945) was the first in the mechanics community to formulate buckling as a bifurcation problem associated with the principal solution and provide an asymptotic technique to follow the post-bifurcation equilibrium paths. With the development of large strain continuum mechanics in the early 1950s, Koiter's work was subsequently applied to a vast array of structural buckling problems in mechanics. The interested reader is referred to the eminently readable review article by Budiansky (1974), who gives the variational formulation for buckling problems in elastic solids that have a potential energy. The connection between the loss of stability of the principal solution at the lowest load bifurcation in elastic systems—the reason for associating the onset of a bifurcation buckling with an instability in these applications—is also well explained in

this article. The most general variational formulation of the buckling and post-buckling problem of conservative elastic systems can be found in Triantafyllidis and Peek (1992), whose notation is followed in the present paper.

We consider the orthotropic elastic layer  $0 < x_2 < H_t$  in a state of plane strain and subjected to a compressive load parallel to the  $x_1$ -axis, as shown in Figure 2.2.

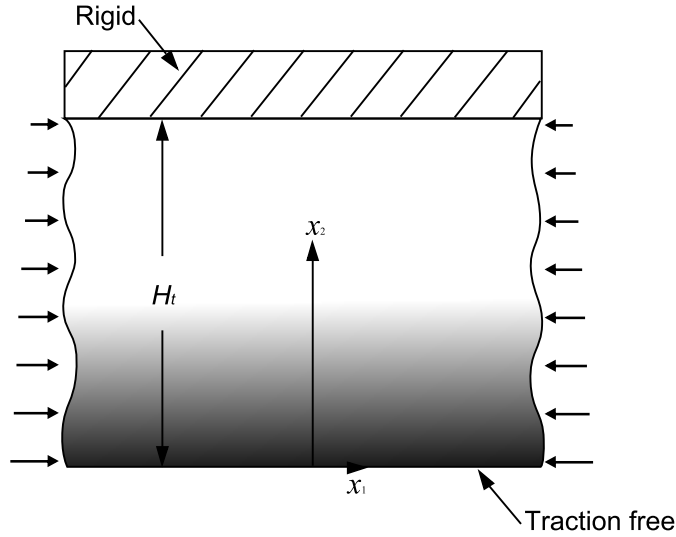


Figure 2.2: The graded layer subjected to a compressive load

The elastic moduli  $L_{ijkl}(x_2)$  are assumed to be arbitrary functions of  $x_2$  only, satisfying the major and minor symmetry conditions

$$L_{ijkl} = L_{klij} = L_{jikl} = L_{ijlk}$$

The boundary  $x_2 = 0$  is assumed traction-free, while  $x_2 = H_t$  is attached to a rigid plane surface. In many cases, the wrinkling field will be localized near the free surface and we can then use the simplifying assumption that the body is a half space ( $H_t \rightarrow \infty$ ) with zero displacement at infinity.

If there is no wrinkling, we expect the stress state to be independent of  $x_1$ . We shall refer to this as the ‘fundamental stress state’ and the corresponding solution of the elasticity

equations as the ‘principal solution’  $\overset{0}{\sigma}$  and it must satisfy both the equilibrium equations

$$\sigma_{ij,j}^0 = 0 \quad i, j = 1, 2$$

and the boundary conditions

$$\overset{0}{\sigma}_{i2} = 0$$

on the free surface  $x_2 = 0$ . Here and subsequently, the notation  $(\cdot)_{,i}$  denotes differentiation with respect to  $x_i$  and the Einstein summation convention is implied over repeated indexes. Since there is no dependence on  $x_1$  (i.e.  $\overset{0}{\sigma}_{,1} = 0$ ), the only possible non-zero stresses are  $\overset{0}{\sigma}_{11}, \overset{0}{\sigma}_{33}$  which can be general functions of  $x_2$ . It is convenient to define a loading parameter  $\Lambda$  such that  $\overset{0}{\sigma}_{ij}(x_2, \Lambda) = 0$  at  $\Lambda = 0$  and increase in  $\Lambda$  describes a set of progressively increased applied loads  $\overset{0}{\sigma}_{ij}(x_2)$ . We then anticipate that above some critical value of  $\Lambda$ , the principal solution will become unstable and wrinkling will occur.

### 2.2.1 Nature of the loading

The loading  $\overset{0}{\sigma}$  may result from a force applied to the extremities of the body, but in this case, compatibility considerations demand that the corresponding strain  $\overset{0}{\varepsilon}_{11} \equiv \varepsilon_0$  be independent of  $x_2$ , giving

$$\overset{0}{\sigma}_{ij} = L_{ij11}(x_2)\varepsilon_0$$

Thus, the fundamental stress state varies with depth in proportion with the elastic modulus. However, more general variations in loading can be generated by other mechanisms. For example, if the temperature  $T(x_2)$  of the body is a function of depth, we will have

$$\overset{0}{\sigma}_{ij} = L_{ijkl}(x_2) \left\{ \overset{0}{\varepsilon}_{kl} - \alpha_{kl} T(x_2) \right\}, \quad (2.1)$$

where  $\alpha_{kl}$  is the tensor of thermal expansion coefficients. This situation may give rise to wrinkling even for a homogeneous half space if the surface is suddenly heated, leading to

high compressive stresses in a thin surface layer. Other physical mechanisms leading to transformation strains could have similar effects.

### 2.2.2 Analysis

Since we assume elastic material response, the problem is conservative and a potential energy functional  $P(u_i)$  exists, defined by

$$P(u_i) = U_{\text{int}} + W_{\text{ext}} \quad (2.2)$$

where  $u_i$  is the displacement field,  $U_{\text{int}}$  is the internal energy and  $W_{\text{ext}}$  is the potential of the external forces. The latter are given by

$$U_{\text{int}} = \int_V W(\varepsilon_{ij})dV \quad \text{and} \quad W_{\text{ext}} = - \int_V \rho b_i u_i dV - \int_{\partial V} t_i u_i d\Gamma \quad (2.3)$$

where  $W(\varepsilon_{ij})$  is the strain energy density in the body  $V$ ,  $b_i$  is the body force and  $t_i$  is the traction on the boundary  $\partial V$ . In the present problem, there is no body force or boundary traction, so only the strain energy term appears in the subsequent analysis. The strain energy density  $W$  is

$$W = \frac{1}{2} L_{ijkl} \varepsilon_{ij} \varepsilon_{kl} , \quad (2.4)$$

where  $\varepsilon_{ij}$  is the strain field. The wrinkling is governed by small strains and moderate rotations, so the strain can be expressed as

$$\varepsilon_{ij} = \frac{1}{2} \left( \frac{\partial u_i}{\partial x_j} + \frac{\partial u_j}{\partial x_i} + \frac{\partial u_k}{\partial x_i} \frac{\partial u_k}{\partial x_j} \right). \quad (2.5)$$

The equilibrium of this system can be examined by taking first derivative of the potential energy,

$$P_{,u} \delta u = 0 \quad (2.6)$$

The equilibrium equation can be expressed in the weak form by substituting Eqs. (2.2)–(2.5) into Eq. (2.6), giving

$$\int_V \sigma_{ij} \delta \varepsilon_{ij} dV = 0 \quad (2.7)$$

The fundamental stress state  $\overset{0}{\sigma}(\Lambda)$  is always a solution of Eq. (2.7). We now consider the stability of the principal solution by taking the derivative of the equilibrium equation. The principal solution is stable in the neighborhood of  $\Lambda = 0$  since it minimizes the total potential energy  $P$  — *i.e.*  $\left[ P_{,uu} \left( \overset{0}{u} \right) \delta u \right] \delta u > 0$ , where  $\overset{0}{u}(\Lambda)$  is the displacement field corresponding to the fundamental stress state  $\overset{0}{\sigma}$  and  $\delta u$  is any kinematically admissible perturbation. As  $\Lambda$  increases, there will be a critical value  $\Lambda^c$  where stability is lost —  $\left[ P_{,uu} \left( \overset{0}{u}(\Lambda^c) \right) \Delta u \right] \delta u = 0$ , where  $\Delta u$  is the eigenmode. By substituting the stress field  $\overset{0}{\sigma}_{ij} = L_{ijkl} \overset{0}{\varepsilon}_{kl}$  in the left-hand side of Eq. (2.7), we can define a stability functional

$$S(\Lambda) \equiv \left[ P_{,uu} \left( \overset{0}{u}(\Lambda) \right) \Delta u \right] \delta u = \int_V \left[ L_{ijkl} \Delta \varepsilon_{kl} \delta \varepsilon_{ij} + \overset{0}{\sigma}_{ij} \Delta \delta \varepsilon_{ij} \right] dV, \quad (2.8)$$

where,

$$\Delta \delta \varepsilon_{ij} = (\Delta u_{k,i} \delta u_{k,j})_s; \quad \delta \varepsilon_{ij} = (\delta u_{i,j} + \overset{0}{u}_{k,i} \delta u_{k,j})_s; \quad \Delta \varepsilon_{ij} = (\Delta u_{i,j} + \overset{0}{u}_{k,i} \Delta u_{r,j})_s.$$

where  $(\cdot)_s$  denotes the symmetric part of the corresponding second-order tensor. Since we assume small strains,  $\left| \overset{0}{u}_{k,i} \right| \ll 1$  and the strain field simplifies to  $\delta \varepsilon_{ij} \simeq (\delta u_{i,j})_s$ ,  $\Delta \varepsilon_{ij} \simeq (\Delta u_{i,j})_s$ . At the onset of wrinkling, we therefore have

$$S(\Lambda^c) = \left[ P_{,uu} \left( \overset{0}{u}(\Lambda^c) \right) \Delta u \right] \delta u = \int_V \left[ L_{ijkl} \Delta u_{k,l} \delta u_{i,j} + \overset{c}{\sigma}_{ij} \Delta u_{k,i} \delta u_{k,j} \right] dV = 0. \quad (2.9)$$

where  $\overset{c}{\sigma} \equiv \overset{0}{\sigma}(\Lambda^c)$ . Integrating Eq.(2.9) by parts and using Gauss' divergence theorem, we obtain

$$\left[ L_{ijkl} \Delta u_{k,l} + \overset{c}{\sigma}_{pj} \Delta u_{i,p} \right]_{,j} = 0 \quad (2.10)$$

with boundary conditions

$$L_{i2kl}\Delta u_{k,l} + \overset{c}{\sigma}_{p2} \Delta u_{i,p} = 0 \quad (2.11)$$

at the free surface  $x_2 = 0$  and

$$\Delta u_i = 0 \quad (2.12)$$

at  $x_2 = H_t$ .

Since the fundamental stress state  $\overset{0}{\sigma}$  and the orthotropic elasticity tensor  $L_{ijkl}$  are independent of  $x_1$ , the equilibrium equation (2.10) and boundary conditions (2.11) simplify to

$$\begin{aligned} &L_{1212}\Delta u_{1,22} + L_{1212,2}\Delta u_{1,2} + \left(L_{1111} + \overset{c}{\sigma}_{11}\right) \Delta u_{1,11} + L_{1122}\Delta u_{2,21} + L_{1221}\Delta u_{2,12} \\ &+ L_{1221,2}\Delta u_{2,1} = 0 \\ &L_{2211}\Delta u_{1,12} + L_{2112}\Delta u_{1,21} + L_{2211,2}\Delta u_{1,1} + L_{2222}\Delta u_{2,22} + L_{2222,2}\Delta u_{2,2} \\ &+ \left(L_{2121} + \overset{c}{\sigma}_{11}\right) \Delta u_{2,11} = 0 \end{aligned} \quad (2.13)$$

$$L_{1212}\Delta u_{1,2} + L_{1221}\Delta u_{2,1} = 0$$

$$L_{2211}\Delta u_{1,1} + L_{2222}\Delta u_{2,2} = 0 \quad (2.14)$$

respectively. Since the material is orthotropic, Eqs. (2.12), (2.13) and (2.14) admit eigenmodes of sinusoidal form

$$\begin{aligned} \Delta u_1 &= U_1(x_2) \sin(\omega x_1) \\ \Delta u_2 &= U_2(x_2) \cos(\omega x_1) . \end{aligned} \quad (2.15)$$

For the problem at hand, the eigenmode decomposition in Eq. (2.15) is complete. Substi-

tuting these expressions into (2.13), we obtain two ordinary differential equations

$$\begin{aligned} L_{1212}U_1'' + L_{1212}'U_1' - \omega^2 \left( L_{1111} + \overset{0}{\sigma}_{11} \right) U_1 + \omega (L_{1122} + L_{1221}) U_2' + \omega L_{1221}' U_2 &= 0 \\ L_{2222}U_2'' + L_{2222}'U_2' - \omega^2 \left( L_{2121} + \overset{0}{\sigma}_{11} \right) U_2 - \omega (L_{2211} + L_{2112}) U_1' - \omega L_{2211}' U_1 &= 0 \end{aligned} \quad (2.16)$$

for the functions  $U_1(x_2), U_2(x_2)$ , where the primes denotes derivatives with respect to  $x_2$ .

The boundary conditions are

$$L_{1212}U_1' - \omega L_{1221}U_2 = 0 ; \quad \omega L_{2211}U_1 - L_{2222}U_2' = 0 \quad (2.17)$$

at  $x_2 = 0$  and

$$U_i = 0 \quad (2.18)$$

at  $x_2 = H_t$ , from Eqs. (2.14), (2.15) and (2.12). In the special case where the material is

isotropic, Eqs. (2.16) and (2.17) reduce to

$$\begin{aligned} \mu U_1'' + \mu' U_1' - \omega^2 \left( \lambda + 2\mu + \overset{c}{\sigma}_{11} \right) U_1 - \omega (\lambda + \mu) U_2' - \omega \mu' U_2 &= 0 \\ \omega (\lambda + \mu) U_1' + \omega \lambda' U_1 + (\lambda + 2\mu) U_2'' + (\lambda' + 2\mu') U_2' - \omega^2 \left( \mu + \overset{c}{\sigma}_{11} \right) U_2 &= 0 \end{aligned} \quad (2.19)$$

with boundary conditions

$$U_1' - \omega U_2 = 0 ; \quad \omega \lambda U_1 - (\lambda + 2\mu) U_2' = 0 , \quad (2.20)$$

at  $x_2 = 0$  and Eq. (2.18) at  $x_2 = H_t$ , where  $\lambda, \mu$  are Lamé 's constants.

Eqs. (2.16), (2.17) and (2.18) or (2.18), (2.19) and (2.20) define an eigenvalue problem for the critical loading parameter  $\Lambda^c$  and the eigenmodes  $U_1(x_2), U_2(x_2)$  for given wavenumber  $\omega$ . If the elastic modulus  $L_{ijkl}$  and the fundamental stress state  $\overset{0}{\sigma}$  are piecewise constant functions of  $x_2$ , the problem can be solved analytically, but the authors were

unable to obtain an analytical solution for the more general case of a functionally graded material. In the next section, we therefore develop a numerical discretization of the problem.

### 2.2.3 Numerical solution

A numerical solution could be obtained by discretizing the differential Eq. (2.16), but it is more convenient to apply the finite element method directly to Eq. (2.8). Using the same eigenmodes as given in Eq. (2.15), the stability functional (2.8) can be written as

$$S(\Lambda, \omega) = \int_{x_1} \int_{x_2} [L_{ijkl} \Delta u_{k,l} \Delta u_{i,j} + \bar{\sigma}_{ij} \Delta u_{k,i} \Delta u_{k,j}] dx_2 dx_1 \quad (2.21)$$

Stability of the structure depends on  $S(\Lambda, \omega)$  being positive definite for all  $\omega \in \mathfrak{R}$ . Since from symmetry  $S$  depends on  $\omega^2$ , only  $\omega > 0$  needs to be checked for  $\Lambda$ .

The  $x_2$  domain is decomposed in a set of 2-node linear interpolation elements, within each of which the unknown displacement  $U_i$  is represented in the form

$$U_i(x_2) = \sum_{I=1}^2 N_I(x_2) u_i^I \quad (2.22)$$

where  $N_I(x_2)$  is shape function and  $u_i^I$  is the local degree of freedom for  $U_i$  at the two terminal nodes ( $I = 1, 2$ ) of the element. For each element there are therefore four degrees of freedom, which we combine into the vector

$$\mathbf{q}_e = \{u_1^1, u_2^1, u_1^2, u_2^2\}^T$$

By substituting Eq. (2.22) to Eq. (2.21) and integrating over the element in question in  $x_2$ -space, we obtain the element stiffness matrix

$$\mathbf{k}_e = \int_e \mathbf{L} dx_2,$$

where

$$\mathbf{L} = \begin{bmatrix} \omega^2 \left( L_{1111} + \overset{0}{\sigma}_{11} \right) & \omega(L_{1122} - L_{1221}) & \omega^2 \left( L_{1111} + \overset{0}{\sigma}_{11} \right) & \omega(L_{1122}N_1N'_2 - L_{1221}N'_1N_2) \\ N_1N_1 + L_{1212}N'_1N'_1 & N_1N'_1 & N_1N_2 + L_{1212}N'_1N'_2 & \\ \\ \omega(L_{2211} - L_{2112}) & \omega^2 \left( L_{2121} + \overset{0}{\sigma}_{11} \right) & \omega(-L_{2112}N_1N'_2 + L_{2211}N'_1N_2) & \omega^2 \left( L_{2121} + \overset{0}{\sigma}_{11} \right) \\ N_1N'_1 & N_1N_1 + L_{2222}N'_1N'_1 & N_1N_2 + L_{2222}N'_1N'_2 & \\ \\ \omega^2 \left( L_{1111} + \overset{0}{\sigma}_{11} \right) & \omega(-L_{1221}N_1N'_2 + L_{1122}N'_1N_2) & \omega^2 \left( L_{1111} + \overset{0}{\sigma}_{11} \right) & \omega(L_{1122} - L_{1221}) \\ N_1N_2 + L_{1212}N'_1N'_2 & N_2N_2 + L_{1212}N'_2N'_2 & N_2N_2 + L_{1212}N'_2N'_2 & N_2N'_2 \\ \\ \omega(L_{2211}N_1N'_2 - L_{2112}N'_1N_2) & \omega^2 \left( L_{2121} + \overset{0}{\sigma}_{11} \right) & \omega(L_{2211} - L_{2112}) & \omega^2 \left( L_{2121} + \overset{0}{\sigma}_{11} \right) \\ -L_{2112}N'_1N_2 & N_1N_2 + L_{2222}N'_1N'_2 & N_2N'_2 & N_2N_2 + L_{2222}N'_2N'_2 \end{bmatrix}$$

The global stiffness matrix  $\mathbf{K}$  can then be constructed by adding the element stiffnesses such that

$$\sum_e \mathbf{q}_e^T \mathbf{k}_e \mathbf{q}_e = \mathbf{Q}^T \mathbf{K} \mathbf{Q}$$

where  $\mathbf{Q}$  is a vector of global degree of freedom. The eigenvalues of the system can be obtained by decomposing the global stiffness matrix  $\mathbf{K}$  using Choleski decomposition, subject to the essential boundary condition  $U_i(H_t) = 0$ . We write

$$\mathbf{K} = \mathbf{L} \mathbf{D} \mathbf{U}$$

where  $\mathbf{L}$  is the lower triangular matrix with unit diagonal terms,  $\mathbf{U} = \mathbf{L}^T$  is the upper diagonal matrix and  $\mathbf{D}$  is diagonal matrix. By tracking the positive definiteness of  $\mathbf{D}$  matrix, the system stability can be evaluated. If the system is stable, the lowest eigen value should be positive. When the load parameter  $\Lambda$  reaches at a critical value  $\Lambda^c$  at which the lowest element of  $\mathbf{D}$  is zero, the system becomes unstable.

## 2.3 Results

### 2.3.1 Convergence and validation

The method developed in the preceding two sections can be used to evaluate the stability of a half space with arbitrarily graded properties and applied loading. However, to validate the method, we first compare its predictions with the results of Huang *et al.* (2005) for an isotropic homogeneous layer of thickness  $H_f$  on a dissimilar substrate of finite thickness  $H_s$  (so in our notation  $H_t = H_f + H_s$ ). Notice that these authors made the simplifying assumption that the shear stress at the film/substrate interface is zero, whereas our analysis is exact within the context of the numerical discretization.

Figure 2.3 shows the critical strain  $\varepsilon_0^c$  and critical dimensionless wavelength  $2\pi/\omega^c H_f$  as a function of the thickness ratio  $H_s/H_f$  for three values of the modulus ratio  $\bar{E}_f/\bar{E}_s$ , where  $\bar{E}$  is the plane strain modulus defined as

$$\bar{E} = \frac{E}{1 - \nu^2}$$

and  $E$  and  $\nu$  are Young's modulus and Poisson's ratio, respectively. Poisson's ratio for both film and substrate was taken as  $\nu = 0.4$ . The solid lines are taken from Huang *et al.* (2005) and reproduce their Fig. 5, while the points were obtained from the present program. The agreement is extremely good in all cases.

Tests were also conducted to determine the number of elements required for the numerical solution to converge. A finer mesh was used in the film and in the upper layers of the substrate since the perturbation is concentrated in this region. Better than 0.1% accuracy was obtained using 100 elements in the film and an equal number in a region of the substrate adjacent to the interface of thickness  $3H_f$ . For the most efficient meshing, the

element gradation should follow the rate of decay of the perturbation, but this depends on the wavelength which is only known *a posteriori*.

It is clear from Figure 2.3 and from heuristic considerations that the thickness of the substrate has little effect on the results if it is large compared with the wavelength of the eigenmode. For the homogeneous layer, we found that the half space results can be recovered from the necessarily finite numerical model provided that the substrate thickness  $H_s$  is greater than about twice the wavelength — *i.e.*  $H_s > 4\pi/\omega^c$ .

### 2.3.2 Graded materials

We next turn our attention to continuously graded materials, for which no previous results are available. We considered two examples: a half space in which the plane strain modulus is graded exponentially from a surface value  $\bar{E}_0$  to a substrate value  $\bar{E}_s$  as  $x_2 \rightarrow \infty$  — *i.e.*

$$\bar{E}(x_2) = \bar{E}_s + (\bar{E}_0 - \bar{E}_s) \exp\left(\frac{-x_2}{H}\right)$$

and one in which the grading follows the complementary error function

$$\bar{E}(x_2) = \bar{E}_s + (\bar{E}_0 - \bar{E}_s) \operatorname{erfc}\left(\frac{x_2}{H}\right). \quad (2.23)$$

In both of these examples, the parameter  $H$  serves as a characteristic length for the decay and can also be used in constructing an expression for the dimensionless wavenumber  $\omega^c H$ . The two expressions are compared in Figure 2.4, which shows that the error function decays to zero more rapidly at large depths.

Figure 2.5 shows the critical strain  $\varepsilon_0^c$  and the dimensionless wavenumber  $\omega^c H$  for the exponentially graded modulus as a function of the modulus ratio  $\bar{E}_0/\bar{E}_s$ . Poisson's ratio was taken as a constant  $\nu = 0.4$  for these calculations. For comparison we also show on these figures the results for a homogeneous layer (solid line). The parameters for this

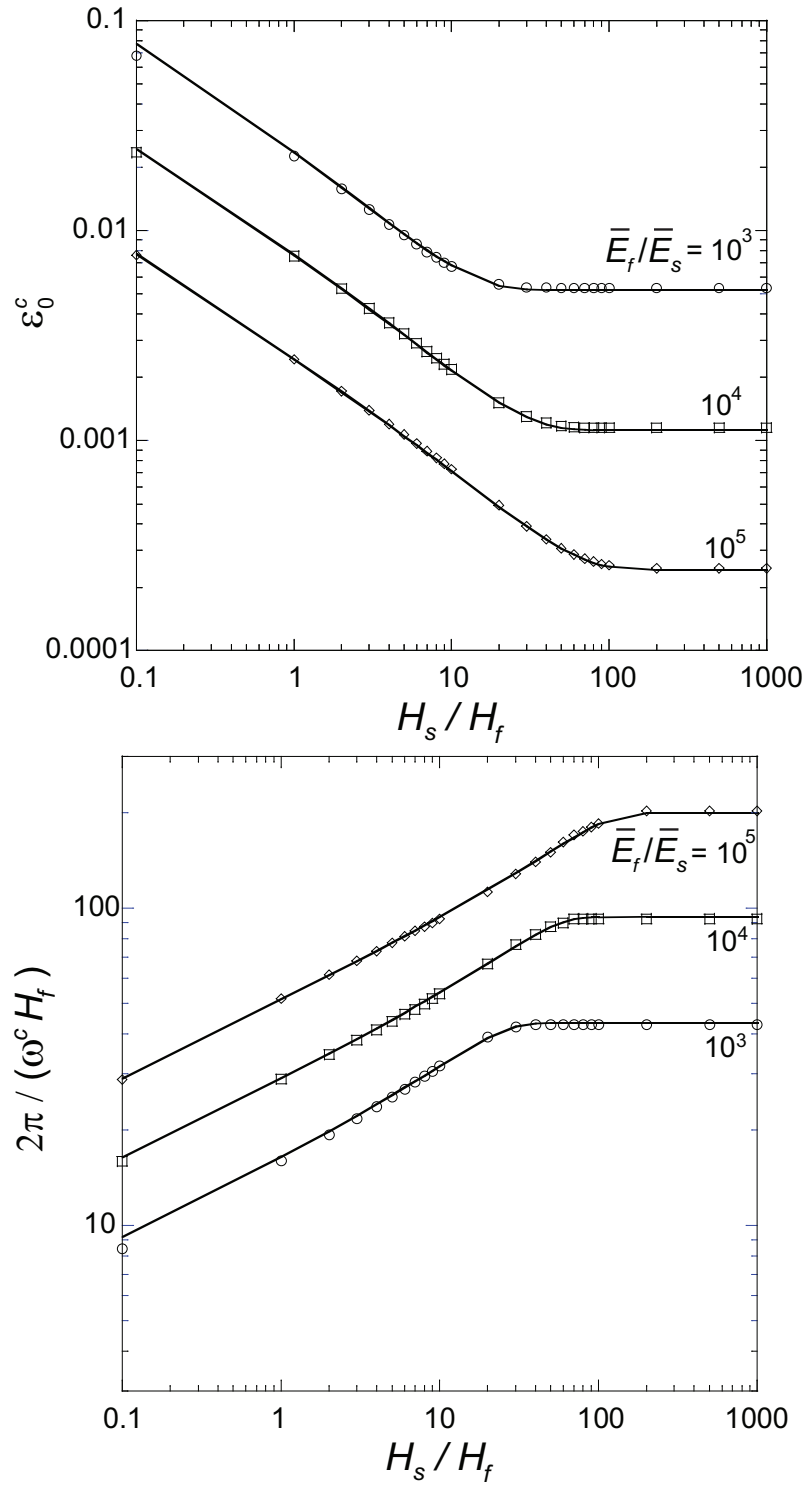


Figure 2.3: Critical strain and wavelength for a homogeneous layer on a dissimilar substrate. The solid lines are taken from Huang *et al.* (2005).

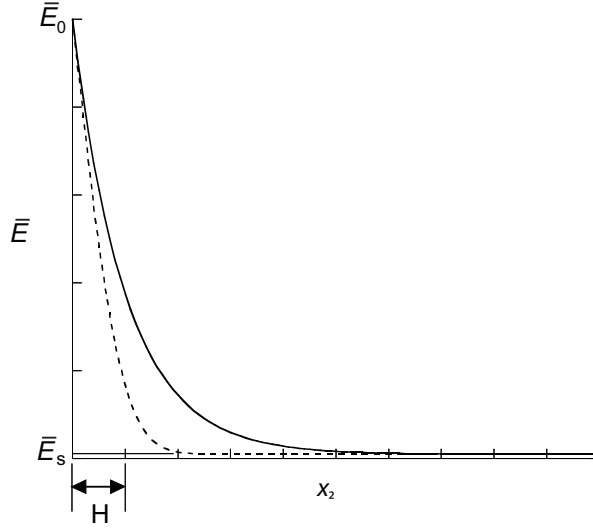


Figure 2.4: Examples of variable modulus: — exponential grading, - - - error function grading

‘equivalent homogeneous layer’ were chosen by matching the area between the modulus curve and the constant substrate level and the first moment of the same area, giving

$$H_f = \frac{2 \int_0^\infty (\bar{E}(x_2) - \bar{E}_s)x_2 dx_2}{\int_0^\infty (\bar{E}(x_2) - \bar{E}_s) dx_2} \quad (2.24)$$

and

$$\bar{E}_f = \frac{1}{H_f} \int_0^\infty (\bar{E}(x_2) - \bar{E}_s) dx_2 . \quad (2.25)$$

The graded results show a trend similar to the homogeneous layer, but the dependence on modulus ratio is not now of power law form and both critical strain and wavenumber become less sensitive to modulus ratio at high ratios. However, the homogeneous approximation (2.24) and (2.25) underestimates the critical strain by up to a factor of two and generally overestimates the corresponding wavenumber.

Corresponding results for error-function gradation are shown in Figure 2.6. The results are qualitatively similar to the exponential case, though the homogeneous approximation to the critical wavenumber is less good.

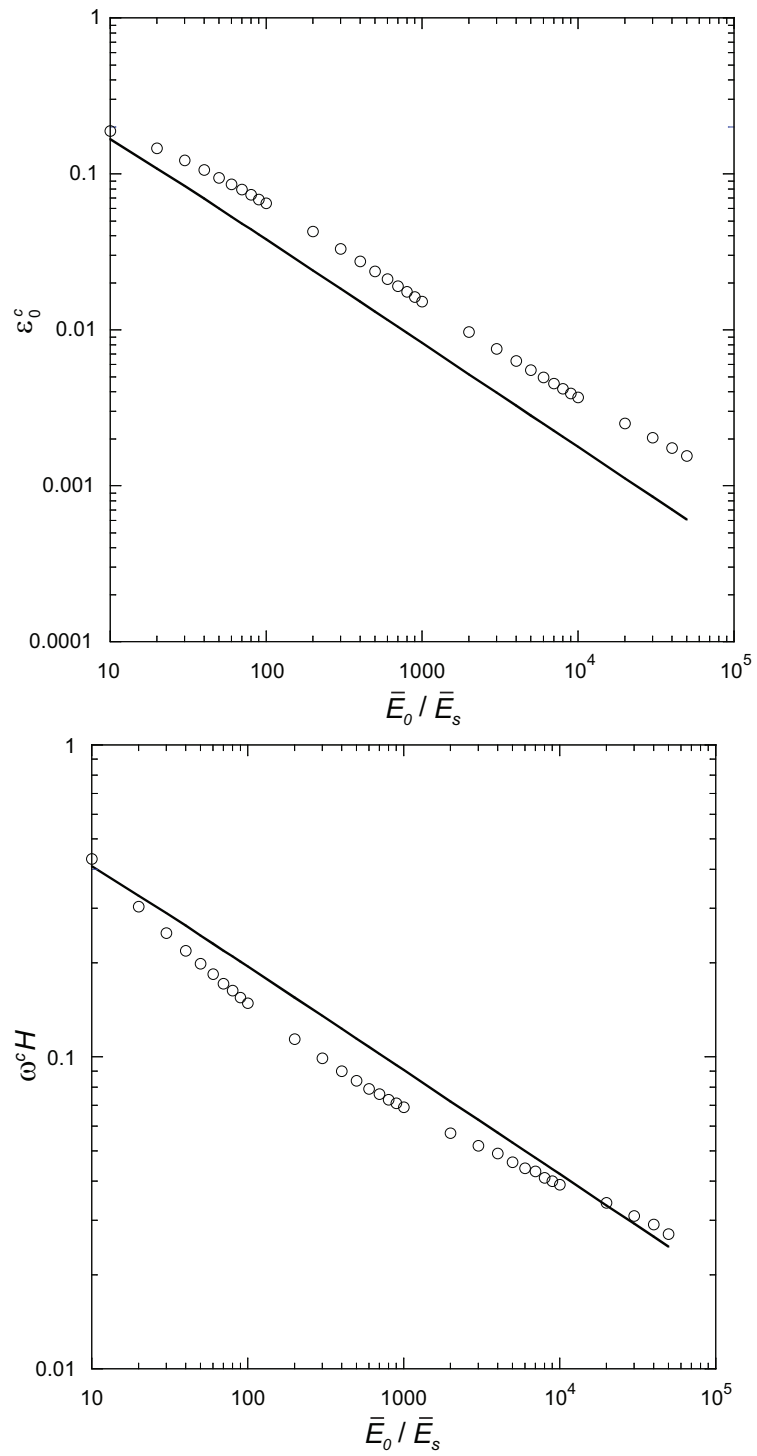


Figure 2.5: Critical strain and dimensionless wavenumber for exponential grading. The solid line represents a homogeneous layer approximation using Eqs. (2.24) and (2.25).

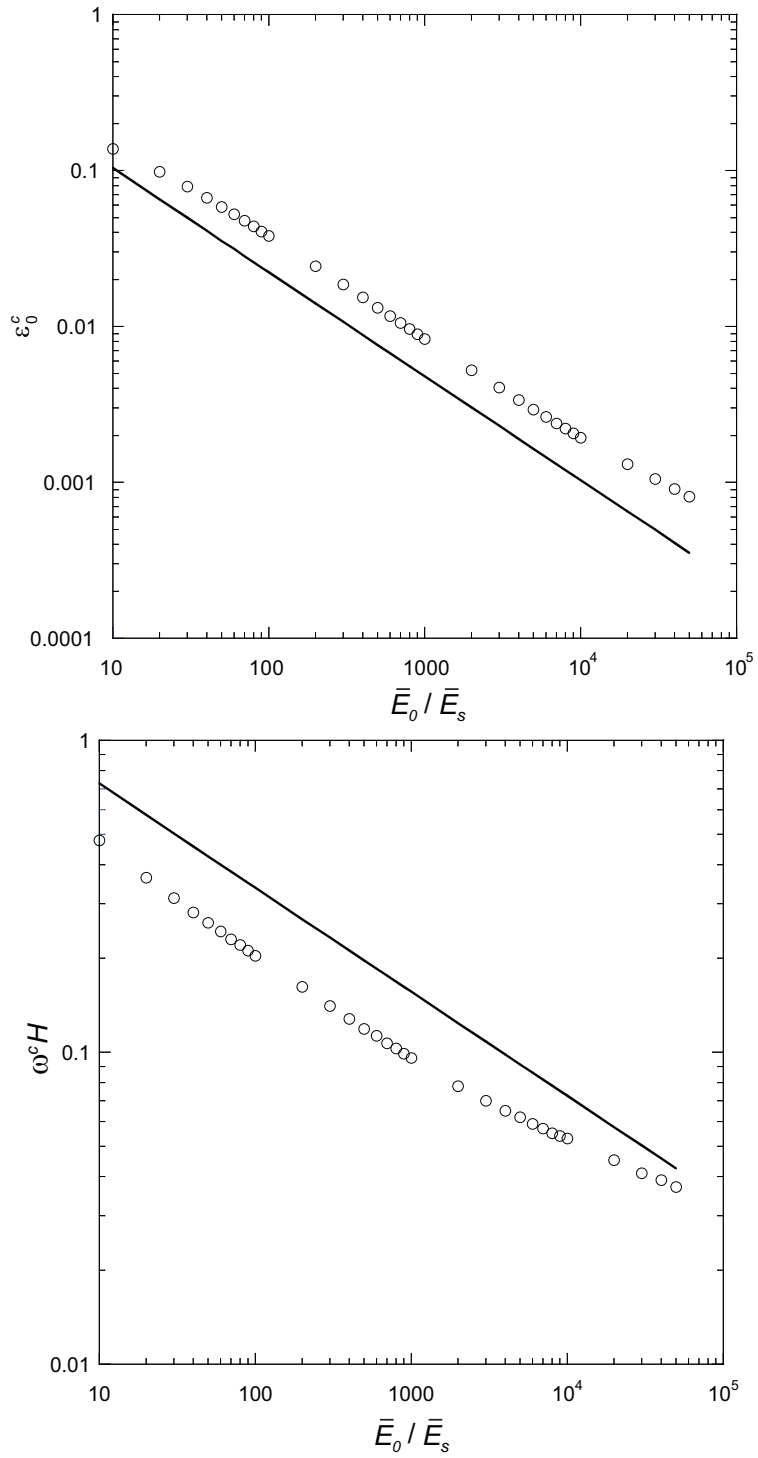


Figure 2.6: Critical strain and dimensionless wavenumber for error function grading. The solid line represents a homogeneous layer approximation using Eqs. (2.24) and (2.25).

### 2.3.3 Effect of Poisson's ratio

In the preceding results, Poisson's ratio was assumed to be independent of depth. To examine the effect of grading in  $\nu$ , we considered the case in which both  $\bar{E}$  and  $\nu$  have error function grading. In other words,  $\bar{E}$  is given by Eq. (2.23) and

$$\nu = \nu_s + (\nu_0 - \nu_s)\operatorname{erfc}\left(\frac{x_2}{H}\right) \quad (2.26)$$

The critical strain and wave number are shown as functions of  $\bar{E}_0/\bar{E}_s$  in Figure 2.7 for the case where  $\nu_0 = 0$  and  $\nu_s = 0.49$ . For comparison, we also show results for the two cases where the modulus has the same grading but Poisson's ratio is uniform and given by the extreme values  $\nu_0 = 0$  and  $0.49$ , respectively. For a homogeneous layer on a homogeneous substrate, the critical strain and wave number depend only on the ratio of the plane strain moduli  $\bar{E}_0/\bar{E}_s$  and are otherwise unaffected by Poisson's ratio (Huang *et al.*, 2005). By contrast, if the modulus is graded, we find a significant effect of  $\nu$  even if it is assumed uniform. These effects are greatest when the modulus ratio is relatively modest. For example, for  $\bar{E}_0/\bar{E}_s=10$ , the critical strain for  $\nu = 0$  exceeds that for  $\nu = 0.49$  by almost 90%. The results for graded Poisson's ratio are very close to those obtained using the uniform value  $0.49$ . In other words, a good approximation is obtained if the substrate value of  $\nu$  is used throughout the body. This conclusion was verified by other numerical experiments.

### 2.3.4 Thermoelastic wrinkling

As a final example, we consider the case where the material is isotropic and homogeneous, but the fundamental stress state  $\sigma^0$  varies with depth because of a non-uniform temperature field due to surface heating, as in Eq. (2.1). If the body is initially at zero temperature and the boundary  $x_2 = 0$  is raised to a constant temperature  $T_0$  for time  $t > 0$ ,

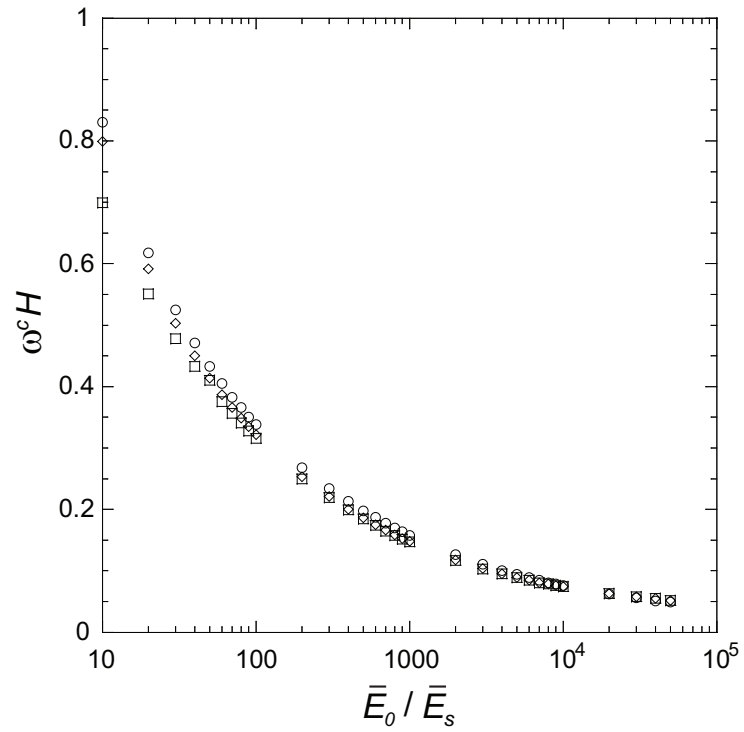
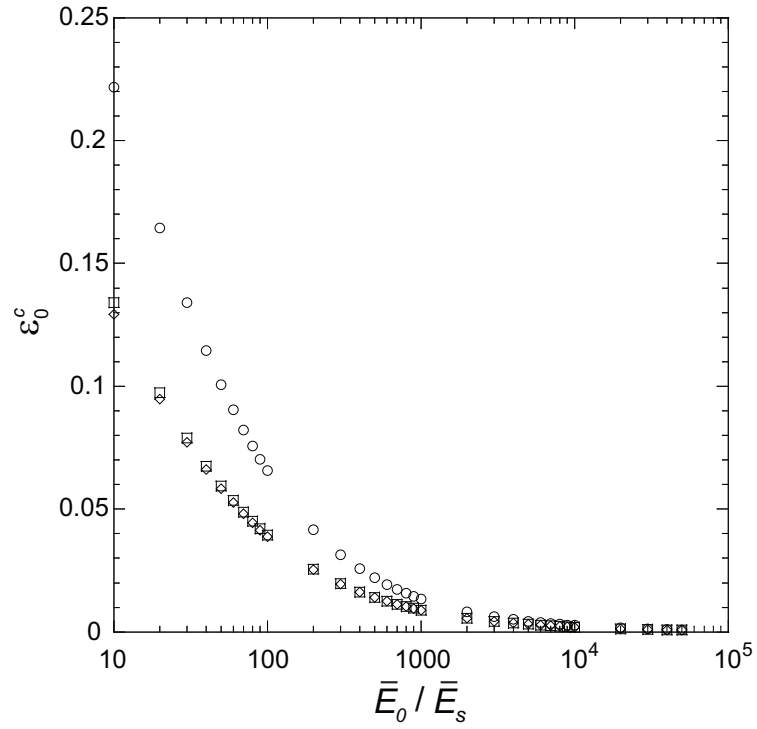


Figure 2.7: Effect of Poisson's ratio; ( $\circ$ )  $\nu = 0$  and uniform, ( $\square$ )  $\nu = 0.49$  and uniform, ( $\diamond$ ) Eq. (2.26) with  $\nu_0 = 0, \nu_s = 0.49$ .

the subsequent temperature profile will be given by

$$T(x_2, t) = T_0 \operatorname{erfc} \left( \frac{x_2}{\sqrt{4\kappa t}} \right), \quad (2.27)$$

where  $\kappa$  is the thermal diffusivity Carslaw and Jaeger (1959, §2.5). The corresponding fundamental stress state is then

$$\sigma_{11}^0 = -\frac{E\alpha T_0}{(1-\nu)} \operatorname{erfc} \left( \frac{x_2}{\sqrt{4\kappa t}} \right), \quad (2.28)$$

from Eq. (2.1), where  $\alpha$  is the coefficient of thermal expansion.

Both expressions have the same functional form at all times, but the characteristic length scale  $\kappa t$  (and hence the wavelength of any wrinkles) increases with time. We can therefore determine a universal dimensionless critical thermal strain  $\alpha(1+\nu)T_0^c$  and critical wavenumber  $\omega^c \sqrt{\kappa t}$  from a single numerical calculation. We find

$$\alpha(1+\nu)T_0^c = 0.287; \quad \omega^c \sqrt{\kappa t} = 75.6. \quad (2.29)$$

A related problem is one in which the thermal-expansion mismatch is uniform and limited to a surface layer of thickness  $H_f$  in a homogeneous material. The critical strain for this problem is given by  $\alpha(1+\nu)T_0^c=0.267$ , and the critical wave number is  $\omega^c H_f = 12.2$ . This thermoelastic problem also provides a model for other phenomena that involve compressive misfit strains within a surface layer; for example, a layer with epitaxial strains, a layer with a volume change due to a phase transition or concentration of a diffusive species (Larché and Cahn, 1982), or a piezo-electric layer. The critical strains due to pure thermoelastic effects are sufficiently large that the surface instabilities may not be of practical significance when there is no modulus mismatch, but in conjunction with a stiff surface layer, phenomena such as thermoelastic wrinkling are likely to occur at practical levels of

strain.

## 2.4 Conclusions

We have presented a general strategy for determining the critical strain and the corresponding wavenumber for the wrinkling instability of a half space or thick layer loaded in compression, when the elastic properties vary with depth. Results exhibit dependence on modulus ratios similar to those observed when a homogeneous stiff surface layer is bonded to a more flexible substrate (*i.e.* where the elastic properties are piecewise constant). We present expressions permitting analytical results for the latter case to be used in an approximate sense. The method can also be applied to thermoelastic loading associated with transient surface heating and we give results for the critical surface temperature at which a homogeneous half space will develop wrinkling.

## CHAPTER III

# ESTIMATION OF THE PROPERTIES OF A THIN HARD LAYER ON A SOFT SUBSTRATE BY INDENTATION

### 3.1 Introduction

Indentation has been used as a standard method to determine mechanical properties such as hardness, stiffness, or modulus (Cousins *et al.*, 1975; Robinson and Truman, 1977). It also has been used to measure the material properties of thin films on a substrate whose thickness reaches up to a few microns (van der Zwaag and Field, 1983; Vinci and Bravman, 1991). Recent technical/engineering development, which is moving toward smaller and smaller scales, requires more sophisticated method to characterize properties of new materials and small structures at sub-micron or nano-scale accuracy. This requirement has led to another technical development that makes nano-indentation possible. Atomic force microscopy (AFM) is a well known implementation of the development. Many researchers have characterized materials and small-scale structures including the oxidized layer of PDMS using AFM as a means of nano-indentation (VanLandingham *et al.*, 1997; Chien *et al.*, 2000).

Recently, Mills *et al.* (2007) reported an interesting observation about indentation experiments in PDMS. They investigated the surface of unoxidized and oxidized PDMS

using AFM with SiNi tip attached to a compliant cantilever ( $k = 0.58 \text{ N/m}$ ). When unoxidized PDMS samples were indented, a non-linear load versus indentation relationship was observed (Figure 3.1a). By contrast, a relationship close to linear was observed from indentation into oxidized PDMS samples (Figure 3.1b). They reported that the relationship between the applied load and indentation depth is in the range of 1.9 to 2.1 N/m in linear scale. If the relationship is converted using a power law ( $P = Cz^m$ ), the exponent ( $m$ ) ranges between 0.98 and 1.01.

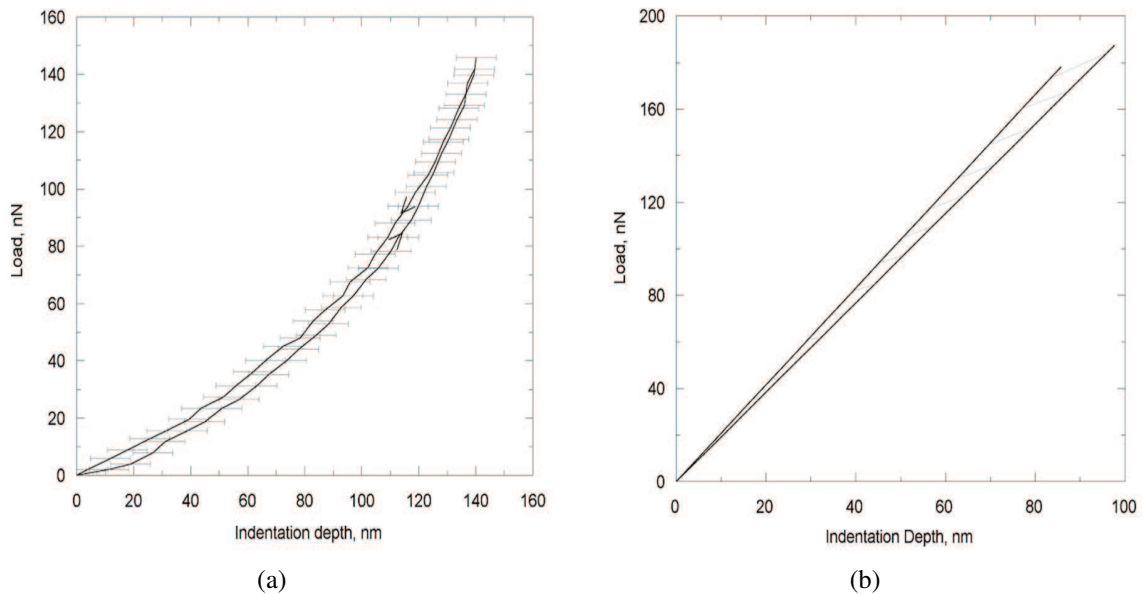


Figure 3.1: Load versus Indentation depth relation for the compliant cantilever ( $k = 0.58 \text{ N/m}$ ) indenting on (a) unoxidized and (b) 4-minute oxidized PDMS (Reproduced from Mills *et al.* (2007))

Typically, non-linear relationships between load and indentation depth have been reported in indentation experiments. Thus, the linear relation could be an interpretation of the modified properties of PDMS. Though many experimental results have reported the possibility of non-uniform properties of the modified layer (Chien *et al.*, 2000; Brun *et al.*, 2001; Efimenko *et al.*, 2002), there are not many theoretical analyses that take the

non-uniform properties into account. These analyses that have considered the graded characteristics have dealt with a modulus that increases with increasing depth (Calladine and Greenwood, 1978; Giannakopoulos and Suresh, 1997a,b).

Therefore, a theoretical method needs to be set up for the estimation of the modified properties of PDMS with the assumption of graded material properties. To build the method, indentation theories will be explored to explain the possible cause of the linear force-indentation depth relationship observed by Mills *et al.* (2007). Then, an iterative procedure to estimate the properties of the modified layer - modulus at the surface and thickness - will be presented based on the suggested theory and the experimental results reported by Mills *et al.* (2007).

### **3.2 Indentation into a homogeneous plate on a half space**

A possible theoretical solution for the linear response in the indentation experiment is a plate on an elastic half space which is indented by a point force. Because the modified layer is generally considered as very thin and harder than the substrate (*i.e.* bulk PDMS), and the AFM tip is much smaller relative to the size of oxidized specimen, the system could be modeled as a plate on an elastic half space.

If the plate theory is an adequate solution to explain the linear force-indentation relationship, the material properties of the modified layer can be determined based on following argument. If a point force acts on the plate, it will deform to a finite radius (Figure 3.2a). If the material properties for the plate and half space are given, the indentation depth is always proportional to the point force. For a rigid indenter, if the radius of a deformed plate is larger than that of the indenter, then the contact load can be considered as a point force and the problem will be linear (Figure 3.2b). Beyond some critical force, the contact

will be become an annular load and the problem will be non-linear (Figure 3.2c). Therefore, if the parameters of the problem are near the plate/foundation (*i.e.* half space) limit, an equivalent stiffness for the plate could possibly be determined. If there is an independent estimate of the film thickness, this would permit an estimate of the modulus of the plate.

A classic indentation theory will be reviewed, which can be a solution for the indentation problem into homogeneous plate resting on elastic half space without friction or adhesion. This theory will be examined for the case of plate bonded to a half space, which models a modified layer on a substrate. The theoretical approaches will be examined using the commercial finite-element code (ABAQUS) by simulating the indentation process.

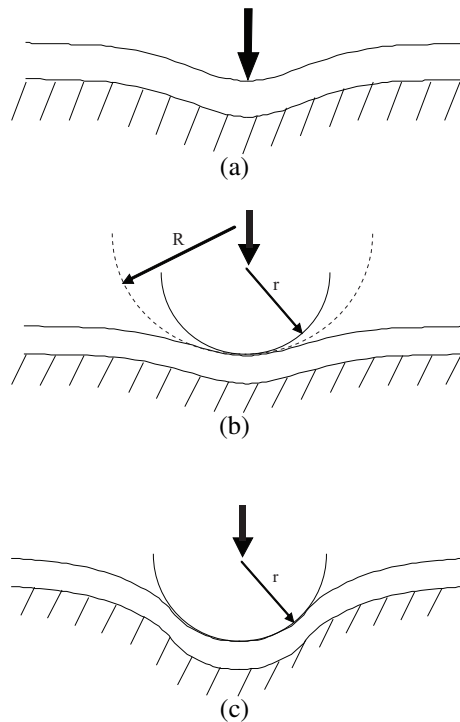


Figure 3.2: Possible deformation of a plate by a point force and a rigid indenter

### 3.2.1 Indentation into a plate on an elastic half space without friction / adhesion

Consider the problem of a thin plate resting on an elastic half space without friction and subjected to a normal compressive force  $P$  (Figure 3.3). The plate consists of thickness  $H_f$  and elastic properties  $E_f$  and  $\nu_f$ , and the elastic half space consist of elastic properties  $E_s$  and  $\nu_s$ .

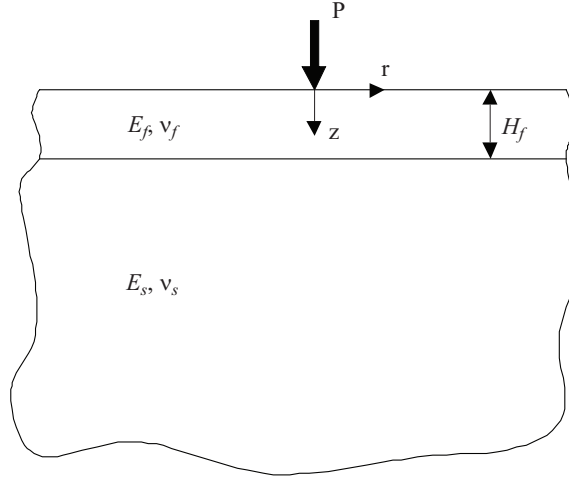


Figure 3.3: Schematic of indentation into a plate on elastic half space.  $E$  is the elastic modulus, and  $\nu$  is Poisson's ratio.  $f$  and  $s$  in the subscripts mean the plate and substrate, respectively.  $H_f$  is the thickness of the plate.

Timoshenko and Woinowsky-Krieger (1959) gave a solution of the problem for a plate resting on a half space without friction. The relationship between force and displacement ( $w$ ) and contact pressure ( $p$ ) were given with the form of Eq. (3.1) at a point on the surface of the plate.

$$w = Pl^2(2D)^{-1}w_0, \quad p = Pl^{-2}p_0 \quad (3.1)$$

where,

$$w_0 = \frac{1}{\pi} \int_0^{\infty} \frac{J_o(\lambda\rho)}{\lambda^3 + 1} d\lambda, \quad p_0 = \frac{1}{2\pi} \int_0^{\infty} \frac{J_o(\lambda\rho) \lambda}{\lambda^3 + 1} d\lambda$$

$$\rho = r/l, \quad D = E_f H_f^3 (12(1 - \nu_f^2))^{-1}, \quad l = (2DE_s^{-1} (1 - \nu_s^2))^{1/3}$$

$E, \nu$  are the elastic modulus and Poisson's ratio of a plate of thickness  $H_f$  while  $E_s, \nu_s$  are the characteristics of the elastic half space, and  $J_0(z)$  is the Bessel function.  $D$  is the flexural rigidity of the plate. Ol'shanskii (1987) suggested the integral of  $w_0$  and  $p_0$  as forms of power series.

$$w_0 = \frac{1}{6} \sum_{m=0}^{\infty} (-1)^m \left\{ \frac{4}{\sqrt{3}} \left[ \frac{\eta^{6m}}{((3m)!)^2} - \frac{\eta^{6m+4}}{((3m+2)!)^2} \right] + \frac{3\eta^{6m+5}}{\Gamma^2(3m+7/2)} + \frac{6}{\pi} \frac{\eta^{6m+2}}{((3m+1)!)^2} [\ln \eta - \psi(3m+2)] \right\} \quad (3.2)$$

$$p_0 = \frac{1}{12} \sum_{m=0}^{\infty} (-1)^m \left\{ \frac{4}{\sqrt{3}} \left[ \frac{\eta^{6m}}{((3m)!)^2} - \frac{\eta^{6m+2}}{((3m+1)!)^2} \right] - \frac{3\eta^{6m+1}}{\Gamma^2(3m+3/2)} + \frac{6}{\pi} \frac{\eta^{6m+4}}{((3m+2)!)^2} [\ln \eta - \psi(3m+3)] \right\} \quad (3.3)$$

### 3.2.2 Indentation into a plate bonded to an elastic half space

Now consider the problem of a thin plate that is bonded to an elastic half space and subjected to a normal compressive force  $P$ . Both the plate and half space have the same properties given in previous section. In this section, another assumption  $\mu_f \gg \mu_s$  is used, since otherwise the plate theory would not be appropriate. Here,  $\mu$  is Lamé's constant, and  $f$  and  $s$  in subscripts denote the plate and half space, respectively.

The bonded plate will tend to restrain tangential displacement of the surface of a half space, relative to the frictionless case considered in the previous section. Two limits can be considered: one in which this displacement is completely restrained, so that the radial displacement  $u_r = 0$ ; and one in which the shear traction  $\sigma_{zr} = 0$  at  $z = 0$ . For the latter case, the surface tractions and displacements for the half space can be written in terms of

a harmonic function  $\varphi$  in the form

$$u_z(r, 0) = -\frac{(1 - \nu_s)}{\mu_s} \frac{\partial \varphi}{\partial z}(r, 0); \quad \sigma_{zz}(r, 0) = -\frac{\partial^2 \varphi}{\partial z^2}(r, 0) \quad (3.4)$$

using the superposition of Green and Zerna's solution (Barber, 2002, §19.5).

For the radially restrained case, the displacement and surface traction can be written as follows:

$$u_z(r, 0) = -\frac{(3 - 4\nu_s)}{2\mu_s} w(r, 0); \quad \sigma_{zz}(r, 0) = -2(1 - \nu_s) \frac{\partial w}{\partial z}(r, 0) \quad (3.5)$$

If the displacement  $w$  can be written in the form,

$$w = \frac{1}{2(1 - \nu_s)} \frac{\partial \varphi}{\partial z} \quad (3.6)$$

Eqs. (3.4) and (3.5) take the form

$$u_z(r, 0) = -\frac{(3 - 4\nu_s)}{4\mu_s(1 - \nu_s)} \frac{\partial \varphi}{\partial z}(r, 0); \quad \sigma_{zz}(r, 0) = -\frac{\partial^2 \varphi}{\partial z^2}(r, 0) \quad (3.7)$$

The displacement and stress in Eq. (3.7) are identical to those in the frictionless case except for the multiplying constant on  $u_z$ . In particular, for a given value of contact pressure, the displacement in the frictionless case will exceed that in the radially restrained case by the ratio

$$\frac{4(1 - \nu_s)^2}{(3 - 4\nu_s)} \quad (3.8)$$

Eq. (3.8) equals unity if  $\nu_s = 0.5$ , indicating that the problems are identical if the half space is incompressible and there will be no tangential displacements or surface shear tractions in either case. For  $\nu_s = 0$ , the ratio is  $4/3$ , showing that the stiffening effect of the radial restraint is always quite modest. For an intermediate value  $\nu_s = 0.3$ , the ratio is 1.09. Thus, the frictionless assumption seems to be a valid model for the analysis of indentation into a plate on an elastic half space. The radially restrained case can be recovered by a modest increase in the assumed half space elastic modulus. Therefore, Ol'shanskii's

solution can be used to determine the load-indentation depth relation for both frictionless case and radially restrained case.

In Eq. (3.2), the dimensionless displacement ( $w_0$ ) corresponds to the case  $\eta = 0$  at the point subjected to the load. Thus, the only non-zero term gives

$$w_0 = \frac{1}{6}(-1)^0 \frac{4}{\sqrt{3}} \frac{1}{(0!)^2} = \frac{2}{3\sqrt{3}} \quad (3.9)$$

By substituting Eq. (3.9) into Eq. (3.1), dimensional displacement is given as follows:

$$w(0, 0) = Pl^2(2D)^{-1}w_0(0) \quad (3.10)$$

After rewriting the term  $l$  using the elastic relation  $2(1 - \nu_s^2)/E_s = (1 - \nu_s)/\mu_s$ , the final dimensional expressions for the central displacement become

$$w(0, 0) = \frac{P}{3\sqrt{3}} \left( \frac{(1 - \nu_s)^2}{\mu_s^2 D} \right)^{1/3} \quad (3.11)$$

for the frictionless case and

$$w(0, 0) = \frac{P}{3\sqrt{3}} \left( \frac{(3 - 4\nu_s)^2}{16\mu_s^2 (1 - \nu_s)^2 D} \right)^{1/3} \quad (3.12)$$

for the radially restrained case.

### 3.2.3 Finite element analysis of the indentation into a plate on an elastic substrate

To examine the relevance of the plate theory, indentation into a plate on an elastic half space is simulated using a commercial finite-element code (ABAQUS/Standard). Because the solutions of the plate theory, Eqs. (3.11) and (3.12), are approximate, they are compared with the finite-element (FE) solutions that are generally considered to be correct.

Figure 3.4 shows the geometry of the model for the simulation. For convenience, the terms ‘*film layer*’ and ‘*substrate*’ are used to designate the plate and the half space, respectively. The indenter tip is modeled as rigid body with parabolic shape, and 2-dimensional linear hybrid axisymmetric elements are used for the film layer and substrate. As seen in Figure 3.4, the sliding boundary condition is applied along the axis of symmetry and the substrate’s base, while a fixed boundary condition is applied at the right edge of each layer to mimic the infinite boundary ( $u = v = 0$ ) due to the dimensional limitation of ABAQUS. This assumption should not add much error to the results.  $H_f$  and  $H_s$  are the thicknesses of the film and substrate, respectively.  $H_{tot}$  is the total thickness of the simulation model ( $H_{tot} = H_f + H_s$ ). The simulation has been done by controlling the displacement of the indenter ( $z$ ). Figure 3.5 shows the mesh configuration near the indenter tip.

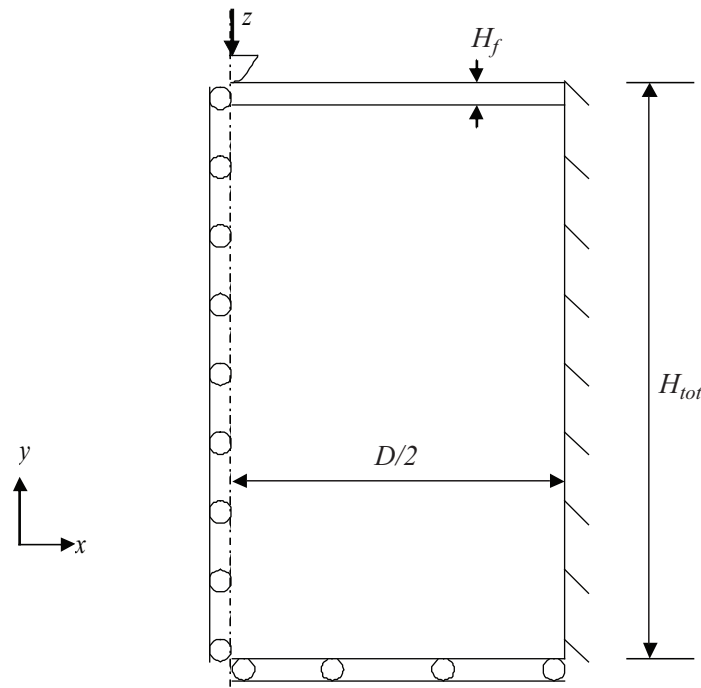


Figure 3.4: Geometry and boundary conditions for the finite element simulation

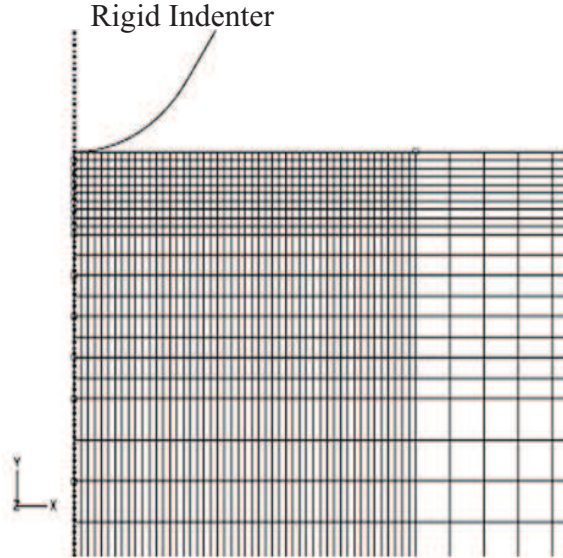


Figure 3.5: Mesh configuration near the indenter tip

Figure 3.6 shows a sample output of the simulation; force-indentation depth relation between the plate theory and a FE simulation. As shown in the figure, the FE simulation gives a result that deviated widely from the plate theory, and, furthermore, the force-indentation depth curve is non-linear. This discrepancy is outside the goals of what we consider to be the magnitude of the uncertainty in the normalized results. Because both layers are assumed to be incompressible bodies, equations (3.11) and (3.12) give the same results.

Though the FE simulation is generally accepted as a correct solution for a continuum problem, it needs to be verified for this discrepancy because it is not an exact solution. According to our assumptions, there are two possibilities for the origin of the non-linearity in the force-indentation depth curve. One is that the displacement of the indenter is not solely determined by the plate theory. The other is that the contact radius ( $a$ ) is not constant during the FE simulation. The first possibility can be explained as follows; if the radius of a rigid indenter is much smaller than the plate thickness, the film layer

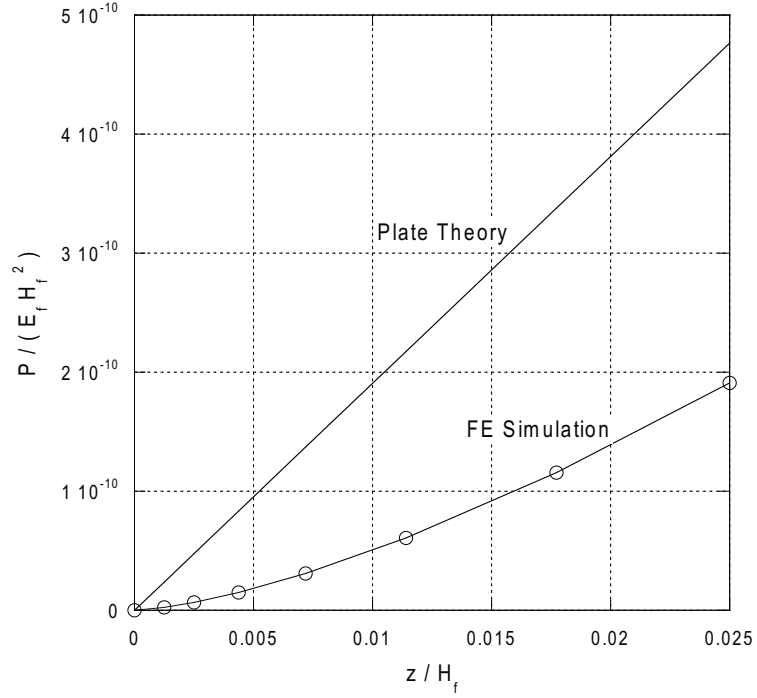


Figure 3.6: Comparison of the load-indentation depth curve between the plate theory and FE simulation; (—) the plate theory, (○) the FE simulation.

can be considered as a half space. Therefore, the problem becomes a local indentation problem. If the radius of the indenter is larger than certain critical value, the indenter can be considered as a point force and hence the plate theory will be the dominant factor of the indentation depth. Therefore, the effect of both the rigid indenter and the point force need to be considered. Based on this assumption, new FE simulation has been done using cylindrical punches with various radius  $a$ , and then we obtained force-indentation relationships close to linear. In successive simulations, we obtained results that the plate theory and FE simulation give similar results when the punch radius is much smaller than the film thickness;  $a/H_f < \sim 0.02$ . Therefore, the plate theory may not be adequate to simulate the indentation problem with rigid indenter.

To compare the plate theory and the FE simulation with a non-circular rigid indenter, the simulations are performed with different modulus. Figure 3.7 shows results that com-

pare the plate theory and the FE simulation for various modulus ratios. The dotted lines are the plate theory, and the solid lines are results of the FE simulation. Each symbol on the lines shows the modulus ratio between the film layer and the substrate. The plate theory and the FE simulation are getting closer according to increasing modulus ratio. Therefore, the information that can be obtained from the plate theory is that it could be used for a bi-layer system that the film layer is much harder than the substrate ( $E_f/E_s > \sim 1000$ ). No information about the contact radius can be obtained from the theory.

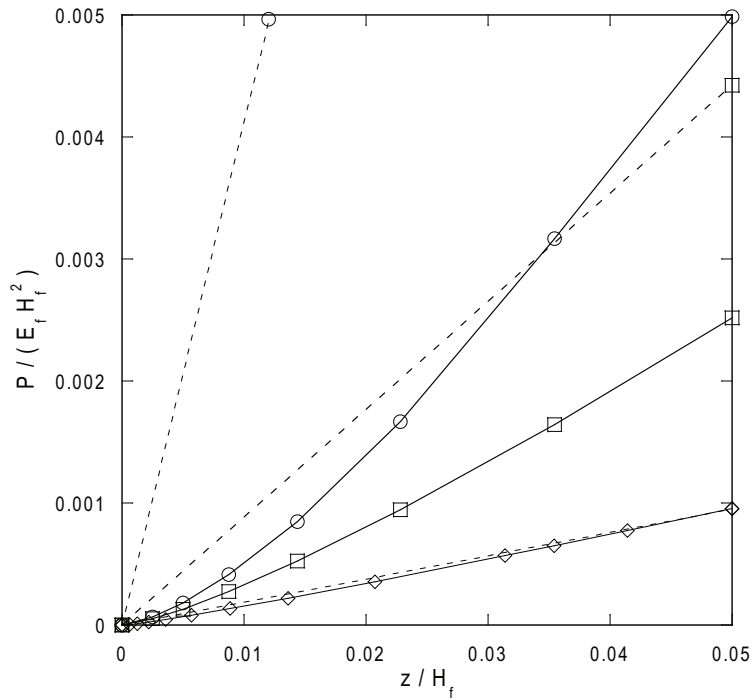


Figure 3.7: Comparison between the plate theory and the FE simulation with various modulus ratios; (- - -) the plate theory, (—) the FE simulation,  $E_f/E_s = (\bigcirc)$  10,  $(\square)$  100,  $(\diamond)$  1000.  $\nu_f = \nu_s = 0.5$ .

The second assumption can be examined by combining the plate theory with Hertz theory. For a spherical rigid indenter, the force-indentation depth relation is,

$$P = \frac{4E_f R^{1/2}}{3(1 - \nu_f^2)} w(0, 0)^{3/2} \quad (3.13)$$

where  $R$  is the radius of the rigid indenter, and  $E_f$  and  $\nu_f$  are the material properties of the plate. The Hertz theory can be added to the plate theory by adding the displacement from both theories. From Eqs. (3.12) and (3.13), a new load-displacement relation can be derived.

$$w(0,0) = \left( \frac{3(1-\nu_f^2)}{4E_f R^{1/2}} \right)^{2/3} P^{2/3} + \frac{P}{3\sqrt{3}} \left( \frac{(3-4\nu_s)^2}{16\mu_s^2 (1-\nu_s)^2 D} \right)^{1/3} \quad (3.14)$$

where subscripts  $f$  and  $s$  mean the plate and substrate, respectively.

As before, the finite-element method is used to examine the new load-indentation depth relation. The term ‘*modified plate theory*’ will be used to refer to Eq. (3.14). Figure 3.8 shows dimensionless load-indentation depth curve calculated from the modified plate theory and the finite element simulation. Though non-linear relationship is shown in this figure, there still some differences between the modified plate theory and the finite element method.

Figure 3.9 shows the effective range of the modified plate theory (left side of the line with circular symbols). Each symbol in the figure means the contact radius that the solution of the modified plate theory and the FE simulation is same at a given modulus ratio. As seen in the figure, the modified plate theory may be valid when the contact radius is much smaller ( $a/H_f < \sim 0.015$ ) and the film layer is much stiffer than the substrate ( $E_f/E_s > \sim 200$ ). In other words, the indentation depth needs to be very shallow than the thickness of the film layer ( $z/H_f < \sim 0.01\%$ ). The modified plate theory is also effective for a layered system that the modulus of film layer is much higher than that of the substrate. The flat lines in the range of moderate modulus ratios ( $30 \leq E_f/E_s \leq 200$ ) may be caused by the minimum mesh size (*i.e.* some contact points between indenter and the

film surface exist between nodes).

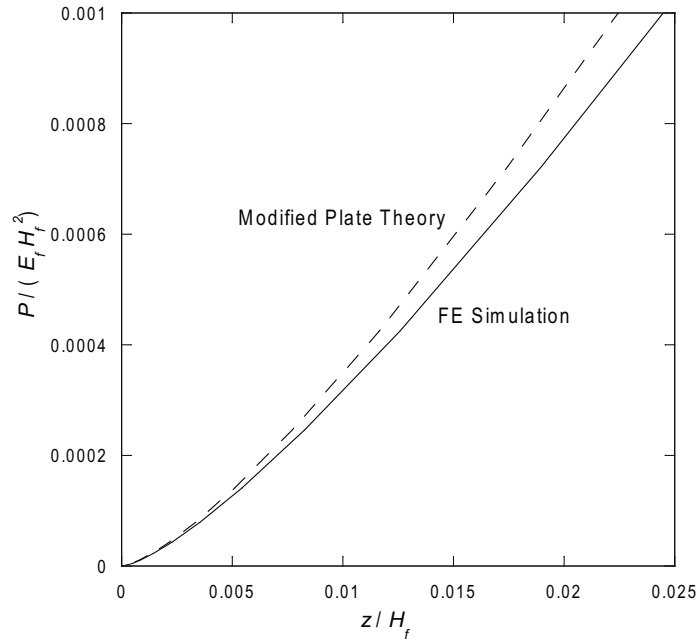


Figure 3.8: A sample comparison of the load-indentation depth curve between the modified plate theory and the FE simulation; (- - -) modified plate theory, (-) FE simulation.  $E_f/E_s = 100, \nu_f = \nu_s = 0.5$ .

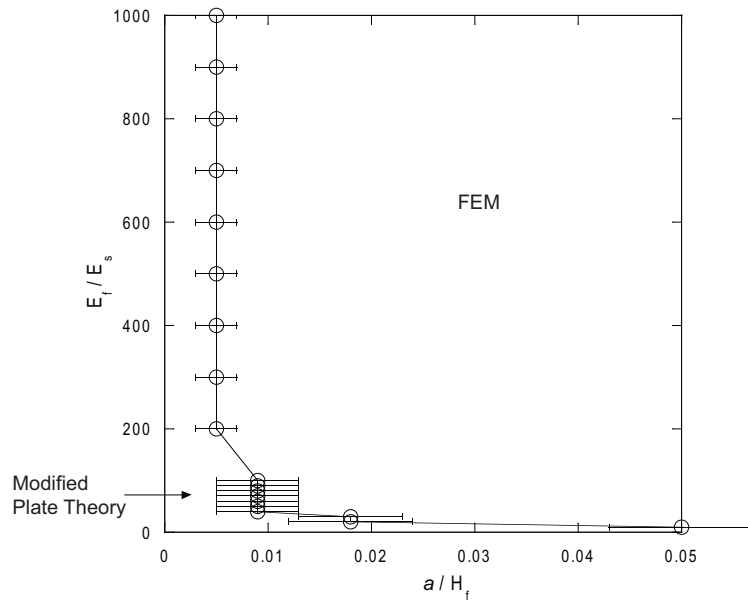


Figure 3.9: Effective range of the modified plate theory. The steps near  $a/H_f = 0.01$  may be caused by the minimum mesh sizes in the finite element simulation.

### 3.2.4 Estimation of the modulus of the surface-modified layer of PDMS

Thus far, we used the finite-element method to explore the limitations of the plate theory and a modified plate theory by simulating the indentation process. Now, we use it to find the combination of modulus and thickness of a layer, which produces a force-indentation depth relation similar to the experimental observation of Mills *et al.* (2007) for an oxidized PDMS.

Mills *et al.* (2007) suggested a method to estimate the thickness of the modified layer using the phase imaging function of AFM. They reported the thickness of a 4-minute oxidized layer being 200 nm. They also estimated the modulus of the modified layer using the plate theory (Ol'shanskii, 1987), with a substrate modulus  $E_s = 3.5\text{MPa}$  and an assumption that  $\nu_f = \nu_s = 0.5$ . When they assumed a discrete layer, they obtained the value  $E_f = 12 \pm 3\text{MPa}$ , and they obtained  $\bar{E}_0 = 37 \pm 10\text{MPa}$  with linearly graded assumption, where  $\bar{E}_0$  is surface modulus of the oxidized layer (*i.e.* plane strain modulus). Based on the parameters they reported, an attempt has been made to estimate the modulus of the film layer using the FE simulation.

Figure 3.10 shows the comparison of the FE simulation results and the force-indentation depth relation obtained from nanoindentation experiments. At moderate modulus ratios ( $E_f/E_s \sim 30, 40, 50$ ), the FE simulation results are close to the experimental data. However, modulus ratios that exist in the experimental limits are hard to find due to the non-linear relationship. The simulated force-indentation depth relationships can be fitted to the experimental data if the shallow indentation data is used. However, the modulus ratio should be high  $E_f/E_s = 100$ , therefore  $E_f$  is at least 350 MPa based on the nanoindentation data. Moreover the minimum power-law relationship (*i.e.* the exponent of power-law fitting) between the force and indentation depth of the FE simulation results is larger ( $\sim 1.33$ ) than the largest value of the experimental data (1.01). A higher modulus ratio may

produce a simulated power-law relationship that is close to the experimental data. However, the modulus of the modified layer may be unrealistically high. This leads one to the conclusion that the plate theory may be an oversimplified approximation. Therefore, another theoretical approach needs to be considered to explain the linear force-indentation depth relation.

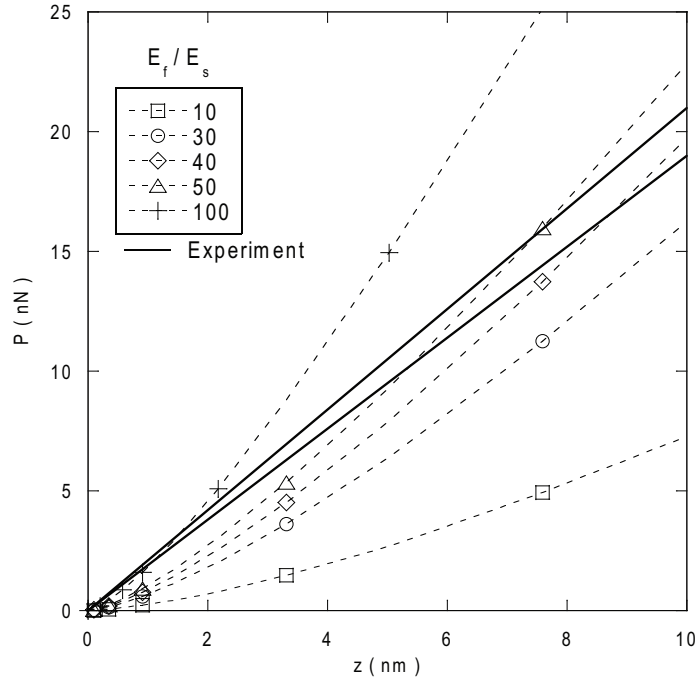


Figure 3.10: Comparison between the results of the FE simulation and the nanoindentation experiments done by Mills *et al.* (2007);  $E_f/E_s = (\square) 10, (\circ) 30, (\diamond) 40, (\triangle) 50, (+) 100$ . Solid lines are experimental results.  $\nu_f = \nu_s = 0.5$ .

Table 3.1: Power-law relationships of the FE simulation

$E_f/E_s$	Force-indentation depth relationship
10	$1.4652 \pm 0.004$
30	$1.4085 \pm 0.007$
40	$1.3912 \pm 0.007$
50	$1.3774 \pm 0.008$
100	$1.3326 \pm 0.01$

### 3.3 Indentation into an elastic half space with graded material properties

In the previous section, plate theory and a modified plate theory were examined for the indentation problem into a layered structure. In this section, the effect of a graded modulus is considered, to explore whether it causes the linearity between the force and the indentation depth. An interesting question is whether we can find an adequate grading profile that produces linearity in the force-indentation depth relation. Similar approaches have been made by other researchers (Calladine and Greenwood, 1978; Giannakopoulos and Suresh, 1997). However, their studies concerned grading profiles that increase with increasing depth. The grading profiles that decrease with increasing depth will be considered in this section. Though Giannakopoulos and Suresh (1997a,b) suggest analytical solutions for indentation with exponentially decreasing modulus, they didn't give any verification.

As in the previous sections, an analytical approach will be presented first then the finite-element method will be used to examine the limitations of the analysis.

#### 3.3.1 Indentation by a cylindrical punch

Consider the half space  $z \equiv x_3 > 0$  with the elastic constitutive law

$$\sigma_{ij} = c_{ijkl} \frac{\partial u_k}{\partial x_l}, \quad (3.15)$$

where the modulus  $c$  varies with depth according to

$$c_{ijkl} = x_3^\lambda C_{ijkl} \quad (3.16)$$

We initially consider an axisymmetric problem in which the half space is indented by a frictionless flat cylindrical punch of radius  $a$ . Here it is convenient to use cylindrical polar coordinates  $(r, \theta, z)$  with  $z \equiv x_3$ . The boundary conditions are then

$$\sigma_{zr}(r, 0) = \sigma_{z\theta}(r, 0) = 0 \quad (3.17)$$

for all  $r$ , and

$$u_z(r, 0) = \Delta; \quad 0 \leq r < a \quad (3.18)$$

$$\sigma_{zz}(r, 0) = 0; \quad r > a, \quad (3.19)$$

where  $\Delta$  and  $a$  are the displace and the radius of the punch, respectively. This is a linear problem in which the only length scale is the radius  $a$ , and hence the solutions for all  $a$  and  $\Delta$  can be mapped into each other by a linear mapping. To expose this result mathematically, we define dimensionless coordinates

$$\rho = \frac{r}{a}; \quad \zeta = \frac{z}{a}; \quad \xi_i = \frac{x_i}{a} \quad (3.20)$$

and displacements

$$U = \frac{u}{\Delta} \quad (3.21)$$

Eq. (3.16) then becomes

$$c_{ijkl} = x_3^\lambda C_{ijkl} = \xi_3^\lambda a^\lambda C_{ijkl}, \quad (3.22)$$

and the constitutive law transforms to

$$\sigma_{ij} = \Delta \xi_3^\lambda a^{\lambda-1} C_{ijkl} \frac{\partial U_k}{\partial \xi_l} \quad (3.23)$$

Substituting the stress components (3.23) into the equilibrium Eq. (3.15).

$$\frac{\partial \sigma_{ij}}{\partial x_j} = 0, \quad (3.24)$$

we obtain

$$\Delta a^{\lambda-1} C_{ijkl} \frac{\partial}{\partial x_j} \left( \xi_3^\lambda \frac{\partial U_k}{\partial \xi_l} \right) = 0, \quad (3.25)$$

which requires that

$$C_{ijkl} \frac{\partial}{\partial x_j} \left( \xi_3^\lambda \frac{\partial U_k}{\partial \xi_l} \right) = 0, \quad (3.26)$$

since  $a$  and  $\Delta$  are not zero.

The boundary-value problem is now defined as the search for a function  $U$  satisfying

$$\sigma_{zr}(\rho, 0) = \sigma_{z\theta}(\rho, 0) = 0, \quad (3.27)$$

such that

$$U_z(\rho, 0) = 1; \quad 0 \leq \rho < 1 \quad (3.28)$$

$$\sigma_{zz}(\rho, 0) = 0; \quad \rho > 1, \quad (3.29)$$

where the stress components are related to the  $U_i$  through Eq. (3.23). We notice that the boundary conditions involving stresses are all homogeneous. Thus, for example, the condition  $\sigma_{zz} \equiv \sigma_{33} = 0$  in  $\rho > 1$  and  $x_3 = 0$  becomes

$$\Delta \xi_3^\lambda a^{\lambda-1} C_{33kl} \frac{\partial U_k}{\partial \xi_l} = 0 \quad (3.30)$$

in  $\rho > 1$  and  $x_3 = 0$ . This clearly requires that

$$\xi_3^\lambda a^{\lambda-1} \frac{\partial U_k}{\partial \xi_l} = 0 \quad (3.31)$$

in  $\rho > 1$  and  $x_3 = 0$ . It follows that, since neither the governing equation nor the boundary conditions involve the dimensional parameters  $a$  and  $\Delta$ , the dimensionless boundary value problem has a universal solution for given  $\lambda$  and  $C_{ijkl}$ .

In the dimensional problem, we are interested in the total force  $F$  required to produce the indentation  $\Delta$ . The most natural way to determine this is to sum the tractions over the contact area. However, since the modulus will go either to zero or to infinity for all values of  $\lambda \neq 0$ , this will involve a limiting process. Therefore, it may be better to consider the tractions transmitted across the horizontal plane  $\xi_3 \equiv \epsilon$ , where  $\epsilon \ll 1$ , and the tractions can be allowed to tend to zero in the limit.

The normal traction on this boundary is defined by

$$\sigma_{33} = \Delta^\lambda a^{\lambda-1} C_{33kl} \frac{\partial U_k}{\partial \xi_l} (\xi_1, \xi_2, \epsilon), \quad (3.32)$$

and the total force is

$$\begin{aligned} F &= \Delta^\lambda a^{\lambda-1} C_{33kl} \int_{-\infty}^{\infty} \int_{-\infty}^{\infty} \frac{\partial U_k}{\partial \xi_l} (\xi_1, \xi_2, \epsilon) dx_1 dx_2 \\ &= \Delta^\lambda a^{\lambda+1} C_{33kl} \int_{-\infty}^{\infty} \int_{-\infty}^{\infty} \frac{\partial U_k}{\partial \xi_l} (\xi_1, \xi_2, \epsilon) d\xi_1 d\xi_2 \end{aligned} \quad (3.33)$$

The force can be written as

$$F = K a^{\lambda+1} \Delta, \quad (3.34)$$

where

$$K = \epsilon^\lambda C_{33kl} \int_{-\infty}^{\infty} \int_{-\infty}^{\infty} \frac{\partial U_k}{\partial \xi_l} (\xi_1, \xi_2, \epsilon) d\xi_1 d\xi_2 \quad (3.35)$$

is independent of  $a$  and  $\Delta$ . Thus, the effective stiffness of the indentation varies with  $a^{\lambda+1}$ .

It is worth noting here that the special case of the homogeneous half space corresponds to  $\lambda = 0$ , for which  $F$  is proportional to  $a$ , as is indeed found in the classical solution to this problem. Another special case is that the modulus is a linear function of depth ( $\lambda = 1$ ). This case was considered by Calladine and Greenwood (1978) who found that the half space then behaved like a Winkler foundation. In other words, the normal traction is linearly proportional to the local indentation and is unaffected by displacements at other locations of the surface. In this case, it follows immediately that the force required to produce an indentation of a given depth is proportional to the area of the indenter planform and hence, in the present case, to  $a^2$ , which again is consistent with the above general result.

### 3.3.2 Indentation by a power-law shaped punch

Suppose now that the half space is indented by a punch whose profile is defined by a power law ( $z = Cr^\beta$ ), so that the boundary conditions are

$$\sigma_{zr}(r, 0) = \sigma_{z\theta}(r, 0) = 0 \quad (3.36)$$

for all  $r$ , and

$$u_z(r, 0) = \Delta - Cr^\beta; \quad 0 \leq r < a \quad (3.37)$$

$$\sigma_{zz}(r, 0) = 0; \quad r > a \quad (3.38)$$

where  $C$  is a constant. Since the punch is smooth, the contact radius ( $a$ ) is a dependent variable if either the force  $F$  or the indentation  $\Delta$  is prescribed. The force  $F$  and  $\Delta$  cannot be prescribed at the same time.

Alternatively, the contact radius ( $a$ ) can be an independent variable if both  $F$  and  $\Delta$  are allowed to be dependent. The extra condition needed to determine  $\Delta$  is the fact that the gap must be positive outside the contact area and the traction compressive inside. An equivalent formulation is that the displacement gradients be continuous at the edge of the contact area. With this formulation, the boundary value problem can be defined in terms of displacement gradients alone, giving

$$\sigma_{zr}(r, 0) = \sigma_{z\theta}(r, 0) = 0 \quad (3.39)$$

for all  $r$ , and

$$\frac{\partial u_z}{\partial r}(r, 0) = -C\beta r^{\beta-1}; \quad 0 \leq r < a \quad (3.40)$$

$$\frac{\partial u_z}{\partial r}(a^-, 0) = \frac{\partial u_z}{\partial r}(a^+, 0) \quad (3.41)$$

$$\sigma_{zz}(r, 0) = 0; \quad r > a \quad (3.42)$$

This time, we cannot use  $\Delta$  to normalize  $u$ , so we shall leave it in dimensional terms, giving

$$\sigma_{zr}(\rho, 0) = \sigma_{z\theta}(\rho, 0) = 0 \quad (3.43)$$

for all  $\rho$ , and

$$\frac{\partial u_z}{\partial \rho}(\rho, 0) = -C\beta a^\beta \rho^{\beta-1}; \quad 0 \leq \rho < 1 \quad (3.44)$$

$$\frac{\partial u_z}{\partial \rho}(1^-, 0) = \frac{\partial u_z}{\partial \rho}(1^+, 0) \quad (3.45)$$

$$\sigma_{zz}(\rho, 0) = 0; \quad \rho > 1, \quad (3.46)$$

where the stress components are related to the  $u_i$  through

$$\sigma_{ij} = a^{\lambda-1} \xi_3^\lambda C_{ijkl} \frac{\partial u_k}{\partial \xi_l} \quad (3.47)$$

The modified problem defined by

$$\sigma_{zr}(\rho, 0) = \sigma_{z\theta}(\rho, 0) = 0 \quad (3.48)$$

for all  $\rho$ , and

$$\frac{\partial u_z}{\partial \rho}(\rho, 0) = -\rho^{\beta-1}; \quad 0 \leq \rho < 1 \quad (3.49)$$

$$\frac{\partial u_z}{\partial \rho}(1^-, 0) = \frac{\partial u_z}{\partial \rho}(1^+, 0) \quad (3.50)$$

$$\sigma_{zz}(\rho, 0) = 0; \quad \rho > 1, \quad (3.51)$$

has a solution  $u_i = U_i(\xi_1, \xi_2, \xi_3)$  that is independent of  $a$  and it is clear that the solution of the problem of (3.30)-(3.33) is

$$u_i = C\beta a^\beta U_i(\xi_1, \xi_2, \xi_3) \quad (3.52)$$

Substituting this result into Eq. (33), we have

$$\sigma_{ij} = C\beta a^{\lambda+\beta-1} \epsilon^\lambda C_{ijkl} \frac{\partial U_k}{\partial \xi_l}, \quad (3.53)$$

and the total force is

$$\begin{aligned} F &= C\beta a^{\lambda+\beta-1} \epsilon^\lambda C_{ijkl} \int_{-\infty}^{\infty} \int_{-\infty}^{\infty} \frac{\partial U_k}{\partial \xi_l} (\xi_1, \xi_2, \epsilon) dx_1 dx_2 \\ &= C\beta a^{\lambda+\beta+1} \epsilon^\lambda C_{ijkl} \int_{-\infty}^{\infty} \int_{-\infty}^{\infty} \frac{\partial U_k}{\partial \xi_l} (\xi_1, \xi_2, \epsilon) d\xi_1 d\xi_2 \\ &= C\beta a^{\lambda+\beta+1} \mathcal{F}, \end{aligned} \quad (3.54)$$

where,

$$\mathcal{F} = \epsilon^\lambda C_{ijkl} \int_{-\infty}^{\infty} \int_{-\infty}^{\infty} \frac{\partial U_k}{\partial \xi_l} (\xi_1, \xi_2, \epsilon) d\xi_1 d\xi_2 \quad (3.55)$$

Thus,  $\Delta$  is independent of the contact radius  $a$ .

Consequently, the relation between the force ( $F$ ) and the contact radius ( $a$ ) is of the form

$$F \sim a^{\lambda+\beta+1} \quad (3.56)$$

The central displacement (*i.e.* indentation depth) is

$$\Delta = u_3(0, 0, 0) = C\beta a^\beta U_3(0, 0, 0) \quad (3.57)$$

From Eqs. (3.56) and (3.57), the relation between force and indentation depth can be expressed as follows,

$$F \sim \Delta^{(\lambda+\beta+1)/\beta} \quad (3.58)$$

In particular,  $F$  is linearly proportional to  $\Delta$  if

$$\frac{\lambda + \beta + 1}{\beta} = 1 \quad (3.59)$$

or

$$\lambda = -1 \quad (3.60)$$

for all shapes of punch. In other words, the linearity can be obtained if the modulus is inversely proportional to depth. Notice that this result is independent of  $\beta$ —*i.e.* if  $\lambda = -1$ , the linearity can be obtained for indenters of all power-law shapes. Giannakopoulos and Suresh (1996) have done a similar analysis with simple power law ( $E = E_0 z^k$ ). They defined  $E_0$  (Pa m<sup>-k</sup>) as the modulus of homogeneous soil ( $k = 0$ ) and  $k$  is dimensionless exponent ( $0 \leq k < 1$ ). However, there is no reason that most  $k$  be positive even if there are singularities near the sharp edge of an indenter (This is confirmed by a personal communication). Thus, the entire range of  $\lambda$  ( $-1 \leq \lambda \leq 1$ ) will be considered in this research.

Figure 3.11 shows the graphic model of a simple power law. If  $\lambda$  is positive, the modulus increases according to the increasing depth. If  $\lambda = 0$ , the modulus is same as the homogeneous half space. If  $\lambda = 1$ , the modulus behaves well known Gibson soil (Gibson, 1967). This type of distribution has been used in geomechanics which deals with soils, sands, clay and rocks. If  $\lambda$  is negative the modulus decays as the depth increases, and it has a singularity at  $z = 0$ .

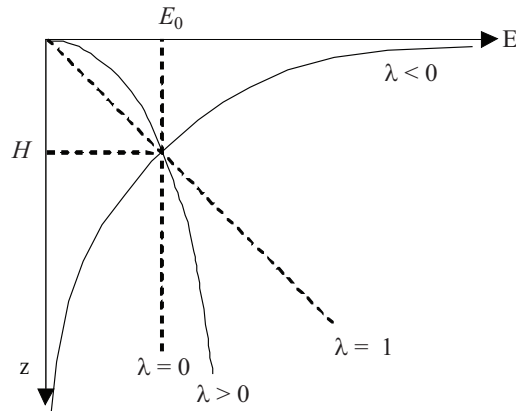


Figure 3.11: Graphic model of a simple power law  $E = E_0(z/H)^\lambda$  ( $-1 \leq \lambda \leq 1$ )

### 3.3.3 Finite-element analysis of the indentation into an elastic half space with power law grading modulus

To examine the relevance of the power law, another series of FE simulations have been performed with a modulus distribution which follows the power law. A simple power law is used for the simulation.

$$E = E_0 \left( \frac{z}{H} \right)^\lambda \quad (3.61)$$

where  $-1 \leq \lambda \leq 1$ ,  $E_0$  is the modulus at the surface of the half space,  $H$  is arbitrary length added for the non-dimensionalization purpose. When the exponent  $\lambda$  is negative, the power law becomes infinite at  $z = 0$ . However, it is impossible to assign an infinite surface modulus in the finite-element simulation. To avoid this problem, a simple truncation method is considered, which is shown in the Eq. (3.62) and Figure 3.12. The term ‘*constant truncation*’ will be used to refer to this truncation method.

$$\begin{aligned} E &= E_0 \quad 0 \leq z \leq H \\ E &= E_0 \left( \frac{z}{H} \right)^\lambda \quad H < z \leq H_{tot} \end{aligned} \quad (3.62)$$

To model the continuously varying modulus, the half space is divided into 38 layers; thinner layers near the surface and thicker layers near the bottom (Figure 3.13). The thickness of the thinnest layers is 1/50000 of the total thickness. The values of the modulus are calculated from the power law at each node along the  $z$  axis, and then an average value of the two nodes is used as the modulus of each layer (*i.e.* the stepped solid line in Figure 3.12).

The geometry and mesh configuration are the same as these used in the simulations of the bi-layer system, and the assumption of incompressible materials ( $\nu = 0.5$ ) is still effective for the half space. A power law ( $z = Cr^2$ ) is used to describe the shape of the

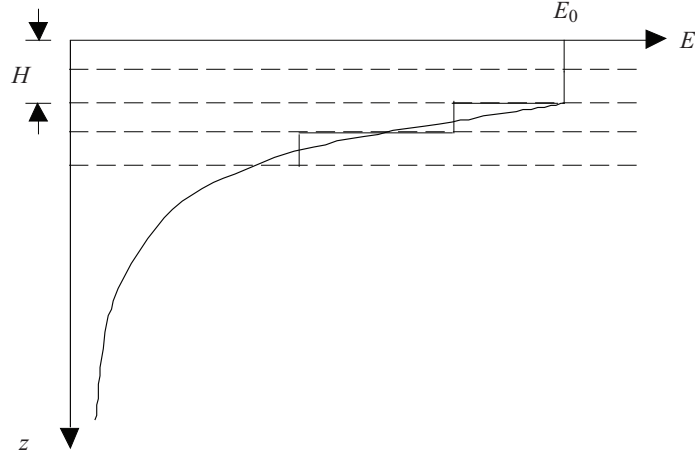


Figure 3.12: Schematic of the simple truncation method. The value of the surface modulus ( $E_0$ ) is used for the first layers. This is a non-scaled picture to show the truncation and discretization methods.

indenter, where  $C = 0.025(nm^{-1})$  which is equivalent to the radius of the spherical part of an AFM tip. Possible length scales that can be used are the overall thickness ( $H_{tot}$ ), the arbitrary length scale ( $H$ ), and the constant for indenter shape function ( $C$ ). Because the substrate was modeled as a half-space ( $H/H_{tot} = 0$ ), the total thickness should not give a significant error to the results. To check the effect of the total thickness, test simulations were run with three thickness ratios ( $H/H_{tot} = 0.001, 0.002, 0.005$ ) for the inverse power law ( $\lambda = -1.0$ ). The error of the dimensionless force-indentation depth relationships were less than 1% for both the constant and quadratic truncation. Thus, the constant ( $C$ ) is used for the non-dimensionalization of the simulation results.

Figure 3.14 shows the force-indentation depth relations of the inverse power law ( $\lambda = -1$ ), which are obtained from the FE simulation. While the linear force-indentation depth relation is expected at  $\lambda = -1.0$ , the force-indentation depth curve is not linear even on the log-log scale as seen in the figure. Thus, the exponent was calculated using a curve fitting technique (power-law fitting) to compare the FE simulation and the theory. This non-linearity may be caused by the parameters used in the numerical simulation such as

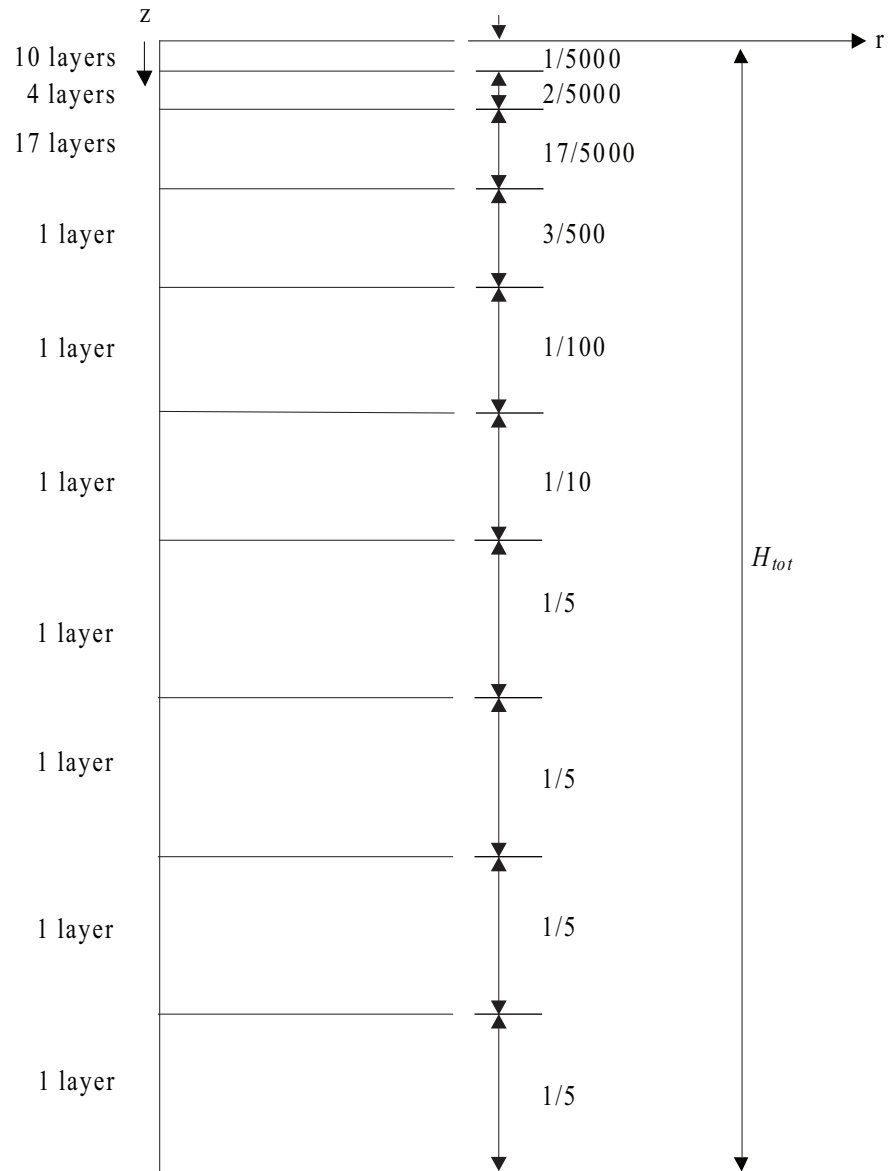


Figure 3.13: Discretization of the body to apply the graded material properties. Numbers in right side are the ratio of each layer to the total thickness ( $h_i/H_{tot}$ ), where  $h_i$  is thickness of  $i$ -th layer. This is a non-scaled picture.

the size of the body (*i.e.* the model is not a half space), the truncated and discretized modulus distribution, or boundary conditions.

Figure 3.15 shows the comparison between the FE results and the power law for entire range of  $\lambda$  ( $-1 \leq \lambda \leq 1$ ). Though the slopes are slightly overestimated along the entire range of  $\lambda$ , the relations seem to be close to the theoretical values. Thus, the power law may be a adequate model to describe the linearity of the force-indentation depth relation that is shown in the experiment, and it can be used to find the modulus value at the surface of the half space.

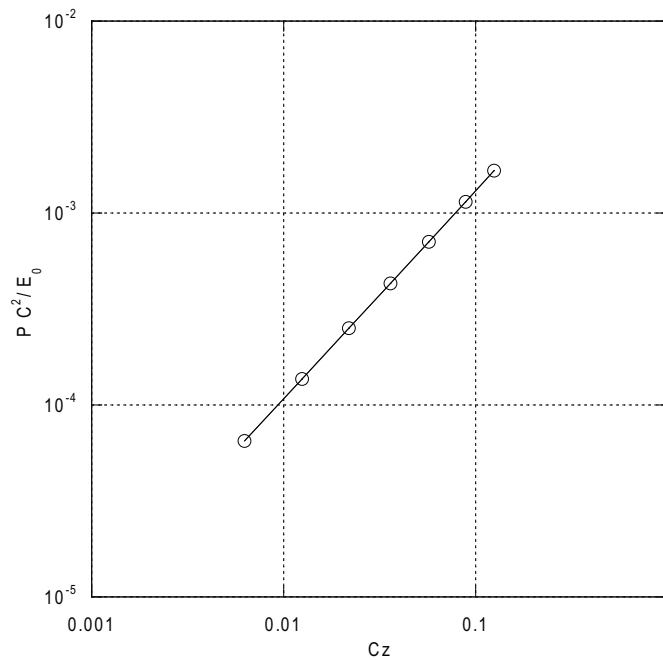


Figure 3.14: Non-dimensional force-indentation depth relationship for the inverse power law ( $\lambda = -1$ ). The constant truncation method is used for the FE simulation.

For the inverse power law ( $\lambda = -1.0$ ), another simple truncation method is derived that can consider the characteristic of the oxidation process. Equation (3.63) shows the second truncation method, which uses a quadratic decaying function within the length scale. The term ‘*quadratic truncation*’ will be used to refer to this truncation method.

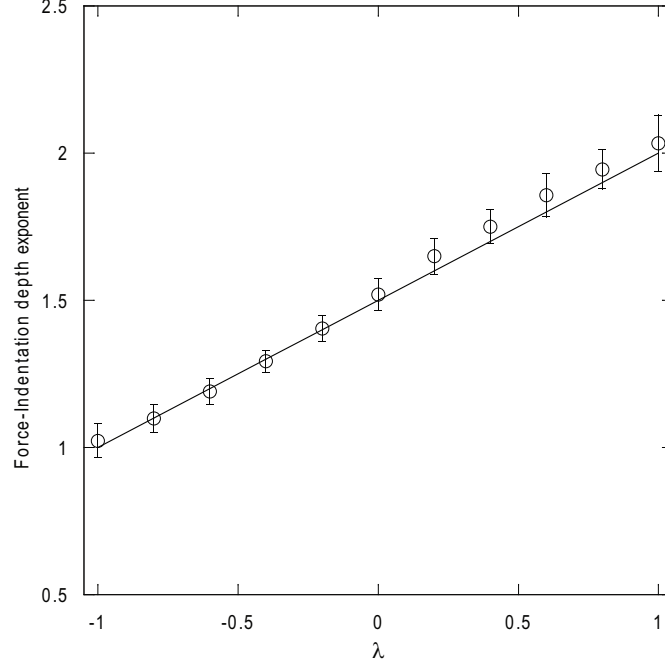


Figure 3.15: Comparison of the force-indentation depth relationship between the power law and FE simulation. The solid line is the power law and the circular symbols are the results of the FE simulation.  $CH = 0.025$ ,  $E_f/E_s = 100$ ,  $\nu = 0.5$ .

$$\begin{aligned}
 E &= E_0 + (E_h - E_0) \left(\frac{z}{H}\right)^2 & 0 \leq z < H \\
 E &= E_h \left(\frac{H}{z}\right) & H \leq z < H_{tot}
 \end{aligned} \tag{3.63}$$

where,  $E_0$  is the surface modulus,  $E_h$  is the modulus at  $z = H$ , and  $H$  is the length scale (Figure 3.16). Because the modified layer is formed by an oxidation process and the surface may be saturated during the process, quadratic decay may be a possible assumption. The unknown modulus  $E_h$  can be derived using the continuity conditions at  $z = H$  ( $E_1 = E_2, \partial E_1/\partial z = \partial E_2/\partial z$ ). Thus, the final form of the second truncation method is,

$$\begin{aligned}
 E &= E_0 \left[1 - \frac{1}{3} \left(\frac{z}{H}\right)^2\right] & 0 \leq z < H \\
 E &= \frac{2}{3} E_0 \left(\frac{z}{H}\right) & H < z < H_{tot}
 \end{aligned} \tag{3.64}$$

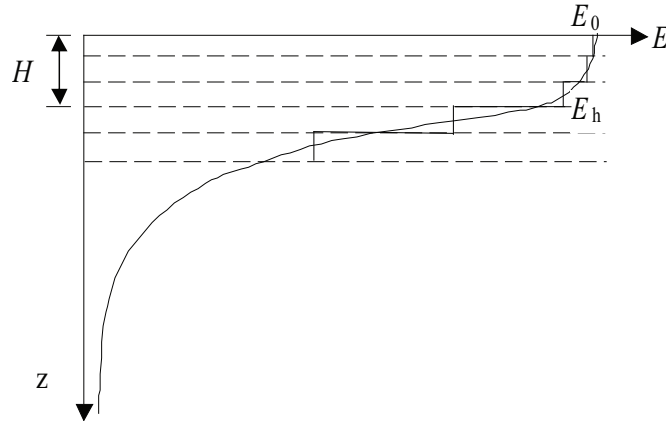


Figure 3.16: Schematic of the quadratic truncation method. This is non-scaled picture to show the truncation method.

Figure 3.18 show the effect of the length scale in the truncation methods. Before comparing the exponents of the relationships for both truncation methods, force-indentation depth curves are examined to check the quadratic truncation method (Figure 3.17). As seen in Figure 3.17, the quadratic truncation method also shows relationships close to linear on log-log scale plot.

Regardless of the truncation method, the exponent of the function approaches to the theoretical value with respect to the decreasing length scale. However, the exponent of the constant truncation is always larger than that of the quadratic truncation. This may be a natural result because the modulus of the quadratic truncation decays more rapidly than the constant truncation. The two truncation methods would give the same value of exponent at the infinitely short length scale. However, this requires additional calculation cost (time and effort). Thus, the slope of  $\sim 1.08$  is the best result that can be obtained with the current geometry and mesh configuration, and the quadratic truncation seems to be a better model for the profile of the inverse power law.

One interesting question is whether the power law is the only possible model to obtain the linear force-indentation depth relation. To check this question, the error function is

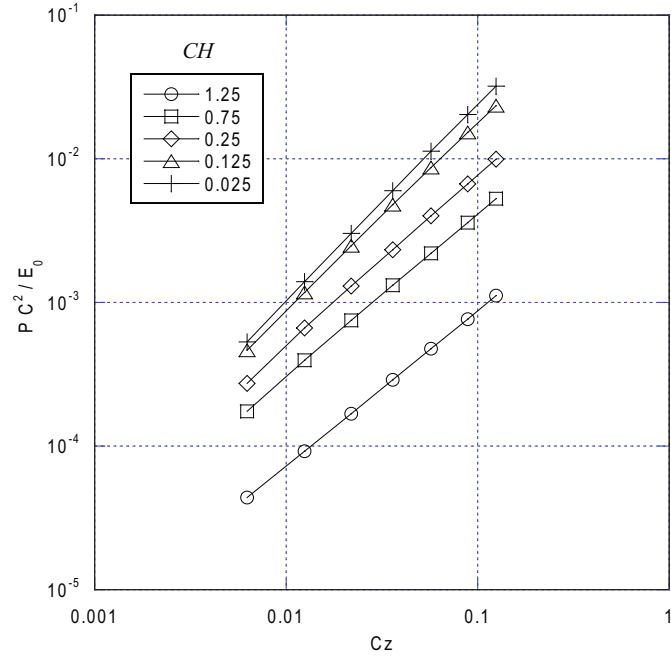


Figure 3.17: Nondimensional force-indentation depth curves of the quadratic truncation with respect to the length scales;  $CH = (\circ)$  1.25,  $(\square)$  0.75,  $(\diamond)$  0.25,  $(\triangle)$  0.125, and  $(+)$  0.025.  $\nu = 0.5$

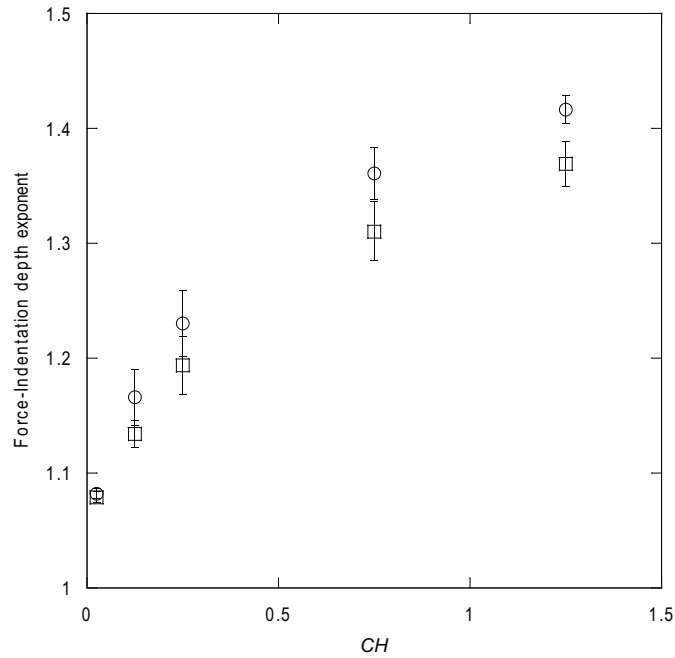


Figure 3.18: Comparison of the force-indentation depth relations between the truncation methods;  $(\circ)$  the constant truncation,  $(\square)$  the quadratic truncation. The bar in each symbol means the errors caused by the power-law fitting.

considered as an alternative model for the modulus distribution.

$$E = E_s + (E_0 - E_s)\text{erfc}\left(\frac{z}{H}\right) \quad (3.65)$$

where  $E_0$  and  $E_s$  are modulus at the surface and in the substrate, respectively.  $H$  is the length scale. Because the error function is often used to denote a diffusion process in material and thermal area, it may be a more realistic expression than the power law. Figure 3.19 shows the graphic model of the modulus distribution of Eq. (3.65).

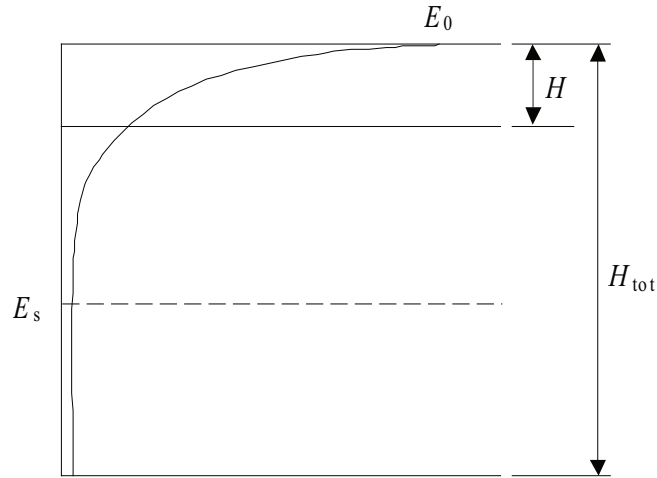


Figure 3.19: Graphic model of the error function.

Figure 3.20 shows the force-indentation depth curves for the error functions with respect to the modulus ratios  $E_0/E_s$ . With the error function, we obtained the curves that are very close to a linear relationship on the linear scale plot when  $E_0/E_s > \sim 10^4$ . Figure 3.21 shows the magnitude of the exponent of the force-indentation depth curves for the error function. As seen in the figure, the relationships decrease with increasing modulus ratio and seem to converge to unity at any value of length scale. The largest converged exponent ( $\sim 1.01$ ) is in the range of nanoindentation experiments performed by Mills *et al.* (2007) ( $0.98 \sim 1.01$ ). The exponent of the inverse power law is out of this range. There-

fore, the error function may be a better approximation for the graded modulus.

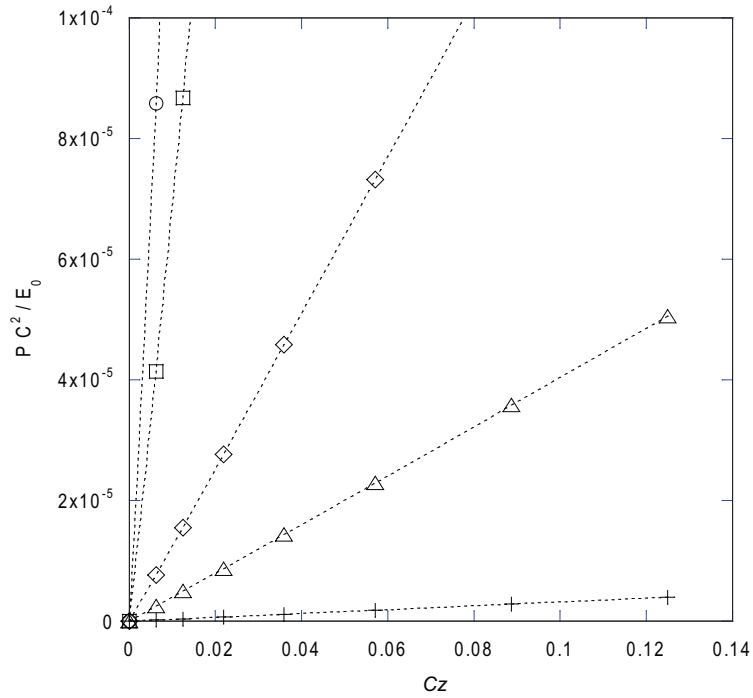


Figure 3.20: Force-Indentation depth curves for the error function;  $E_0/E_s = (\circ)$  10,  $(\square)$   $10^2$ ,  $(\diamond)$   $10^3$ ,  $(\triangle)$   $10^4$  and  $(+)$   $10^5$ .  $CH = 0.025$ ,  $\nu = 0.5$

The comparison between the quadratically truncated power law and the error function is shown in Figure 3.22. For the comparison, different modulus ratios ( $E_0/E_s$ ) are taken for each length scale ( $CH$ ). For example, the modulus ratio is about  $10^5$  at  $CH = 0.025$ . The error function always shows the relationships closer to the theoretical limit than the quadratically truncated power law.

Consequently, any function whose profile is similar to the power law could be the modulus distribution for an indentation simulation, and among the possible distribution, the error function shows good linearity in the force-indentation depth relationships.

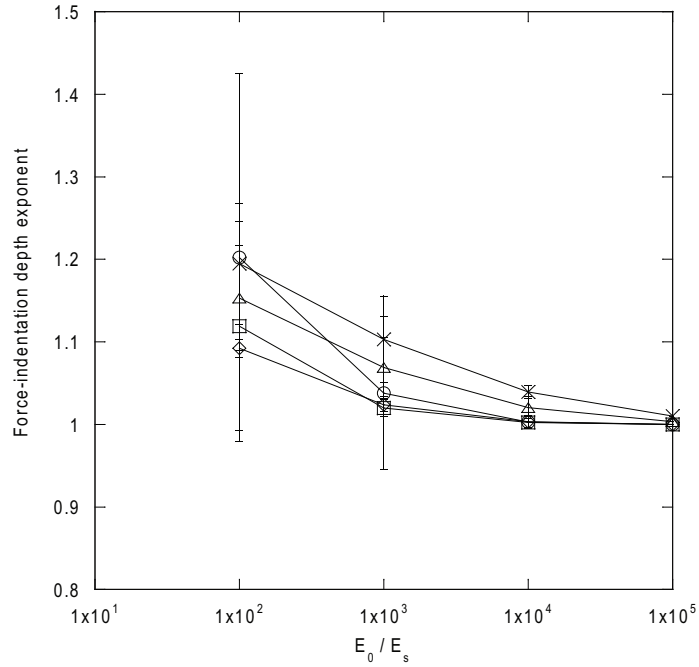


Figure 3.21: Force-Indentation depth relationships for the error function.  $CH = (\bigcirc)$  0.025,  $(\square)$  0.05,  $(\diamond)$  0.1,  $(\triangle)$  0.5,  $(\times)$  1.0. The bar in each symbol means the errors caused by the power-law fitting.

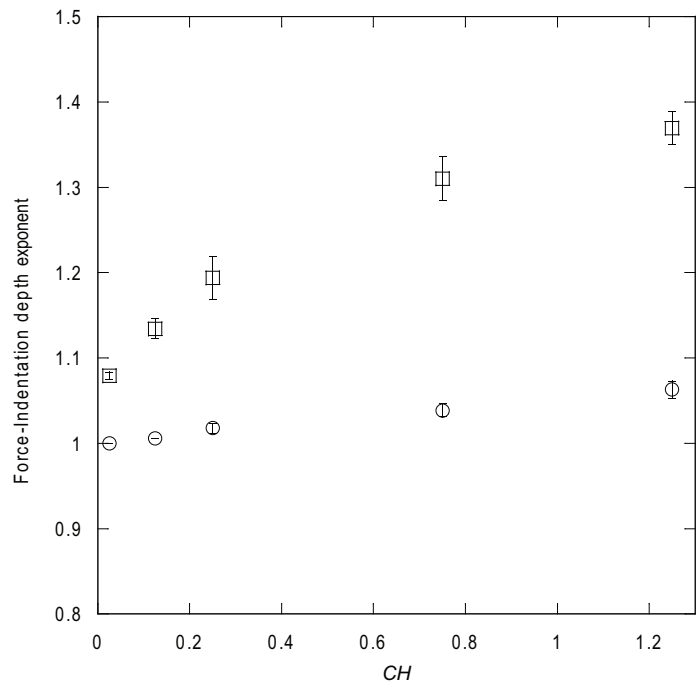


Figure 3.22: Comparison of the force-indentation depth relationships between the power law (quadratic truncation) and the error function;  $(\bigcirc)$  the error function,  $(\square)$  the power law with quadratic truncation. The bar in each symbol means the errors caused by the power-law fitting.

### 3.4 Estimation of the modulus of an oxidized PDMS

In Sections 3.2 and 3.3, indentation theories the plate theory and a power law were explored to explain the linear force-indentation depth relation that is obtained from experiments done by Mills *et al.* (2007). Through a series of analyses, we found possibilities that the graded modulus can cause the observed force-indentation depth relation to be linear. Two functions, the power law and the error function, were examined using the FE simulation. The error function shows good linearity than the power law, and shows almost perfect linearity under certain simulation conditions.

An iterative procedure will be introduced in this section, which can be applied for the estimation of the mechanical properties surface modulus and thickness of the oxidized layer using the analyses for indentation and the quantities that are measured.

#### 3.4.1 Iterative procedure to determine the modulus of oxidized layer

The error function is used for the profile of the graded modulus based on the analysis of Section 3.3. To use the error function, two variables, surface modulus ( $E_0$ ) and scale length ( $H$ ), need to be determined. There is additional unknown property, Poisson's ratio of the oxidized layer, that taken to be 0.5, with the assumption that both oxidized and unoxidized regions are incompressible. If we can find a force-indentation depth curve based on assumed values of the surface modulus ( $E_0$ ) and length scale ( $H$ ), and the curve is in the range of results of indentation experiments (Figure 3.1),  $E_0$  can be considered as the modulus at surface of an oxidized PDMS, and  $H$  can be used to determine the thickness of the layer. The thickness of the modified layer can be approximated as about  $3H$  based on the property of the error function. However, arbitrary guesses of the values may cause enormous computational cost. Therefore, a more systematic approach needs to

be implemented. This is done by introducing the result from Chapter II, the wavelength as a function of dimensionless modulus for an elastic half space that has graded material properties.

As seen in Figure 3.23, wavelengths are a weak function of the modulus ratio. In other words, large changes in modulus ratio cause rather small changes in the dimensionless wavelength. Therefore, if we have a given value of wavelength, the length scale in the modulus distribution can be determined. Consequently, the change of modulus ratio, which is used to match the results of indentation simulation to the results of indentation experiment, makes the length scale converge to a certain value. The detail procedure is shown in Figure 3.24.

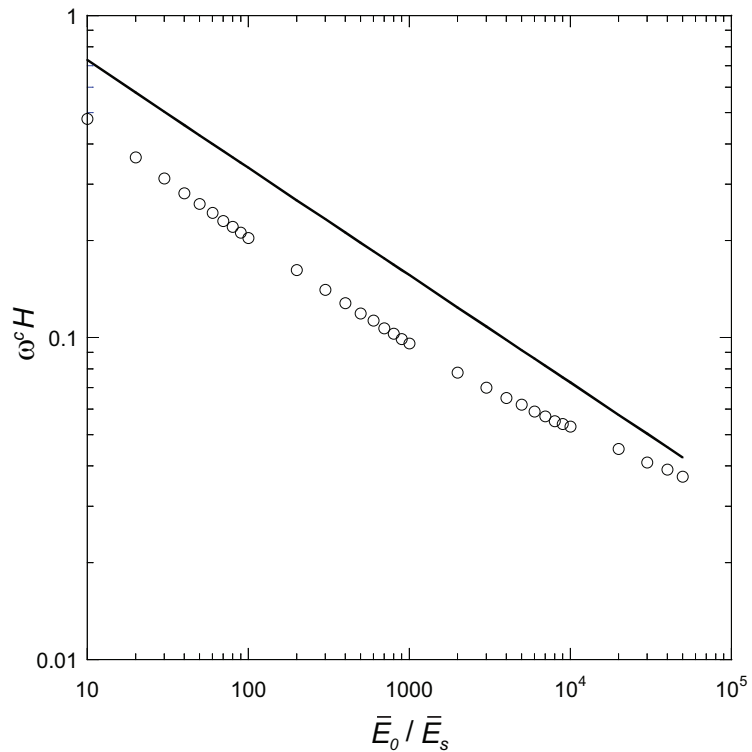


Figure 3.23: Dimensionless wavenumbers for error function grading. The solid line represents a homogeneous layer approximation using Eqs. (2.24) and (2.25).

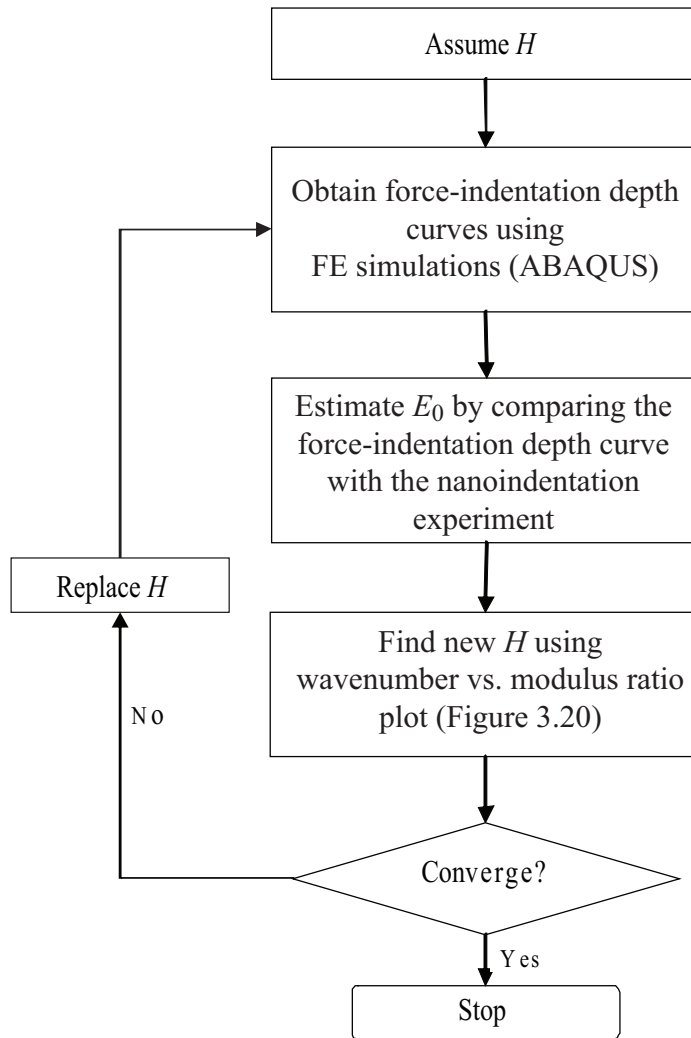


Figure 3.24: Flow chart for the iterative procedure to estimate surface modulus and thickness of the oxidized layer of PDMS

The iterative method is tested using experiment data <sup>1</sup> ; wavelength  $\sim 1340$  nm and the modulus of the bulk PDMS  $E_s \sim 3.5$  MPa. For the FE simulation, same conditions that are used in Section 3.3 are used. The values determined from this test are  $E_0 \sim 31.5$  GPa and  $H \sim 11.5$  nm (*i.e.* the thickness of the oxidized layer is about 35 nm). While the procedure seems to be an effective method to find unknown properties of a modified surface, the value of surface modulus is higher than expected. Mills *et al.* (2007) suggested that the surface modulus is  $E_0 \sim 27.75$  MPa with the assumption of linearly graded modulus using the plate theory.

### 3.4.2 Effect of residual strain

An iterative method is introduced in preceding section, which can be used to evaluate the surface modulus of an oxidized PDMS. However, test results showed unrealistically high value of surface modulus. One potential cause of the result is residual strain. Because the PDMS is heated during an oxidation process, residual strains may be produced when it is cooled down. Previous studies reported the effect of residual stresses on indentation hardness, which decreases with tensile stress and increases with compressive stress (Suresh and Giannakopoulos, 1998; Swandener *et al.*, 2001). However, the residual strain is hard to be determined from the experiments directly. Thus, small tensile strains are applied to the right edge of the FE model in Figure 3.4 to produce strains in the structure.

Table 3.2 shows the values of surface modulus and length scale obtained from the FE simulations according to the applied tensile strains. In the table, the surface modulus decreases about factor of 1/2 when the applied strain (*i.e.* residual strain) increases twice. Table 3.3 shows the homogeneous layer approximation of the results of the FE simulations calculated by Eqs. (2.24) and (2.25). When the applied strain is 4 %, the modulus

---

<sup>1</sup>All specific data are refer to the data obtained by Mills *et al.* (2007)

ratio is  $E_f/E_s \sim 35$  that seem to be much realistic value than the values in the preceding section. In Table 3.2 and Table 3.3, the change of surface modulus seems to be sensitive to the change of residual strains. Therefore, if there are more sophisticate methods to estimate the residual strain, the surface modulus may converge to closer values of the modulus and thickness.

Table 3.2: The surface modulus and length scale estimated by the iterative FE simulation

Applied tensile strain(%)	$E_0$ (MPa)	$H_f$ (nm)	Estimated thickness of the modified layer ( $\sim 3H$ )
0.5	4375	19.5	58.5
1	2275	23	72
2	1260	28	84
3	875	32.75	98.25
4	682.5	35	105

Table 3.3: Homogeneous layer approximation of the results of the iterative FE simulations

Applied tensile strain(%)	$E_f$ (MPa)	$H_f$ (nm)
0.5	795	17.3
1	425	20.4
2	228	24.8
3	152	29
4	123.5	31

For the estimation of the residual strain, an approximation can be made by observing open cracks that remain on an oxidized PDMS after releasing strain in tensile experiments. If there are residual strains in the oxidized layer, these strains will not be recovered after releasing the applied strain.

Table 3.4 shows lengths of crack spacing and their widths. The widths and spaces were measured after relaxing 10% applied strain. Figure 3.25 shows how to estimate the residual strain from the experimental data. The residual strain is calculated using the values in the

dotted box by dividing the sum of crack widths by the sum of average crack spacings, and  $\sim 2.85\%$  and  $\sim 2.95\%$  strains are calculated from both experiment set, respectively. These values seem to be quite relevant each other, and these are in the range of the finite element simulation. Therefore, no further simulation has been conducted.

Table 3.4: Crack spaces and widths obtained by a nanoindentation experiment. The question marks mean no data has been obtained.

Crack Experiment Set	Width(nm)	Space( $\mu$ m)
Set 1	?	12.8
	?	7.03
	250	5.4
	214	10.6
	319	5.7
	290	5.6
Set 2	9.3	?
	147	2.95
	218	9.5
	?	9.6

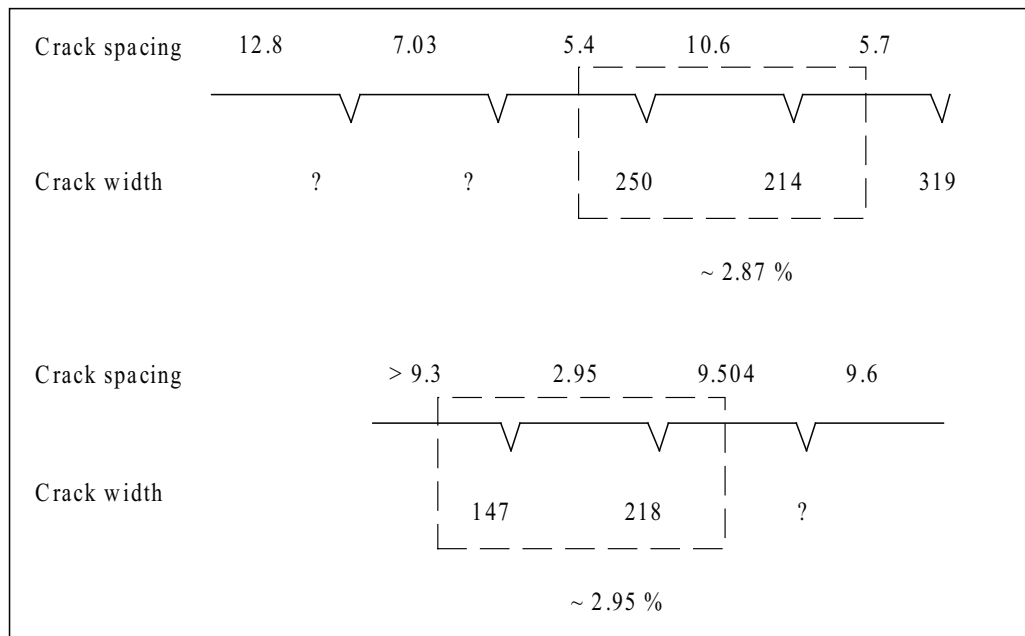


Figure 3.25: Estimation of residual strain from the geometry of cracks that is produced by releasing 10 % tensile strain produced by Mills *et al.* (2007)

### 3.5 Conclusions

Indentation theories are explored to explain the linear force-indentation depth relationships obtained from nanoindentation experiments. The plate theory is reviewed and compared with the finite-element method. There are two significant differences between the plate theory and the FE simulation; non-linear force-indentation relationship and indentation force at same depth.

To explain the non-linearity, we suggest a modified theory that combines the plate theory and Hertz theory for global and local indentation behavior, respectively. This modified theory showed non-linear behavior, and the effective limits of the modified theory are examined with the FE simulation. Though non-linear relationship is found, the FE simulation is not able to fit the simulation results into the experimental data due to the high non-linearity in the force-indentation depth relation. An indentation problem is modeled with graded modulus in an elastic body using a power law. A condition is obtained, which could show linear force-indentation depth relation. Though the FE simulation gave moderate non-linear force-indentation depth curves, the slopes were much closer to the linear relation.

An iterative procedure is introduced as a mean to evaluate the surface modulus and thickness of a surface-modified layer of PDMS based on the indentation theory suggested in this chapter and critical wrinkling conditions produced in Chapter II. The effect of residual strain has been considered. We have found that increasing residual strain decreases the modulus at the modified surface. Though the modulus evaluated by this iterative method show higher value than previous research, the values of modulus exist in acceptable range. Therefore, this method can be used as a mean to characterize a thin hard layer on a soft substrate.

## CHAPTER IV

# WRINKLING IN A SURFACE-MODIFIED LAYER OF POLY (DIMETHYLSILOXANE)

### 4.1 Introduction

Since it has been revealed that the hydrophobic surface of PDMS can be changed to a hydrophilic surface using oxidation techniques (Hansen *et al.*, 1965), the modified surface has been used in various research areas, which requires wettable surface; for example, microfluidics (Jo *et al.*, 2000) and soft lithography.

In addition to the chemical change of the PDMS surface, researchers have also found that a thin hard layer is formed by oxidation. This hard layer has been considered as an experimental platform to form small scale structures. Instead of structures built by adding or removing parts, researchers have tried to form micro-/nano-scale structures using spontaneous wrinkles that can be formed by applying deformation to the layer. Thermal expansion (Huck *et al.*, 2000; Bowden *et al.*, 1999) and mechanical stretching (Volynskii *et al.*, 2000; Watanabe, 2005) are well known techniques to apply strains in the layer. Many applications have used the wrinkles. Well known applications that utilize the wrinkles are diffraction gratings (Harrison *et al.*, 2004) and electric interconnector (Lacour *et al.*, 2004). The mechanism that produces the wrinkles is the interaction between the compressive stresses in the modified layer and the modulus mismatch between the hard layer and

the substrate. A recent study reported that uniaxial tensile strains produce periodic parallel cracks in the hard layer (Zhu *et al.*, 2005), and wrinkles are formed perpendicular to the strained direction between the cracks.

Many researchers have tried to explain the mechanism of the wrinkling using models based on the classic plate theory and energy minimization (Huck *et al.*, 2000; Bowden *et al.*, 1999; Huang *et al.*, 2005). Important parameters in the models are the thickness, the modulus and Poisson's ratio of the modified layer. Most models assume uniform material properties in the layer. However, there are experimental evidences that the properties of the layer may be distributed spatially (Bar *et al.*, 2001; Hillborg *et al.*, 2004).

In this chapter, wrinkling formed on a surface-modified PDMS will be explored. Especially, stripe wrinkles produced by compressive and tensile loads<sup>1</sup> will be examined using elasticity theory. To do this, experiments to produce wrinkles have been done at first. A model to explain the wrinkling mechanism induced by a compressive and a tensile load will be introduced for a bi-layer system. Graded modulus will be considered later using the wrinkling model and the instability model introduced in Chapter II. The wrinkling observed from the experiments will be compared with the suggested model.

## **4.2 Experimental Methods and Observations**

### **4.2.1 Producing wrinkles by a compressive load**

PDMS sheets with a thickness of 2 mm were cast using the Sylgard-184 silicon elastomer kit from Dow Corning. The base monomer and cross-linking agent were mixed in a ratio of 10:1. The sheets were cured at 60 °C for three hours, and then at 150 °C for 12

---

<sup>1</sup>Although all wrinkles are produced by a compressive stress, the terms, compressive and tensile, will be used to distinguish the experiments. Compressive load and experiment designate the experiment that strain is applied before the oxidation process. Tensile load and experiment designate the experiment that strain is applied after the oxidation process.

hours. They were then sectioned into rectangular specimens 40 mm long and 10 mm wide before being oxidized. The oxidation was performed in a plasma etcher (Plasma-Prep II, SPI Supplies Inc.) at the maximum power of 100 W, a pressure of about 40 Pa, and a constant oxygen flow rate of about 25 m<sup>3</sup>/min. The samples were exposed to the oxygen plasma under these conditions for various periods ; 30 sec, 4, 20, 40, and 60 min. This oxidation process resulted in a thin, stiff surface-modified layer.

A well-documented technique that appears to induce a compressive stress within the surface-modified layer is to oxidize the PDMS while holding it under a fixed tensile strain (Volynskii *et al.*, 2000; Watanabe, 2005). When the constraint applying the strain is released after oxidation, surface wrinkling is observed perpendicular to the direction of the original applied strain. This wrinkling indicates that relaxation of the applied strain induces a compressive stress within the surface layer. In the present study, a tensile strain of  $4 \pm 1 \%$  was applied manually to the specimen before oxidation, and then both ends of the specimen were clamped to a glass plate using metal clips. The surface of the glass plate was covered by paper tape to prevent adhesion. The magnitude of the strain was estimated by using digital calipers to ensure that two lines marked at a distance of 20 mm apart on the surface of the specimen were moved apart by 0.8 mm. The samples were oxidized while clamped to the glass plate.

After oxidation, the applied strain was released by removing the clamps. A 10 mm by 10 mm section was cut from the center of the specimen and examined in an atomic force microscope in tapping mode<sup>2</sup>. Figure 4.1 shows a typical profile of the surface of the specimen after oxidation for 40 minutes and relaxation of the applied tensile strain. While this image, with its very regular wrinkling pattern is fairly typical for a specimen that has been subjected to a prolonged period of oxidation, some of the specimens oxidized for

---

<sup>2</sup>Nanoscope III AFM, using a silicon tip with a nominal stiffness of 42 N/m

shorter period showed more irregularity in the amplitudes of the wrinkles. In all cases, the wrinkles formed perpendicular to the direction of the applied tension. Images such as these were used to measure how the wavelength varied with oxidation time (Figure 4.2).

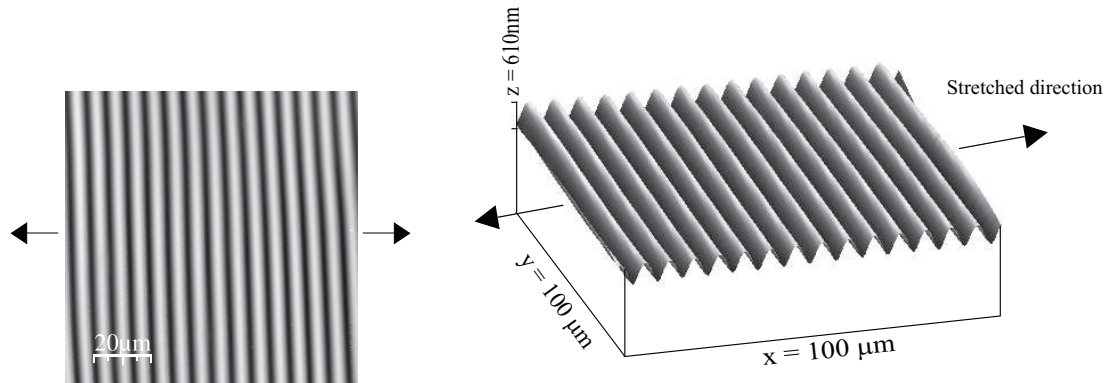


Figure 4.1: Surface buckling after relaxation of a 4 % tensile strain imposed during a 40-minute oxidation. The left-hand image is a 2-D projection of the image shown on the right.

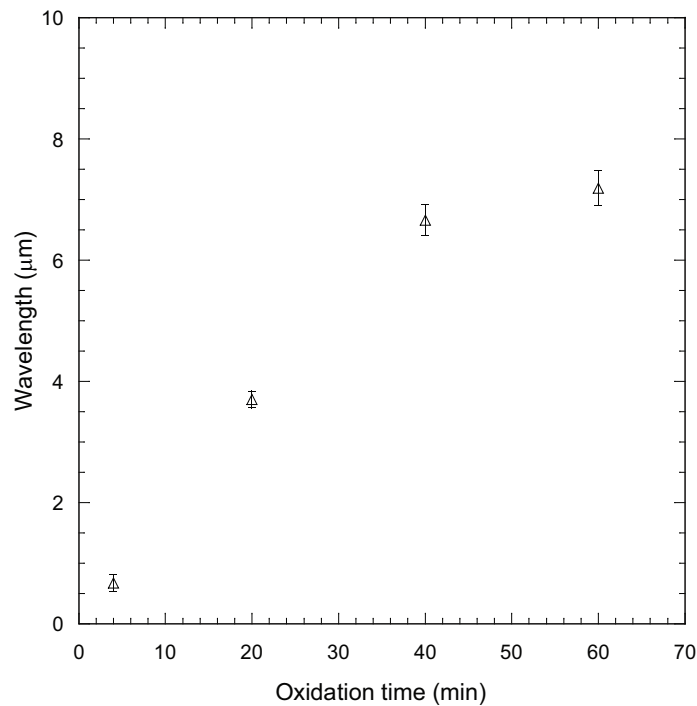


Figure 4.2: Distribution of the wavelengths produced by compressive loading produced by pre-stretching. At 30-second oxidation, wrinkles were not found.

No surface wrinkling was observed when the oxidation time was only 30 seconds. The wavelength increased monotonically from about 1 micron for an oxidation time of 4 minutes to about 7 microns for an oxidation of 60 minutes. This increase is believed to be associated with the increase in the thickness of the surface-modified layer with oxidation time.

#### 4.2.2 Producing wrinkles by tensile loading

An alternative way to produce surface wrinkles in this system is to oxidize the PDMS in a relaxed state, and then to apply a uniaxial tensile strain. As a consequence of this applied tensile strain, periodic cracks form in the surface-modified layer (Zhu *et al.*, 2005), and then, upon further loading, wrinkles form between and perpendicular to the cracks (Mills *et al.*, 2007).conducted in which the PDMS specimens were oxidized in a relaxed state. After oxidation, a tensile strain of 10 % was applied by means of a mechanical stretcher. Figure 4.3 shows overall procedure to produce wrinkling by the two loading methods.

Owing to the limitations of the available atomic force microscope, it was impossible to measure the surface topology directly in a stretched state. Therefore, a replica was taken of the cracked and wrinkled surface while the tensile strain was applied. The surface was treated<sup>3</sup> to prevent adhesion to the replica. PDMS, with a 10:1 ratio of monomer to hardener, was poured onto the surface and cured for 2 hours at 60°C oven while the sample was still under an applied tension. After curing, the replica was stripped from the surface, and a section was cut from the middle for examination in the AFM (Figure 4.4).

A typical example of the data from an AFM scan of a replica is shown in Figure 4.5.

---

<sup>3</sup>A mixture of (tridecafluoro-1,1,2,2-tetrahydrooctyl)-1- trichlorosilan and mineral oil was mixed on a glass plate in a 1:1 ratio. The glass plate and the stretched specimen were placed in a vacuum chamber for seven minutes to allow the vapor to condense onto the cracked surface.

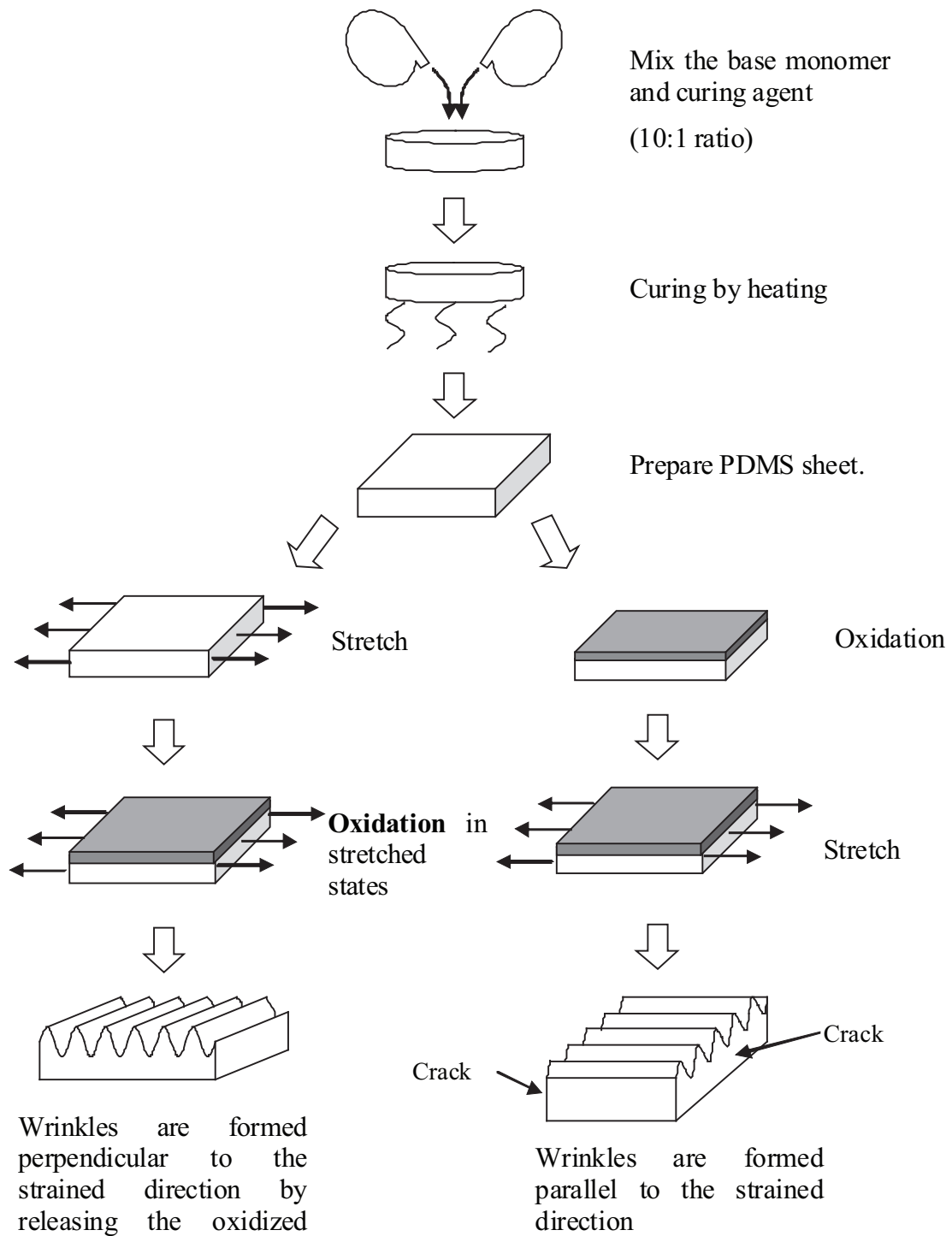


Figure 4.3: Schematic for the process to produce wrinkles on an oxidized surface of PDMS using two loading methods

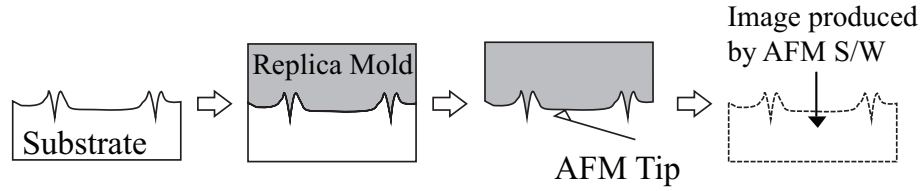


Figure 4.4: Measurement of the surface topology of the oxidized PDMS subjected to tensile load using replica mold

The features that can be identified in this figure are the periodic cracks perpendicular to the applied tensile strain, and the surface wrinkles between these cracks that are aligned in the direction of the applied strain. Measured data for how the average wavelength of the wrinkles varies with oxidation time are included in Figure 4.6. As seen in the figure, there is a significant difference in the wavelengths obtained from the experiments in which wrinkles were generated by relaxing a tensile strain, and those in which the wrinkles were generated between cracks. It is clear that the wavelengths generated in the former experiments were systematically smaller than those obtained in the latter experiments. In order to confirm that this difference was caused by the different procedures, every effort was made to ensure that all other features of the experiments were identical. In particular, the specimens for each pair of tests at the same oxidation times were prepared from the same batch of material and were oxidized together.

Furthermore, an additional set of experiments were performed in which a replica was taken from a set of samples subjected to relaxed tension to verify that the process of producing a replica did not affect the results. Single specimen was used to produce wrinkles for both tensile and compressive loading. Tensile strain of  $7 \pm 1\%$  was applied to the specimen before 10-minute oxidation. After oxidation, the specimen was released and first replica was made. The same specimen was stretched by 14% using a mechanical stretcher, and the second replica was made from the strained specimen. Same surface treatment technique was used for both replicas. In this experiments, wrinkles produced by

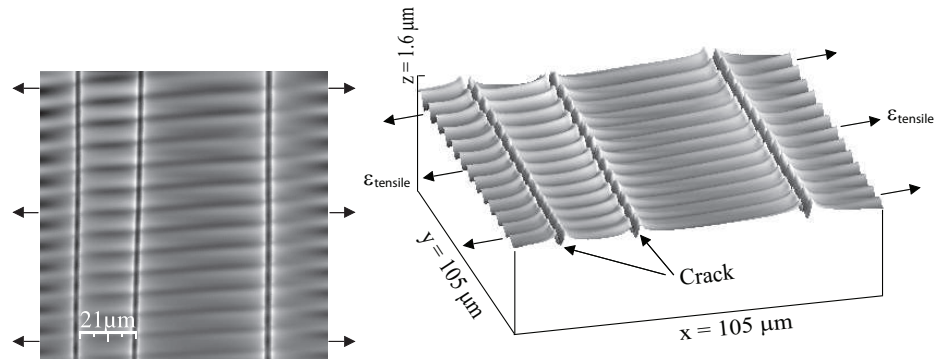


Figure 4.5: Wrinkles produced by a 10 % tensile strain applied after a 40-minute oxidation. The left-hand image is a 2-D presentation of the data shown in the right. Both images are inverted from the raw data obtained from the AFM from the replica, so the cracks appear as cracks not hillocks.

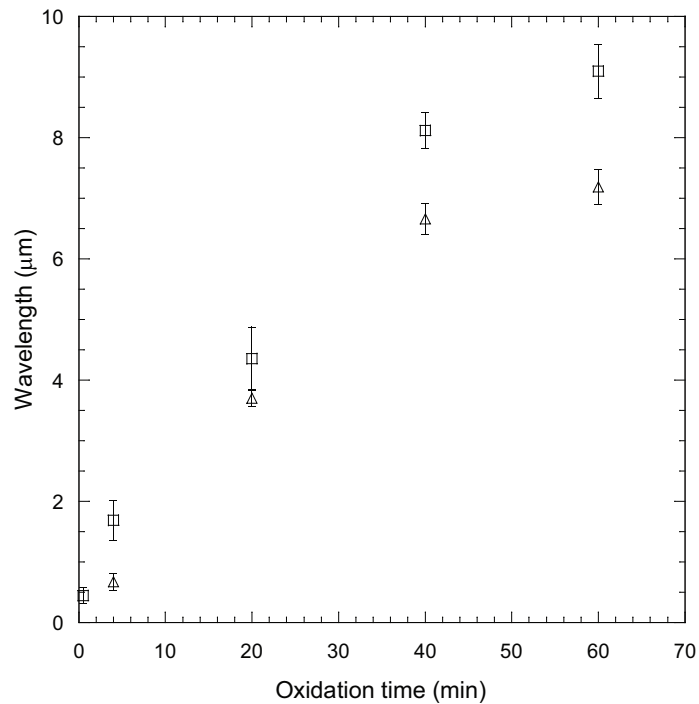


Figure 4.6: Wavelengths of wrinkles produced by tensile loading (□). Wavelengths produced by compressive loading (△) are added for comparison

a tensile load was always longer than these produced by a compressive load. Therefore, the process of producing a replica did not affect the results. In the next section, possible causes for this difference are addressed.

### 4.3 Wrinkling in a surface-modified layer

A statistically meaningful discrepancy was observed in wavelengths through a series of experiments conducted using two loading methods. Every effort has been made to assure that the experiment conditions were controlled with care except two differences loading methods and cracks in tensile experiment may be the causes of the discrepancy.

If Poisson's ratio was independent of the depth, the lateral strains in the tension experiment would be compatible. In other words, the only possible explanation would be a variation of Poisson's ratio with depth before the cracks form. If Poisson's ratio is same in the system, lateral strains could not develop stresses in the plane perpendicular to the tensile strain. This means that the entire structure simply shrinks, and only a volume change is physical phenomenon that can be seen. Therefore, constant Poisson's ratio is unable to produce wrinkles. The effect of Poisson's ratio will be examined using a simple model for a bi-layer system.

#### 4.3.1 Effect of Poisson's ratio mismatch

Suppose a strain  $e_{11} = \epsilon_1$  is applied in the  $x_1$ -direction uniformly and the  $x_2$ - surface is unrestrained (Figure 4.7), so that  $e_{22}$  adopts whatever value is necessary for the total force to be zero;  $\sigma_{22}^f H_f + \sigma_{22}^s H_s = 0$ . Because the substrate is much thicker than the film layer ( $H_s \gg H_f$ ), the zero force condition reduces to  $\sigma_{22}^s = 0$ . Also, stress in the  $z$ -direction ( $\sigma_{33}$ ) is zero in the structure. Based on this argument, the stress distribution can be derived

using Hooke's law.

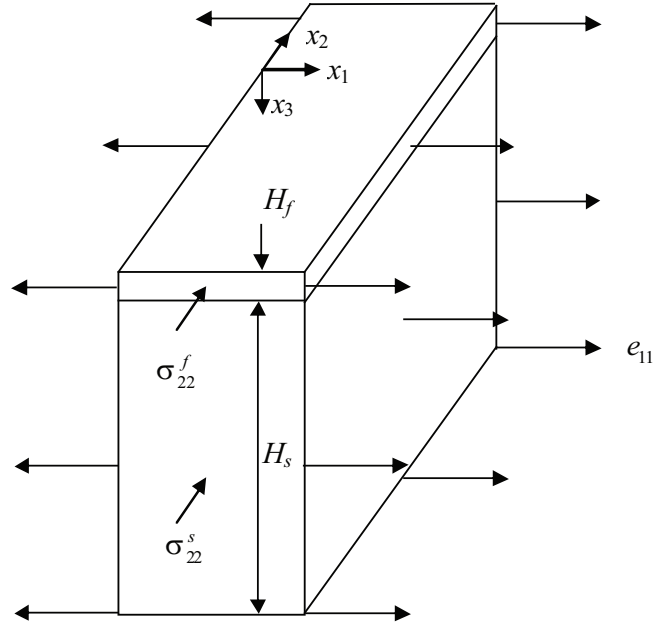


Figure 4.7: Layered structure subjected to a lateral load. The  $f$  and  $s$  in superscripts and subscripts mean film and substrate, respectively.  $H_f$  and  $H_s$  are thickness of the film layer and substrate, respectively.

In Figure 4.7, Hooke's law for the substrate gives,

$$\epsilon_1 = e_{11}^s = \frac{\sigma_{11}^s}{E_s} - \frac{\nu_s \sigma_{22}^s}{E_s} = \frac{\sigma_{11}^s}{E_s} \quad (4.1)$$

and hence

$$\sigma_{11}^s = E_s \epsilon_1 \quad (4.2)$$

Also, the strain in the  $x_2$  direction is

$$e_{22} = \frac{\sigma_{22}^s}{E_s} - \frac{\nu_s \sigma_{11}^s}{E_s} = -\nu_s \epsilon_1 \quad (4.3)$$

The same strain ( $e_{22}$ ) must be applied in the film layer and hence

$$e_{22} = \frac{\sigma_{22}^f}{E_f} - \frac{\nu_f \sigma_{11}^f}{E_f} = -\nu_s \epsilon_1 \quad (4.4)$$

and

$$\epsilon_1 = \frac{\sigma_{11}^f}{E_f} - \frac{\nu_f \sigma_{22}^f}{E_f} \quad (4.5)$$

The stresses in the film layer can be determined from equation (4.4) and (4.5).

$$\begin{aligned} \sigma_{11}^f &= \frac{E_f \epsilon_1 (1 - \nu_f \nu_s)}{1 - \nu_f^2} \\ \sigma_{22}^f &= \frac{E_f \epsilon_1 (\nu_f - \nu_s)}{1 - \nu_f^2} \end{aligned} \quad (4.6)$$

Suppose that the system buckles in compression when  $\epsilon_1 = -\epsilon_c$ , implying that

$$\sigma_{11}^f \equiv \sigma_c = -\frac{E_f \epsilon_c (1 - \nu_f \nu_s)}{1 - \nu_f^2} \quad (4.7)$$

The wrinkling would occur in tension only if

$$\sigma_{22}^f = \sigma_c \quad (4.8)$$

This requires that

$$\frac{\epsilon_1}{\epsilon_c} = \frac{1 - \nu_f \nu_s}{\nu_s - \nu_f} \quad (4.9)$$

This defines a tensile strain only if  $\nu_s > \nu_f$ , and the minimum practical ratio of  $\epsilon_1/\epsilon_c$  occurs when  $\nu_f = 0.0$ ,  $\nu_s = 0.5$  and is

$$\frac{\epsilon_1}{\epsilon_c} = 2.0$$

For more realistic values of  $\nu_f = 0.25$  and  $0.3$ , the strain ratios are  $3.5$ ,  $4.25$ , respectively.

In the experiments, the minimum and maximum applied tensile strains were  $6\%$  and  $20\%$ ,

respectively, and the compressive strains were 4 % and 7%. Though the tensile and compressive strains are not real critical values, a rough estimation can be made using these values. From the applied tensile and compressive strains, the range of the strain ratio ( $\epsilon_1/\epsilon_c$ ) can be obtained; 0.85 ~ 5.0. The strain ratio less than equal to 2.0 leads to the conclusion that Poisson's ratio of the film layer is negative or zero. Even though the ratio seems to be in the rather practical range (*i.e.* the ratio is larger than 2.0), it doesn't show why the wavelengths are different. Thus, the stress distribution in the entire structure needs to be examined for the estimation of the critical strains and wavelengths according to the loading method.

#### 4.3.2 Stresses produced by compressive and tensile loading

In the preceding section, it was assumed that the wrinkling depends only on the state of compressive stress in the film layer. However, this is not strictly correct. It may depend not only on the compressive stresses in the direction perpendicular to the resulting waviness, but the stresses in the substrate may make a contribution to the energy balance and hence both to the critical strain and the wavelength.

The stresses derived in the preceding section can be used as compressive stresses for the compressive and tensile loading. In the direct compression case, the second equation in Eq. (4.6) can be the stress in the film layer, and Eq. (4.2) can be the stress in the substrate.

$$\sigma_{11}^f = -\frac{E_f \epsilon_c (1 - \nu_f \nu_s)}{1 - \nu_f^2}, \quad \sigma_{11}^s = -E_s \epsilon_c \quad (4.10)$$

where,  $\epsilon_c (> 0)$  is the critical compressive strain, the superscripts  $f$  and  $s$  represent the film layer and substrate, respectively. In the tensile loading case, the second equation in Eq. (4.6) can be a stress in the film layer, and the stress in the substrate is zero according

to the zero force condition used in the preceding section.

$$\sigma_{22}^f = -\frac{E_f \varepsilon_t (\nu_s - \nu_f)}{1 - \nu_f^2}, \quad \sigma_{22}^s = 0 \quad (4.11)$$

where,  $\varepsilon_t$  is the critical tensile strain, and the superscripts  $f$  and  $s$  again represent the film and the substrate, respectively. It needs to be investigated whether the difference in the substrate stress ( $\sigma^s$ ) between these two cases causes any measurable difference in the critical strain and wavelength for practical values.

To simulate the two loading methods, Eqs. (4.10) and (4.11) are used in the finite-element code developed in Chapter II. Convergence tests are performed using different mesh sizes. To reduce numerical errors that may be caused by the abrupt change of mesh sizes, the substrate is divided into two layers, and hence the mesh sizes are changed gradually from the film layer to a position in deep substrate. With over 50 elements in film layer and 100 elements in substrates, the critical strains and wavenumbers converge to a value with less than 0.1% error.

Figure 4.8 shows the distribution of the ratios of critical strains and wavelengths. The difference of wavelengths (*i.e.* dimensionless wavenumber  $\omega H$ ) is shown in mostly low modulus ratio ( $E_f/E_s < \sim 100$ ). This difference seems to be adequate because the difference of stress field is in the substrate. Therefore, the wavelength difference is in right direction but probably not big enough to explain the discrepancy of the experimental. The ratios of critical strains seem to close to the theoretical estimation in high modulus ratios but not in low modulus ratios. This may be caused by the numerical calculation or discretization for the FE calculation. While Poisson's ratio mismatch and the zero force condition seem to be causes of the wavelength discrepancy, the wavelengths seem to be not much sensitive to the change of Poisson's ratio.

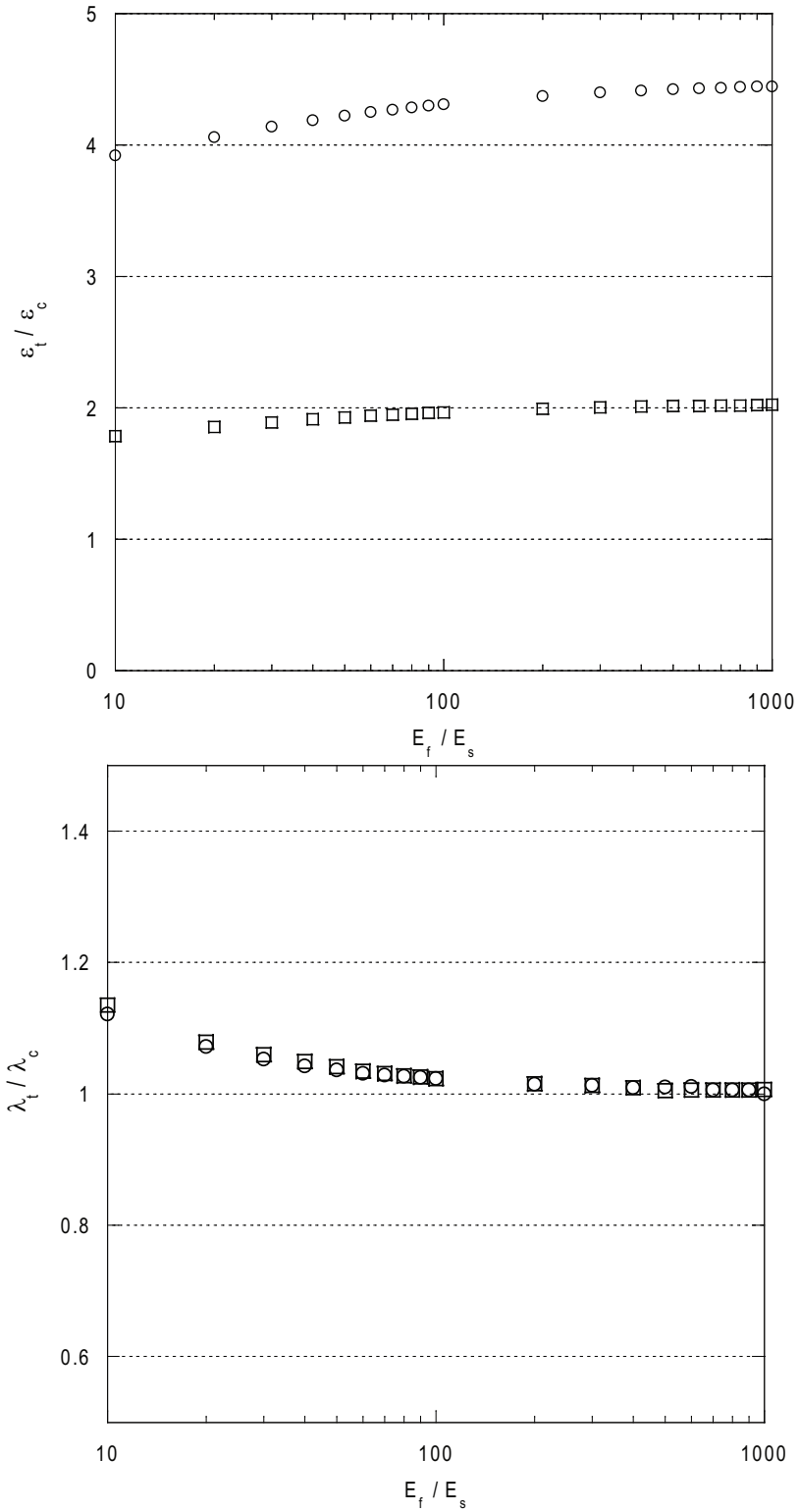


Figure 4.8: The ratios of critical strains and wavelengths with respect to Poisson's ratios; ( $\square$ )  $\nu_f = 0.0$ , ( $\circ$ )  $\nu_f = 0.3$ .  $\nu_s = 0.49$  is used in the numerical calculations.  $H_s/H_f = 100.0$ .

## 4.4 Effect of cracks

In the preceding section, we found that Poisson's ratio mismatch does not give significant effect to the difference of wavelengths for both tensile and compressive loadings. Thus, another physical difference in the experiments—cracks—needs to be examined. The effect of cracks on the formation of wrinkles is not clearly understood. While it may or may not affect the formation of wrinkles, the experiments show that wrinkling doesn't occur until the cracks form, suggesting that it is influenced by the resulting redistribution of stress during crack opening. Therefore we need to make a model to consider the stress redistribution. Suppose part of the surface-modified PDMS (Figure 4.9). We assume the vertical planes remain straight before and after crack opening and while strains are applied.

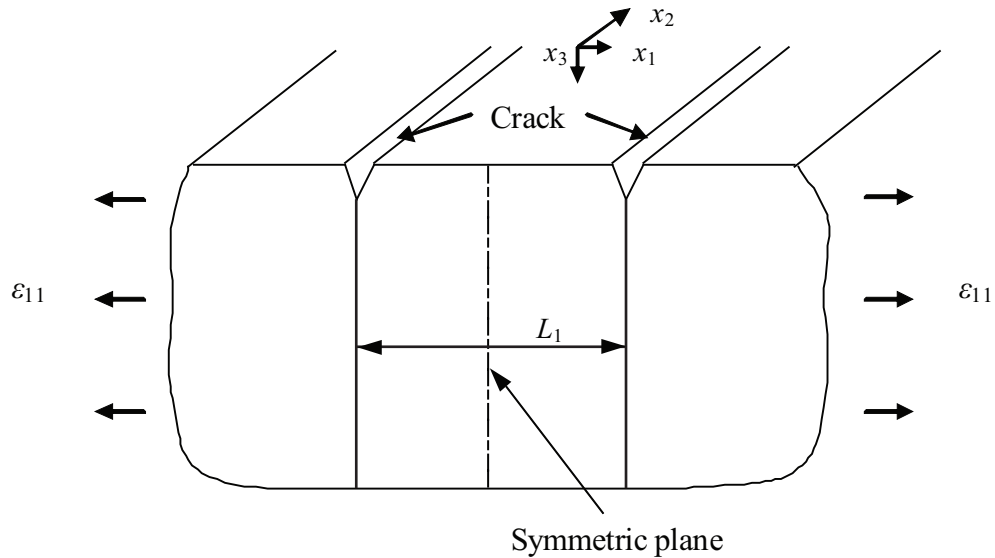


Figure 4.9: Schematic for crack opening and assumption of vertical planes

To estimate the relation between the crack opening and the stress relaxation, we focused on the stress variation between cracks. If the stress decays rapidly and the crack spacing is far enough, the region around symmetric plane will be plane strain status. There-

fore, the wrinkles may not be formed in the middle of the two cracks (Figure 4.10a). If the decay rate is slow enough, stresses on the surface can be considered as zero (Figure 4.10b). Intermediate decay rate also can occur, and it may produce waves between cracks. This case will not be considered in this section (Figure 4.10c).

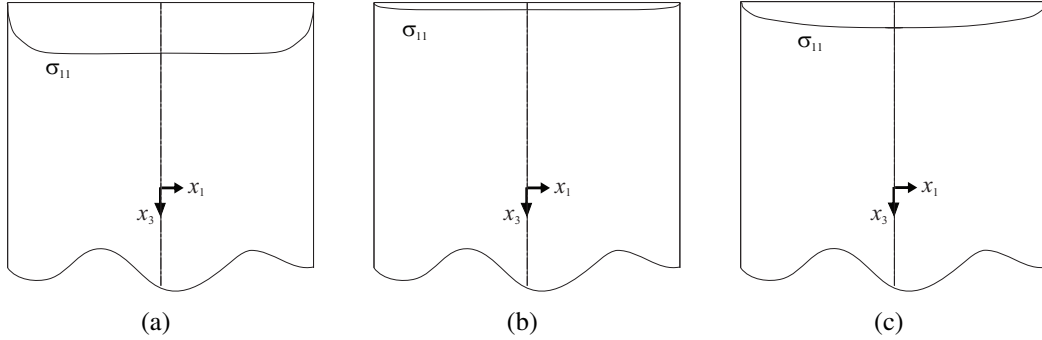


Figure 4.10: Possible types of stress relaxation between cracks

#### 4.4.1 Stress relaxation between cracks

To check the variation of stress field between cracks, finite element simulations were performed using ABAQUS. Figure 4.11 shows the geometry and boundary conditions used in the simulation that modeled the half of the length between two cracks. Unit traction is applied on the film layer. The decay length is defined as the length that the stress decays, 50% of the input (Figure 4.12).

Through a series of simulations, the relation between the decay length and the modulus ratio is obtained. The problem is whether the decay length is shorter than dimensionless crack space ( $L_1/H_f$ ).

$$\frac{d}{H_f} \sim 1.75 \frac{E_f}{E_s} \quad (4.12)$$

To compare the decay length (4.12) to experiment results, the thickness of the oxidized

layer was estimated using Eq. (4.13) suggested by Chen and Hutchinson (2004).

$$\frac{\lambda}{2\pi H_f} = \left(\frac{\bar{E}}{3\bar{E}_s}\right)^{1/3}, \quad \varepsilon^c = \frac{1}{4} \left(\frac{3\bar{E}_s}{\bar{E}}\right)^{2/3} \quad (4.13)$$

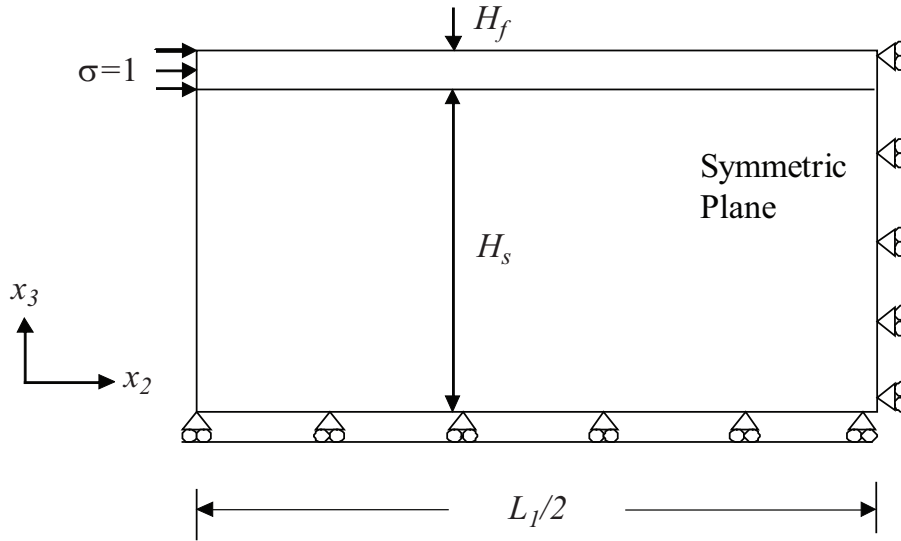


Figure 4.11: Geometry to calculate the decay length

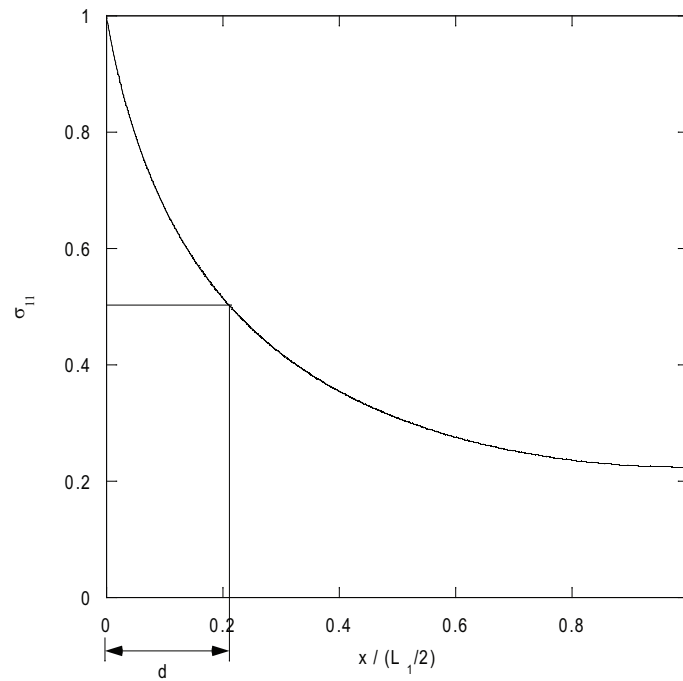


Figure 4.12: Graphic model of the decay length ( $d$ ). It is defined by a length that the magnitude of stress in the film layer becomes half of the input value.

Because the critical strains included in Eq. (4.13) are unable to be determined from experiments directly, arbitrary values were assumed, which are smaller than the lowest applied strain (4%). For an assumed critical strain, the modulus ratio of the film and substrate was calculated, and then the film thicknesses are estimated from the measured wave lengths and the estimated modulus ratios.

Figure 4.13 shows the distribution of the dimensionless decay lengths and crack spacings at various oxidation times. The  $x$ -axis is the assumed critical strain and the  $y$ -axis is the dimensionless lengths ( $d/H_f$  or  $(L_1/2)/H_f$ ). To check the consistency, several crack spacings were chosen at an oxidation time (Table 4.1). The symbols on a same vertical line show the difference between the decay length and the crack space. As seen in the figure, the decay length is always longer than the crack space for all cracks produced under various oxidation times. This means that the decay rate of the stress is slow enough so that the stress relaxation doesn't produce any significant effect on the amplitude of the wrinkles between cracks. This estimation also can be supported by the measurement of the amplitudes of wrinkles between two cracks. Figure 4.14 shows the contour map of amplitudes between selected cracks measured from 60-minute oxidized specimen. As seen in the figure, the amplitude of a wrinkle doesn't change significantly between two cracks. Thus, a simple model derived in the preceding section can be used to set up the stress distribution.

Table 4.1: Average crack spacings used in the comparison

Crack Spacing( $\mu\text{m}$ ) Oxidation Time(min)	1	2	3
4	5.39	10.86	-
20	6.55	13.28	13.5
40	11.37	29.13	48.4
60	12.53	20.84	32.84

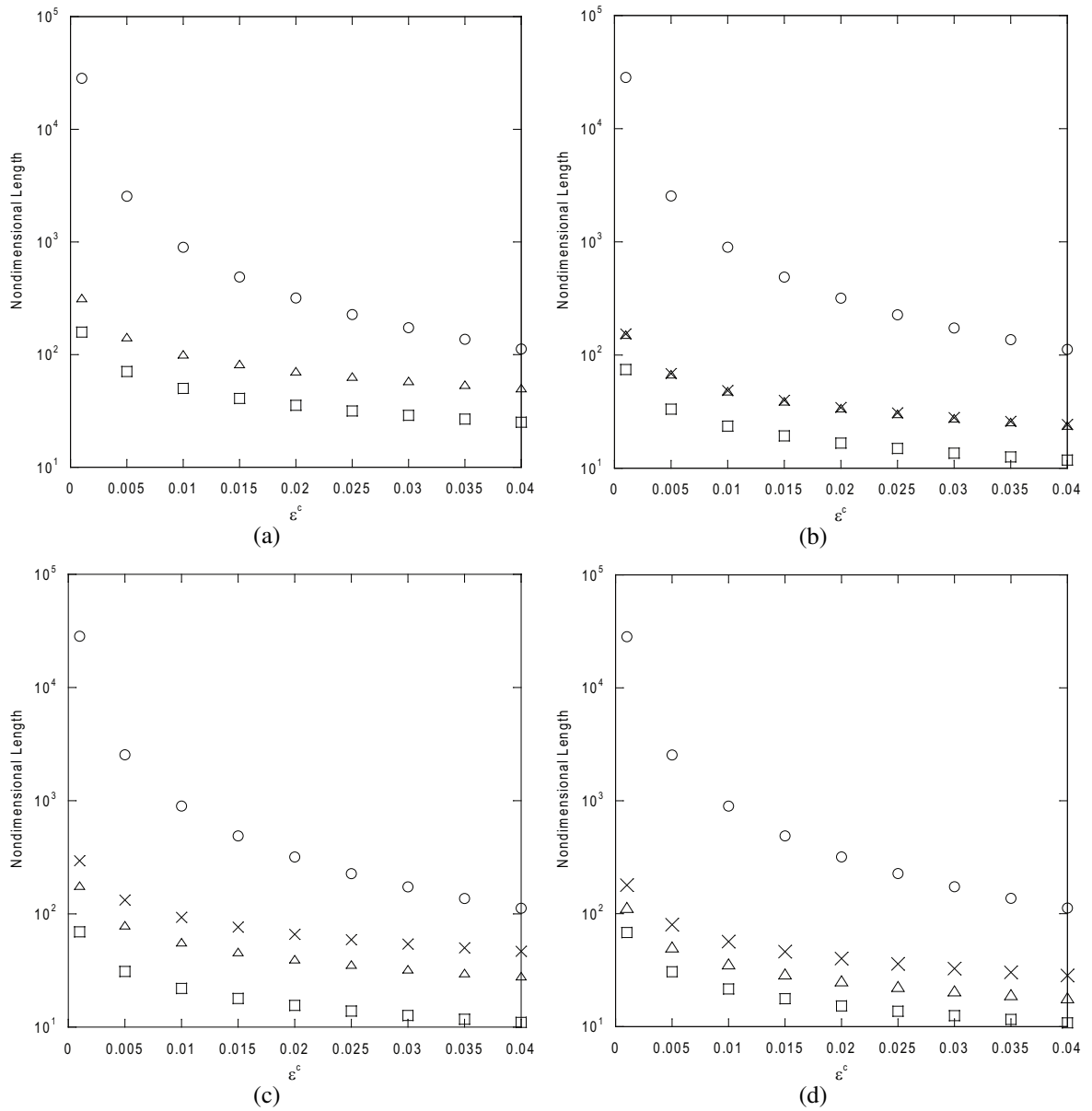


Figure 4.13: Comparison between nondimensional decay lengths and crack spacings at different oxidation time. (a) 4, (b) 20, (c) 40, (d) 60 minutes. ( $\circ$ ) nondimensional decay lengths calculated by FE simulations, ( $\square$ ,  $\triangle$ ,  $\times$ ) nondimensional crack spacings estimated from the experiment results. Critical strains ( $x$ -axis) are assumed to estimate the ratio of the crack spacing to the film thickness.

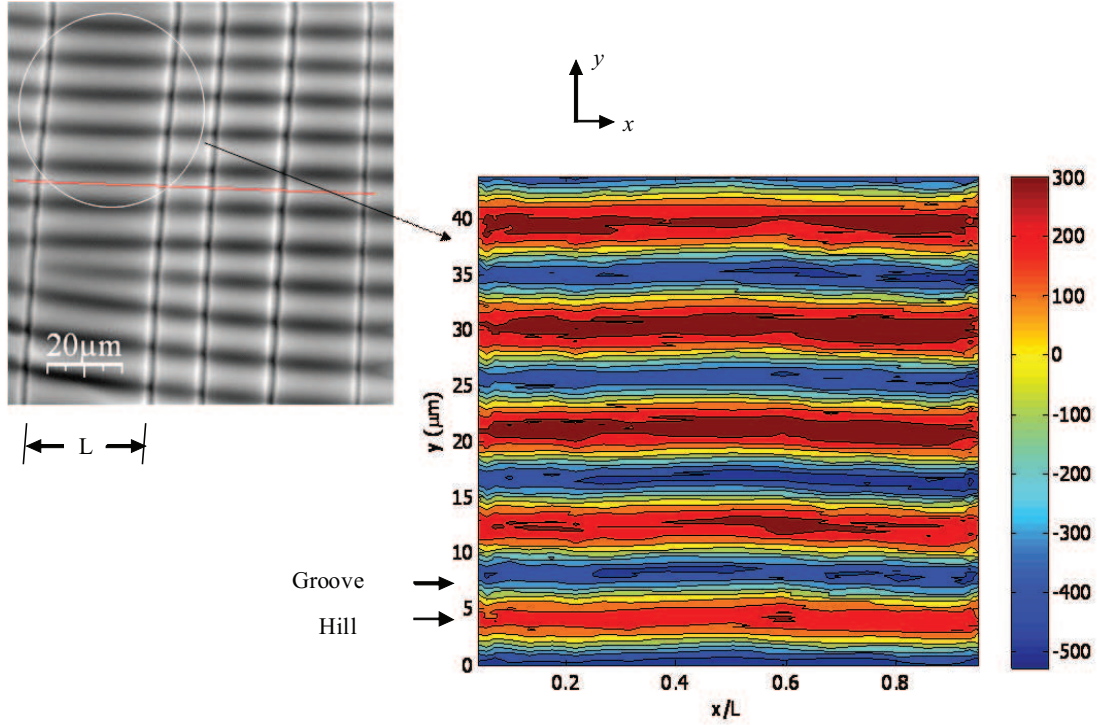


Figure 4.14: AFM image of 60-minute oxidized PDMS (left) and contour map of the amplitude between selected cracks (right). Horizontal line in left image is same with the  $x$ -axis in right image. White parts of the left image are the top of the wrinkles and dark parts are the bottoms.

#### 4.4.2 Stress field induced by crack opening

Before crack opening stresses developed in  $x_1$  direction, there are stresses in the film only in  $x_2$  direction, only if Poisson's ratios are different. The effect is localized to the surface, and by assuming the crack depth is also small compared with the substrate depth, the forced induced in  $x_2$  direction near the surface will have a negligible effect on  $e_{22}$  (same reason in the preceding section). If also the crack spacing is small compared with the decay length as we argued, then the effect of the relaxation is to reduce the tensile stress  $\sigma_{11}$  in the film to zero, whilst holding  $e_{22}$  constant. Assume plane strain in the  $x_2$  direction. This will induce a compressive stress,  $\sigma_{22} = -\nu\sigma_{11}$ . There will also be some compressive stress  $\sigma_{22}$  in the substrate near the interface between the film and the substrate

for the same reason, but it may not have much effect, because it is found that even having a compressive stress throughout the substrate didn't change the buckling much relative to having compressive stress only in the film (Figure 4.8). Therefore, the stress relaxation can be simulated by pressurizing the film layer with the stress ( $\sigma_{11}$ ) derived in preceding section, which has same magnitude but subject on opposite direction (Figure 4.15b). The crack is assumed to be not propagated along depth (*i.e.* the crack opening occurs in the film layer only).

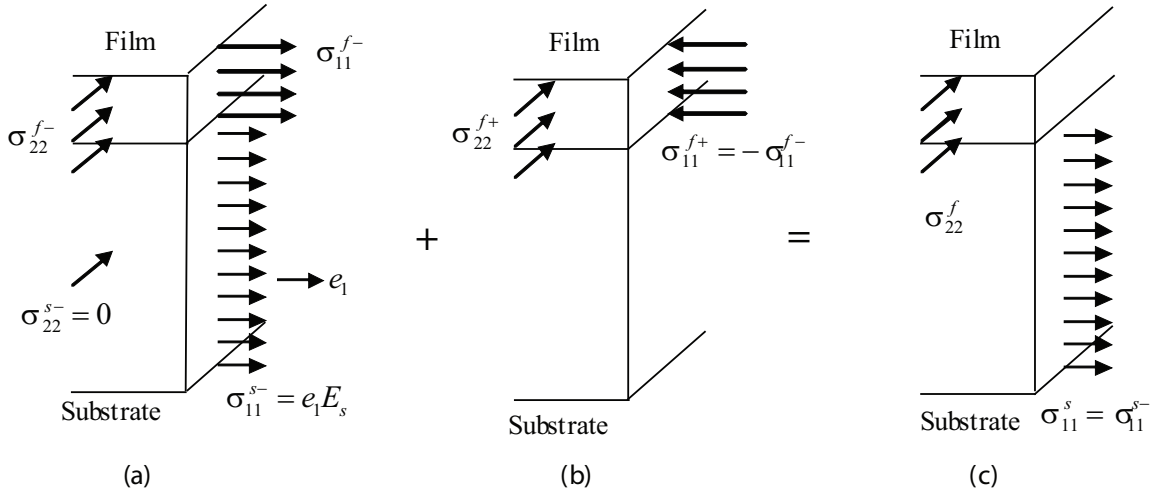


Figure 4.15: Modeling the stress relaxation in the film layer by crack opening. The minus and plus sign in superscripts are used to denote the states before and after crack opening, respectively.

At the time just before a crack opens, the stress distribution in both the film layer and substrate is same with Eq. (4.6) (Figure 4.15a). To simulate the stress relaxation in the film layer,  $\sigma_{11}$  is applied on the film layer in the negative  $x_1$ -direction (Figure 4.15b). At the time of crack opening, plane strain in the  $x_2$ -direction is supposed in the film layer.

$$\varepsilon_{22}^{f+} = \frac{\sigma_{22}^{f+}}{E_f} - \frac{\nu_f \sigma_{11}^{f+}}{E_f} = 0 \quad (4.14)$$

This gives a new stress induced by the crack opening.

$$\sigma_{22}^{f+} = -\nu_f \sigma_{11}^{f-} = -\frac{E_f e_1 (1 - \nu_f \nu_s) \nu_f}{1 - \nu_f^2} \quad (4.15)$$

Therefore, the compressive stress ( $\sigma_{22}^f$ ) in the film layer can be obtained by superposition of two stress components in equations (4.6) and (4.15)

$$\sigma_{22}^f = \sigma_{22}^{f-} + \sigma_{22}^{f+} = -E_f e_1 \nu_s \quad (4.16)$$

The compressive stress in the film layer is dependent on Poisson's ratio of the substrate only. Eq. (4.16) is used as the stress distribution in preceding section for the simulation. The same level of error with the previous sections has been achieved by doing another convergence tests with this stress field.

The ratios of critical strains and wavenumbers are shown in Figure 4.16, which are calculated by the tensile load Eq. (4.16) and the compressive load Eq. (4.10). Here, we can see how the crack affects on the wavelengths. The ratios of the critical strains decrease less than 2.0 even Poisson's ratio of the film layer is larger than zero. For same Poisson's ratios ( $\nu_f = 0.3$  and  $\nu_s = 0.49$ ), the wavelength ratios in the preceding section show the range of  $3.9 \sim 4.5$ . With same Poisson's ratio for both modified layer and substrate, to obtain same length of wrinkles, the tensile strain needs to be larger than the compressive strain about  $4 \sim 4.5$  times if cracks are not formed. With crack opening, tensile strains that are larger than  $1.7 \sim 1.9$  of the compressive strain are enough to produce the same length of wrinkles. Though the ratios of wavelengths are not much different for both cases, the change in the strain ratios may be a good evidence of the role of cracks.

As a critical case, homogeneous case ( $\nu_f = \nu_s = 0.49$ ) has been chosen to examine the effect of Poisson's ratio. This case causes maximum 10% in critical strain at  $E_f/E_s = 10$ . Wavelength changes are less than 3% along the entire range of modulus ratios.

### 4.4.3 Effect of graded modulus

In the preceding section, we found that the possible effect of the cracks on the formation of the wrinkles in the surface-modified layer of PDMS. In Chapter III, we also found that the error function can be a good model of graded modulus in the modified layer. The error function is used by matching the length scale  $H$  to the thickness of a modified layer  $H_f$ . Therefore, non-uniform compressive stresses subject in the region as deep as  $H$ . Poisson's ratio  $\nu = 0.49$  is assumed for the entire system, and convergence test also has been done.

Figure 4.17 shows the ratios of critical strains and wavelengths. Here another difference can be observed from the preceding section. Both the ratios of critical strains and wavelengths are higher than these shown in Figure 4.16. The graded modulus may cause the higher strain ratios, however the ratios of critical strains are still less than the analytical estimation (*i.e.* = 2.0). The ratios of wavelengths are higher than the case of bi-layer with crack opening along the entire modulus ratios and especially at low modulus ratios ( $E_0/E_s < \sim 100$ ). Therefore, both crack and graded modulus may affect to the wavelength discrepancy.

## 4.5 Conclusions

We did two types of experiments to produce wrinkling in a modified-surface of PDMS. For each experiment wavelengths were observed and a discrepancy in the wavelengths was observed between the loading methods. To reveal this discrepancy, analytical models to describe the stress field in the system have been developed with assumptions to deal the effect of Poisson's ratio mismatch, crack opening, and graded modulus.

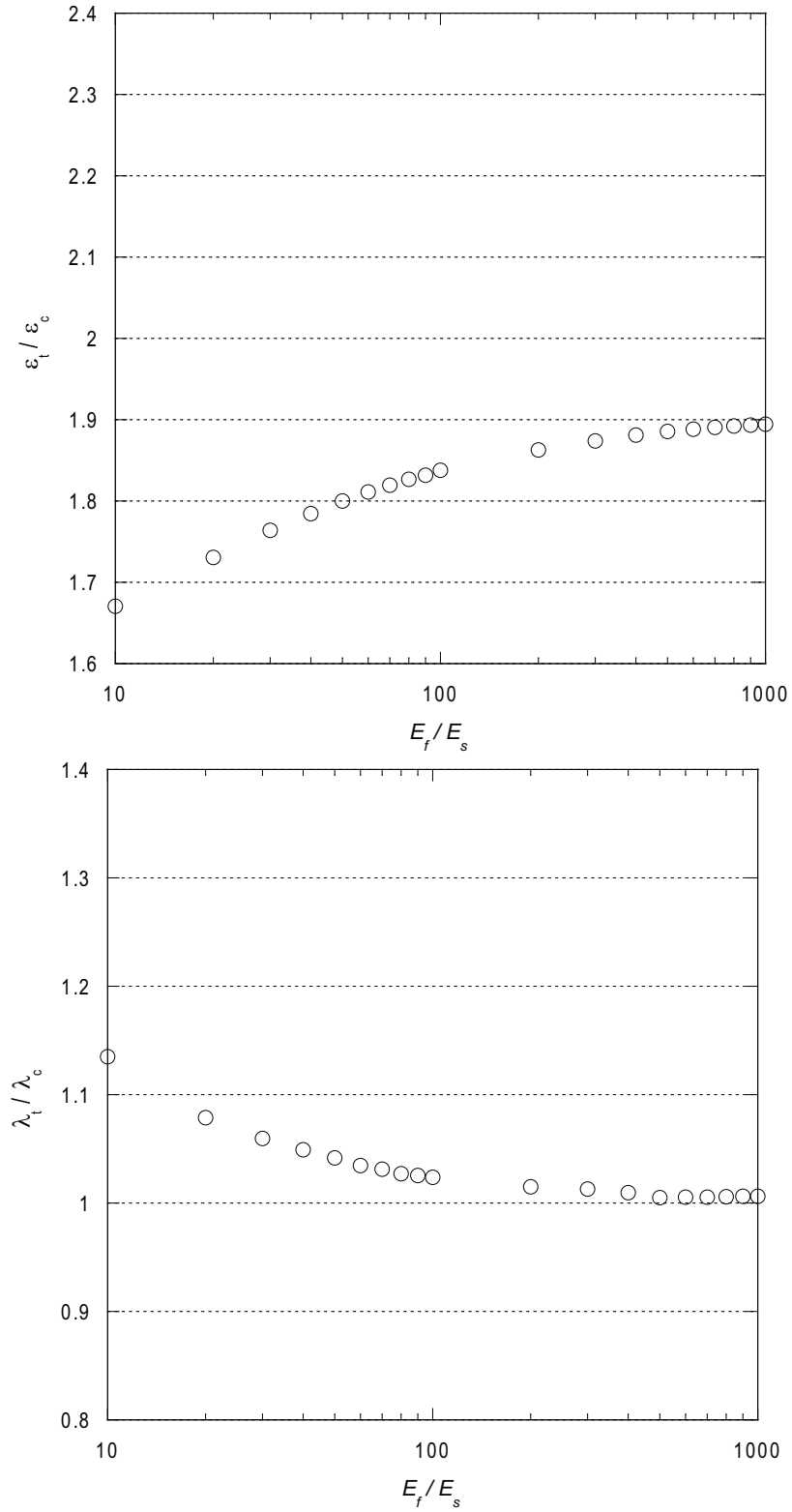


Figure 4.16: Effect of crack opening on the ratios of critical strains and wavelengths;  $\nu_f = 0.3, \nu_s = 0.49, H_s/H_f = 100.0$ .  $E_f$  and  $E_s$  are the modulus of the surface-modified layer and substrate, respectively.

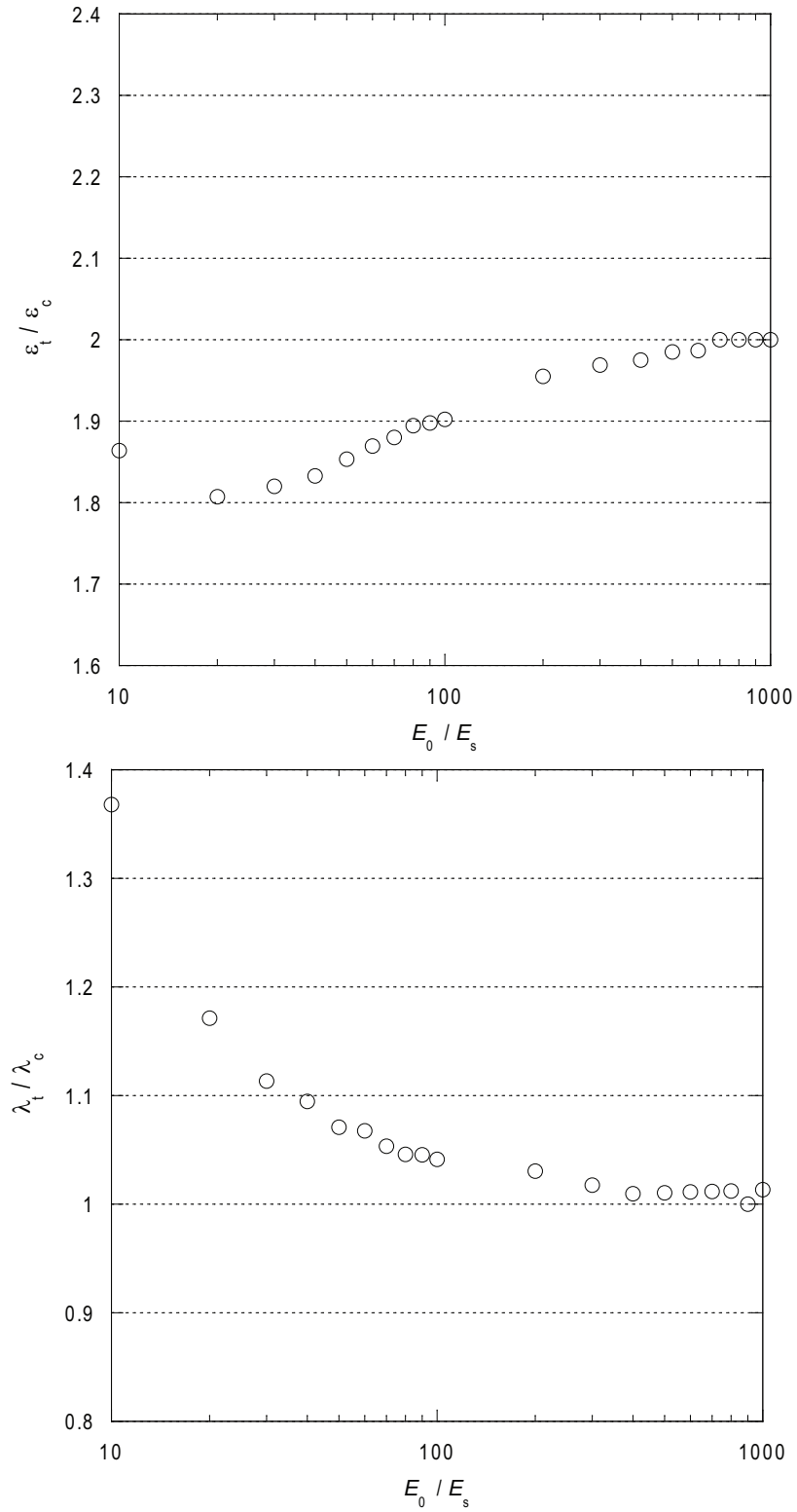


Figure 4.17: Effect of graded modulus on the ratios of critical strains and wavelengths.  $\nu = 0.49$  for entire system.  $E_0$  is the modulus at the surface of a modified layer.  $E_s$  is the modulus of substrate.

Though the wavelengths between structures with and without cracks are not much different, we could find a cause of the discrepancy in the ratios of critical strains. The ratios of critical strains with cracks were less than the ratios without cracks. When we have considered the error function as a modulus distribution, the strain ratios decreased, and the wavelength ratios increased compared to the ratios of a bi-layer system with cracks. Though a quantitative estimation is hard to obtain from the suggested models, the discrepancy in the experiments can be explained qualitatively, and the models suggested in this section could be a useful tool for a research.

## CHAPTER V

# CONCLUSIONS AND FUTURE WORK

### 5.1 Conclusions

In this study, theoretical approaches are introduced to investigate the characteristics of a thin hard layer on a soft substrate, and they are used to explain experimental results obtained from the observation of a plasma-oxidized PDMS. The methods and models introduced in this research can be used as a framework for the characterization of a hard thin layer on a soft substrate.

A general theory is suggested to determine the critical conditions (critical strain and corresponding wavenumber) that cause the surface instability on an elastic half space or a thick substrate loaded in compression. The suggested model is verified by comparing with a previous research for a bi-layer structure consisting two layers with homogeneous properties. The effect of graded material properties exhibit dependence on modulus ratios similar to those observed from a bi-layer system. Using suggested model, we demonstrate that non-mechanical perturbation such as thermoelastic loading with transient surface heating can generate wrinkling on a half space and we give results for the critical surface temperature at which a homogeneous half space will develop wrinkling.

Indentation theories are explored to reveal the linear force-indentation depth relationships observed in the nonindentation experiments. The plate theory and a modified plate

theory are examined by the finite-element simulations. We reveal that both theories are not adequate to explain the linear relationships. Therefore, we suggest another analytical model, which shows a possibility that a graded modulus can cause the linear force-indentation depth relationship. Two grading functions, the power law and the error function, are examined using the finite-element simulations, and we obtain force-indentation depth relationships very close to the linearity using the error function. An interactive method to determine the characteristic of a modified layer on PDMS is introduced using the results of the indentation with the error function and wavenumbers versus modulus ratios obtained in Chapter II. Due to the unrealistically high modulus ratio obtained from the iterative method, the effect of residual strains is considered. Higher residual strains cause lower modulus ratio.

From the experiment to produce wrinkles in a surface-modified layer of PDMS, a discrepancy in the wavelengths is observed according to the loading methods (tensile and compressive loadings). To explore the causes of the discrepancy, an analytical model is suggested. Poisson's ratio mismatch, the effect of crack opening, and the effect of graded modulus are examined using suggested model. Poisson's ratio mismatch is not enough to explain the discrepancy in a bi-layer structure. With the assumption of the crack opening, we obtain the possibility that causes the discrepancy at certain critical strain even lower than the theoretical limit (*i.e.* the ratio of the critical strain is less than the theoretical limit while the ratio of the wavelengths is same). When the error function with the crack opening model is used, the wavelength ratios increase and the critical strain ratios decreased. While we obtain the evident of the discrepancy from suggested models, quantitative estimation is not able to be obtained.

## 5.2 Future Work

In Chapter III, we found that the change of modulus at modified surface is very sensitive to the residual strains. If we find a sophisticated method to determine the residual strains experimentally or theoretically, we may obtain more realistic value of the modulus. This method should deal with both tensile and compressive residual strains. Therefore, the implementation of the method to determine the residual strain may do important role in the study of indentation in future.

Though we find several evidences that the modulus in the modified layer is graded, the investigation of the bi-layer assumption may still have importance in this research. In Chapter IV, we assume that the crack opening occurs only in the film for a bi-layer system. Thus, we can't find the stress field when the crack depth is larger than the thickness of film layer. Even though the effect of crack depth is not significant on the wavelengths, it deserves careful study.

## APPENDIX A

### AN AUTOMATED PROCEDURE FOR DETERMINING ASYMPTOTIC ELASTIC STRESS FIELDS AT SINGULAR POINTS

#### A.1 INTRODUCTION

Singular stress fields are generally developed in elastic bodies at re-entrant corners (sharp notches and cracks) and at the end points of discontinuous interfaces between dissimilar bodies. Some typical examples are shown in FigureA.1. Williams (1952) pioneered the technique of asymptotic analysis in which the local stress field is expanded as a series, each term of which has power-law dependence on  $r$ , where  $(r, \theta)$  is a system of polar coordinates based on the singular point. As the singular point is approached, the field will be increasingly dominated by the leading term in this series — *i.e.* the term for which the power-law exponent is smallest (or has the smallest real part). Thus, if failure is determined by behaviour in a small region near the singular point, it will be characterized simply by the coefficient of this most singular term (Dunn, 2003). In the case of a crack, this coefficient is the familiar stress intensity factor, which forms the basis of linear elastic fracture mechanics (LEFM). Similar arguments have been used to predict local failure in other situations involving theoretically singular elastic fields, such as a notch (Leguillon, 2002; Lazzarin *et al.*, 2003) or fretting fatigue at a sharp corner (Giannakopoulos *et al.*,

1998; Churchman *et al.*, 2003).

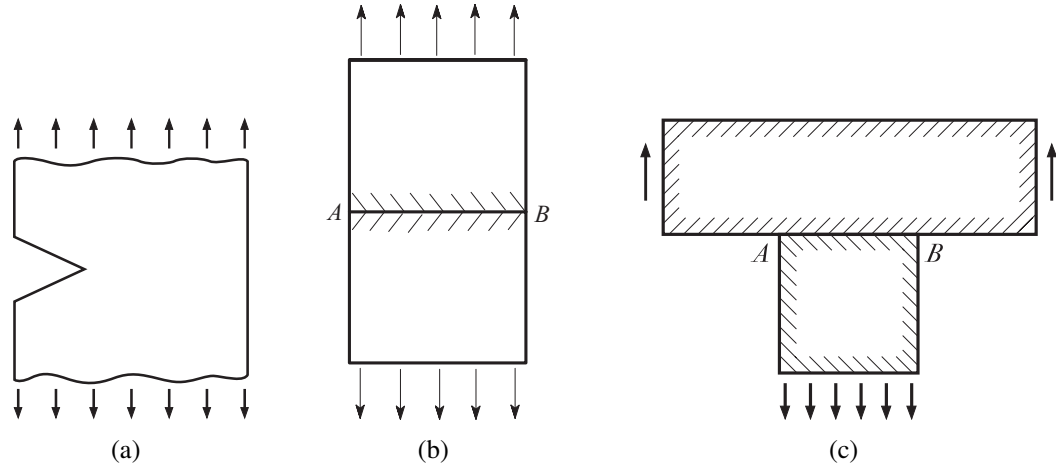


Figure A.1: Elastic structures involving singular points.

Knowledge of the nature of the singular field is also important in numerical (typically finite element) solutions of elasticity problems involving singular points (Sinclair *et al.*, 2002). Conventionally, a highly refined mesh will be used in such regions in the hope of capturing the nature of the local field, but this approach is extremely computer-intensive and even then may fail to converge with increasing mesh refinement, thus compromising the entire numerical solution. The most efficient way to solve such problems is to define a special element to model the region immediately surrounding the singular point (Seweryn, 2002). The shape function used in this element can then be chosen to conform with that of the dominant singular term in the appropriate asymptotic expansion. Special elements for crack tips in homogeneous materials are now included in all the major commercial finite element codes and several authors have developed and used special elements in other situations involving singular points (Lin and Tong, 1980; Chen and Sze, 2001; Tur *et al.*, 2002; Liu and Huang, 2003).

Results for the asymptotic fields in a variety of special cases have been published. Bogy (1968) investigated the case of bonded dissimilar wedges and in a discussion to this

paper Dundurs (1969) demonstrated that a more efficient statement of the solution could be made in terms of the now well known ‘Dundurs’ parameters’. Further results for this system were then given by Bogy (1971) and Bogy and Wang (1971). The asymptotic field at the corner of a sharp body indenting an elastic half plane was investigated by Dundurs and Lee (1972) for the frictionless case and the corresponding frictional problem was considered by Gdoutos and Theocaris (1975) and Comninou (1976). It should be noted that apart from Williams’ results which can be presented in a convenient graphical form, it is far from easy to use these published results to determine the power law exponent, since the authors generally use an inverse method to obtain their results.

The general technique of asymptotic analysis at a singular point is now a well established branch of elasticity (Barber, 2002, §11.2), but the algebraic calculations can be tedious and time consuming and are usually a distraction from main purpose of the investigation for which they are required. For this reason, many investigators simply use conventional elements with mesh refinement at singular points, often even without the backup of an appropriate convergence test. In the present paper, we introduce an automated procedure for solving the asymptotic eigenvalue problem for a fairly general class of singular point, using the software code MATLAB<sup>TM</sup>. Potential users merely need to specify the geometrical description of the singular point and the appropriate material properties and boundary conditions. The program then solves the eigenvalue problem, determining the strength of the dominant singular term and the form of the stress and displacement fields in the dominant region.

## A.2 SOLUTION METHOD

We first define a set of polar co-ordinates centered on the singular point and then focus on a region extremely close to the origin, which is equivalent to looking at the singular point through a very strong microscope. In this view, all the other geometric features of the component appear to be far distant from the origin and any curved boundaries in the field of vision will appear straight because their radii of curvature will have been indefinitely magnified. The local elasticity problem therefore reduces to that of one or more semi-infinite wedges with appropriate boundary conditions at the terminal edges  $\theta = \alpha_1, \theta = \alpha_2$  and at the interface(s)  $\theta = \beta_1, \theta = \beta_2, \dots$  (if any) between adjacent wedges. We shall refer to this as the *asymptotic problem*.

### A.2.1 Boundary and interface conditions

The only finite boundaries in the asymptotic problem comprise the two edges  $\theta = \alpha_1, \theta = \alpha_2$ . At an edge  $\theta = \alpha$ , the boundary conditions might take any one of the following forms :-

**B:(i) Traction-free:**

$$\sigma_{\theta r}(r, \alpha) = 0 ; \quad \sigma_{\theta \theta}(r, \alpha) = 0 ; \quad (\text{A.1})$$

**B:(ii) Bonded to a rigid body:**

$$u_r(r, \alpha) = 0 ; \quad u_\theta(r, \alpha) = 0 ; \quad (\text{A.2})$$

**B:(iii) Frictionless contact with a rigid body:**

$$\sigma_{\theta r}(r, \alpha) = 0 ; \quad u_\theta(r, \alpha) = 0 ; \quad (\text{A.3})$$

**B:(iv) Frictional contact with a rigid body**

$$\sigma_{\theta r}(r, \alpha) \pm f\sigma_{\theta\theta} = 0 ; \quad u_{\theta}(r, \alpha) = 0 , \quad (\text{A.4})$$

where the sign in the first equation depends on the assumed direction of slip.

At an interface  $\theta = \beta$  between the  $j$ th and  $(j + 1)$ th wedges, equilibrium conditions demand that

$$\sigma_{\theta r}^j(r, \beta) - \sigma_{\theta r}^{(j+1)}(r, \beta) = 0 ; \quad \sigma_{\theta\theta}^j(r, \beta) - \sigma_{\theta\theta}^{(j+1)}(r, \beta) = 0 . \quad (\text{A.5})$$

In addition, depending on the status of the interface, we have the additional conditions

**I:(i) Bonded interface:**

$$u_r^j(r, \alpha) - u_r^{(j+1)}(r, \alpha) = 0 ; \quad u_{\theta}^j(r, \alpha) - u_{\theta}^{(j+1)}(r, \alpha) = 0 ; \quad (\text{A.6})$$

**I:(ii) Frictionless contact:**

$$\sigma_{\theta r}^j(r, \beta) = 0 ; \quad u_{\theta}^j(r, \alpha) - u_{\theta}^{(j+1)}(r, \alpha) = 0 ; \quad (\text{A.7})$$

**I:(iii) Frictional contact**

$$\sigma_{\theta r}^j(r, \beta) \pm f\sigma_{\theta\theta}^j(r, \beta) = 0 ; \quad u_{\theta}^j(r, \alpha) - u_{\theta}^{(j+1)}(r, \alpha) = 0 , \quad (\text{A.8})$$

where the sign in the first equation depends on the assumed direction of slip.

At the most general singular point, there will be  $n$  wedges,  $n - 1$  interfaces and two edges, in which case the appropriate choice from equations (A.1–A.8) defines  $4n$  homogeneous conditions that must be satisfied by the stress fields in the wedges.

By way of illustration, Figure A.2 shows the asymptotic problem corresponding to the singular point  $A$  in Figure 1.1(c). There are two wedges of dissimilar materials occupying

the regions  $-\pi/2 < \theta < 0$  and  $0 < \theta < \pi$  respectively. There are two traction-free boundaries (Eq. (A.1)) corresponding to  $\alpha_1 = -\pi/2$  and  $\alpha_2 = \pi$  and one bonded interface (Eq. (A.6))  $\beta = 0$ .

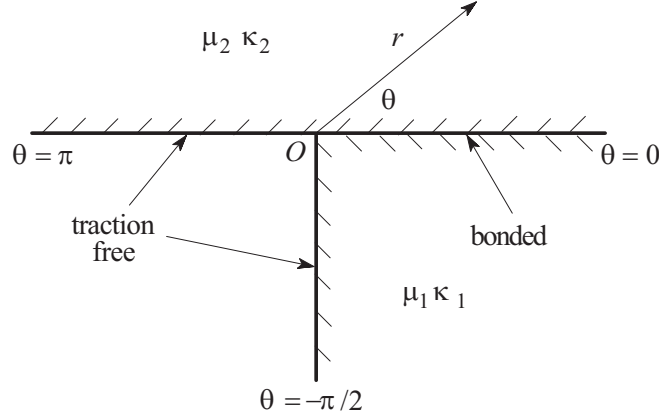


Figure A.2: Asymptotic problem corresponding to the point A in Figure 1.1(c).

### A.2.2 Asymptotic expansion

The asymptotic problem is self-similar (there is no inherent length scale) and the boundary and interface conditions are all homogeneous. We therefore seek particular solutions to the governing equations of elasticity in which the displacement fields have the separated-variable form

$$\mathbf{u} = r^\lambda \mathbf{f}(\theta) \quad (\text{A.9})$$

The most general solution of this kind in the wedge  $j$  is conveniently expressed in terms of the Airy stress function (Barber, 2002, §11.2),

$$\begin{aligned} \phi = r^{\lambda+1} \{ & A_j \cos(\lambda + 1)\theta + B_j \cos(\lambda - 1)\theta \\ & + C_j \sin(\lambda + 1)\theta + D_j \sin(\lambda - 1)\theta \} \end{aligned} \quad (\text{A.10})$$

corresponding to the stress and displacement components

$$\begin{aligned}\sigma_{rr} = & r^{\lambda-1}\{-A_j\lambda(\lambda+1)\cos(\lambda+1)\theta - B_j\lambda(\lambda-3)\cos(\lambda-1)\theta \\ & -C_j\lambda(\lambda+1)\sin(\lambda+1)\theta - D_j\lambda(\lambda-3)\sin(\lambda-1)\theta\}\end{aligned}\quad (\text{A.11})$$

$$\begin{aligned}\sigma_{r\theta} = & r^{\lambda-1}\{A_j\lambda(\lambda+1)\sin(\lambda+1)\theta + B_j\lambda(\lambda-1)\sin(\lambda-1)\theta \\ & -C_j\lambda(\lambda+1)\cos(\lambda+1)\theta - D_j\lambda(\lambda-1)\cos(\lambda-1)\theta\}\end{aligned}\quad (\text{A.12})$$

$$\begin{aligned}\sigma_{\theta\theta} = & r^{\lambda-1}\{A_j\lambda(\lambda+1)\cos(\lambda+1)\theta + B_j\lambda(\lambda+1)\cos(\lambda-1)\theta \\ & +C_j\lambda(\lambda+1)\sin(\lambda+1)\theta + D_j\lambda(\lambda+1)\sin(\lambda-1)\theta\}\end{aligned}\quad (\text{A.13})$$

$$\begin{aligned}2\mu_j u_r = & r^\lambda\{-A_j(\lambda+1)\cos(\lambda+1)\theta + B_j(\kappa_j - \lambda)\cos(\lambda-1)\theta \\ & -C_j(\lambda+1)\sin(\lambda+1)\theta + D_j(\kappa_j - \lambda)\sin(\lambda-1)\theta\}\end{aligned}\quad (\text{A.14})$$

$$\begin{aligned}2\mu_j u_\theta = & r^\lambda\{A_j(\lambda+1)\sin(\lambda+1)\theta + B_j(\kappa_j + \lambda)\sin(\lambda-1)\theta \\ & -C_j(\lambda+1)\cos(\lambda+1)\theta - D_j(\kappa_j + \lambda)\cos(\lambda-1)\theta\}\end{aligned}\quad (\text{A.15})$$

where  $A_j, B_j, C_j, D_j$  are arbitrary constants,  $\mu_j$  is the shear modulus and  $\kappa_j$  is Kolosov's constant equal to  $3 - 4\nu_j$  in plane strain and  $(3 - \nu_j)/(1 + \nu_j)$  in plane stress, with  $\nu_j$  being Poisson's ratio.

Substitution of these results into the appropriate boundary and interface conditions (A.1–A.8) will yield  $4n$  homogeneous linear algebraic equations for the  $4n$  unknowns  $A_j, B_j, C_j, D_j$ . For most values of  $\lambda$ , these equations will have only the trivial solution  $A_j = B_j = C_j = D_j = 0$ , but non-trivial solutions are obtained for a denumerably infinite set of *eigenvalues*  $\lambda_i$  at which the algebraic equations are not linearly independent. These eigenvalues are the solutions of the *characteristic equation* obtained by setting the determinant of the coefficients of the algebraic equations to zero. Depending on the conditions at the singular point, the eigenvalues  $\lambda_i$  may be real or complex.

### A.2.3 The eigenfunctions

For each eigenvalue  $\lambda_i$ , there is an associated eigenfunction which can be found by eliminating the redundant equation from the set and solving for  $4n - 1$  of the constants in terms of the remaining constant. Substitution into equations (A.10–A.15) then defines a non-trivial particular solution to the asymptotic problem of the form

$$\mathbf{u} = K_i r^{\lambda_i} \mathbf{f}_i(\theta) \quad (\text{A.16})$$

where  $K_i$  is the one remaining undetermined multiplying constant. A more general solution to the asymptotic problem can then be written down in the form of the eigenfunction expansion

$$\mathbf{u} = \sum_{i=1}^{\infty} K_i r^{\lambda_i} \mathbf{f}_i(\theta) \quad (\text{A.17})$$

Gregory (1979) has shown that this expansion is complete for the problem of the single wedge loaded only on the circular boundary  $r = a$ . It must also therefore be complete for the local field at a traction-free notch in an arbitrarily shaped body, since the imaginary boundary  $r = a$  in that body must transmit a unique set of tractions. To the best knowledge of the present authors, rigorous completeness proofs are not available for more general singular points, but it seems likely that this representation has general validity.

If the strain energy in the body is to be bounded, all the eigenvalues must satisfy the condition  $\Re(\lambda_i) > 0$  (Barber, 2002, §11.2) and if they are ranked in order of increasing real part, the stress field in the immediate vicinity of the singular point will be dominated by the first term  $K_0 r^{\lambda_0} \mathbf{f}_0(\theta)$ . This term will define a singular field if and only if  $0 < \Re(\lambda_0) < 1$ .

### A.3 THE ANALYTICAL TOOL

This procedure has been automated, using the software code MATLAB<sup>TM</sup> v7.1 with the MATLAB GUI development environment (GUIDE) v2.5 and the MATLAB Symbolic Toolbox v3.1. The analytical tool provides a graphic interface in which users can define their problem, determine the order of the corresponding singularity and generate the distribution of stress and displacement. Final results are provided in both text and graphic format.

Figure A.3 shows a schematic of the steps involved in the solution. Users specify the geometry of the singular point through the angles  $\alpha_1, \alpha_2$  defining the edges, and the angles  $\beta_1, \beta_2, \dots$  defining the interfaces between regions (wedges) of different materials, if any. They also specify the material properties  $\mu_j, \nu_j$  of the various regions and whether conditions are plane strain or plane stress. Finally, for each edge or interface, they select one of the qualitative states itemized in Section A.2.1.

Using this input, the analytical tool constructs the corresponding system of algebraic equations and hence determines the characteristic equation by evaluating the determinant of coefficients. It then attempts to solve this equation to evaluate the first few eigenvalues, using Maple<sup>TM</sup> (which is included as a solver within MATLAB). If the characteristic equation system is too complicated for Maple to solve, the user is prompted to use Newton's method to obtain an iterative solution. Since the characteristic equation has many solutions, the result of this iterative procedure is sensitive to the choice of initial guess, so a visual root finder is provided in order that the user can make a selection of an appropriate initial guess. This procedure is explained in Section A.3.3 below.

Once the lowest eigenvalue has been determined, the corresponding eigenfunction is

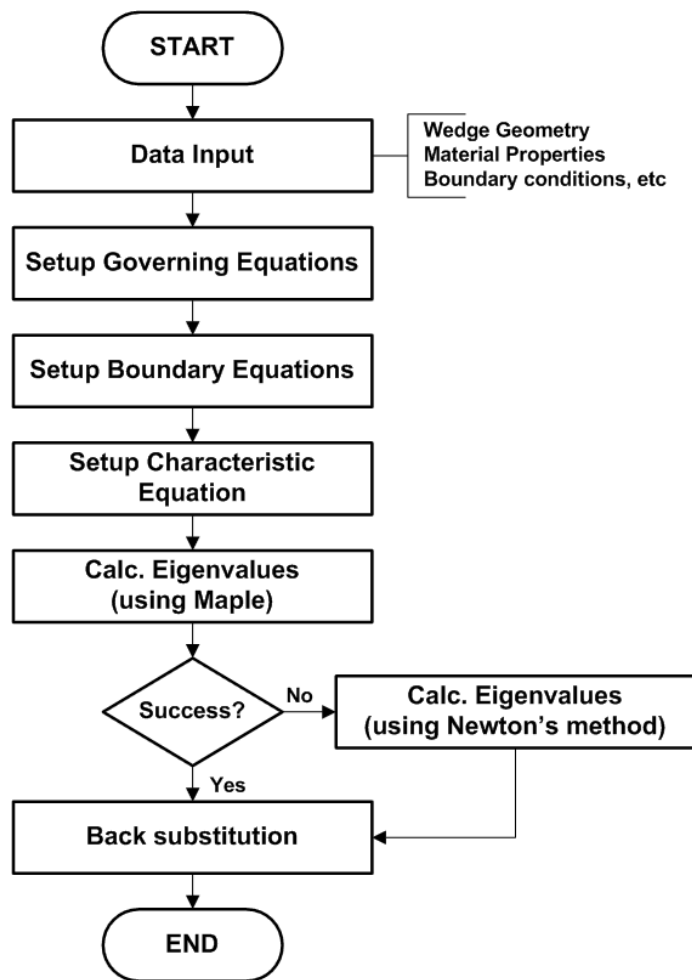


Figure A.3: Flow chart for the automated eigenvalue solver.

obtained by the back substitution procedure of Section A.2.3. Features of the corresponding stress or displacement field can then be displayed as contour plots.

### A.3.1 Data input

Figure A.4 shows the graphic interface representing the appropriate geometry for the asymptotic problem of Figure A.2. On starting the program, the user is presented with a blank screen of this form, in which they first select plane stress and plane strain as appropriate. Clicking on ‘Add Wedge’ opens an input window for the first wedge as shown in Figure A.5. For the present example, we would select  $-\pi/2$  and 0 to define the wedge angles and then input the appropriate material properties for material 1. If the box ‘use Loading Condition’ is clicked, Kolosov’s constant  $\kappa$  will be calculated from  $\nu$  based on the previously specified loading condition. Alternatively, if this box is not checked,  $\kappa$  can be input as an independent variable.

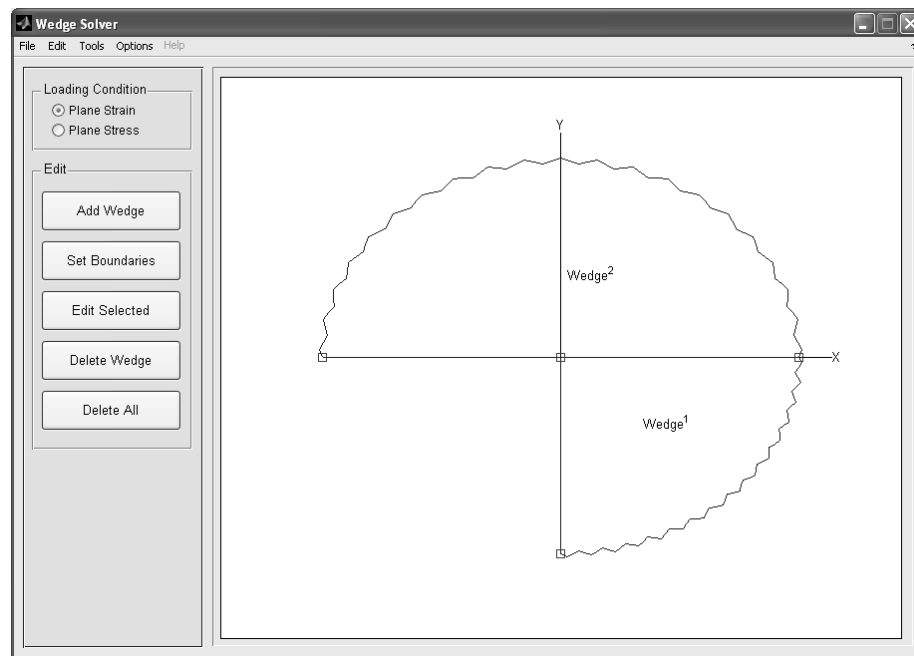


Figure A.4: Geometry of the asymptotic problem of Figure A.2.

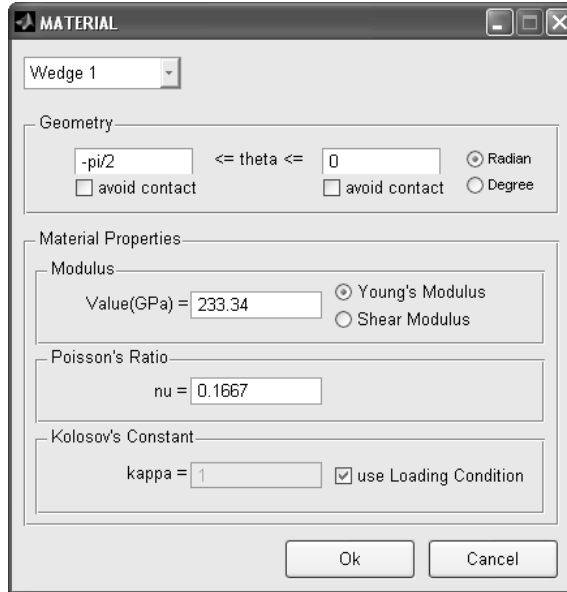


Figure A.5: Input window for the first wedge.

Clicking on ‘Ok’ returns the user to the geometry window, in which the first wedge will now be correctly identified. To add the second wedge, we once again click on ‘Add Wedge’, enter the angles  $0$  and  $\pi$  and the properties of material 2, which will then return to the geometry window in the form shown in Figure A.4.

There is no limitation on the number of wedges that can be entered into the problem statement using this procedure, but the algebraic complexity of multi-wedge problems may place practical limits, depending on the available hardware resources such as processor and memory capacity.

### A.3.2 Boundary and interface conditions

Once the geometry of the problem is completely specified, the next step is to identify the conditions at the boundaries and interfaces, by selecting between the choices in Section A.2.1. The first step is to click on the button ‘Set Boundaries’ in Figure A.4, leading to the screen of Figure A.6, in which all the boundaries and interfaces are identified and

sequentially numbered. The default option is to identify radial lines shared by two wedges as interfaces. The user can override this assumption by checking the box ‘Avoid Contact’ for the appropriate edge in the wedge input window of Figure A.5. The user next highlights one of the boundaries using the mouse and clicks on ‘Edit Selected’. This opens a data input window, which in the case of a boundary offers the choice of the boundary conditions B(i)–B(iv) of §2.1, as shown in Figure A.7. If ‘Frictional Contact with a Rigid Body’ is selected, the coefficient of friction  $f$  must also be input. Notice that  $f$  may take either sign depending on the direction of slip anticipated at the singular point. In general, different singular fields are obtained for different directions of slip. If an interface is highlighted at the stage, the corresponding data input window offers the choices I(i)–I(iii) of Section A.2.1.

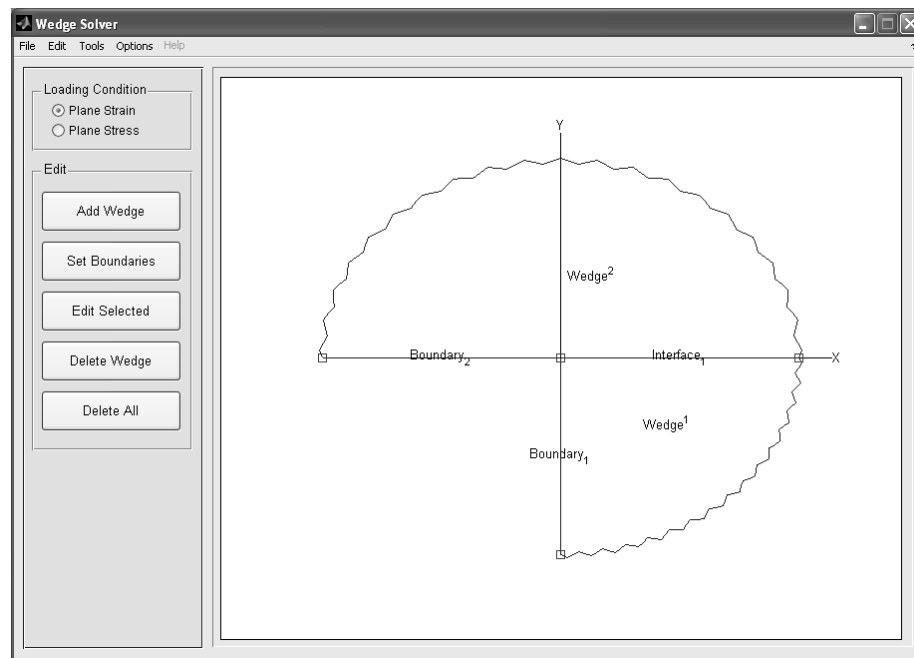


Figure A.6: Geometry of the problem with boundaries and interfaces identified.

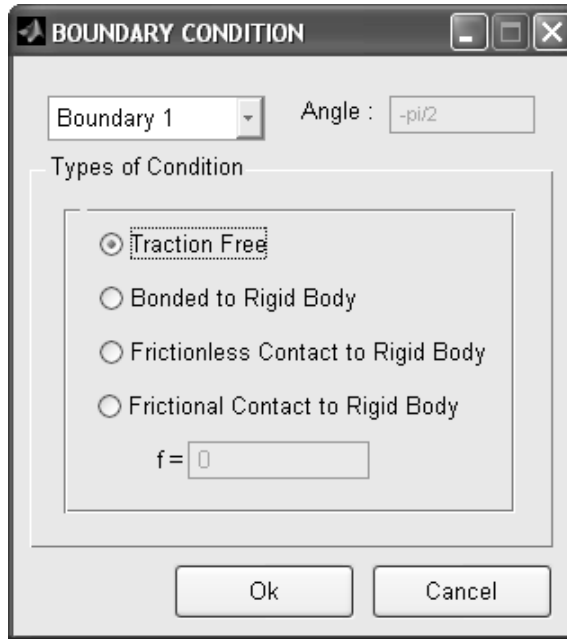


Figure A.7: Data input window for Boundary 1 from Figure A.6.

### A.3.3 Solving process

To start the solution of the eigenvalue problem, the user clicks on 'Tools→Run' in the toolbar of Figure A.6. During the solution, a message window is shown on the screen to inform the user of the progress of the solution. Once the characteristic equation has been constructed, the tool will attempt to solve it using Maple. However, sometimes this is unsuccessful and an iterative numerical solution is necessary, using Newton's method. The success of this method depends on the choice of initial guess. To increase reliability, the user is prompted to select an appropriate initial value by the root finding screen shown in Figure A.8.

This Figure shows the loci of the equations  $\Re\{\mathcal{C}(\lambda)\} = 0$  (thick lines) and  $\Im\{\mathcal{C}(\lambda)\} = 0$  (thin lines), where  $\mathcal{C}(\lambda) = 0$  is the characteristic equation. The loci are plotted in the complex plane for  $\lambda$ , so that real eigenvalues (if any) appear on the real axis. Both these equations must be satisfied, so permissible eigenvalues correspond to the intersection of

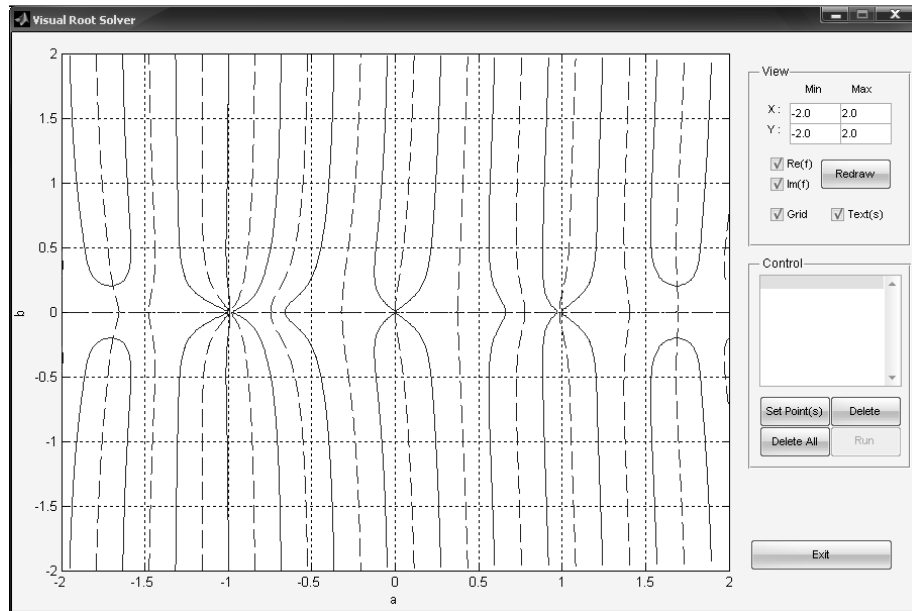


Figure A.8: The visual root finder.

a pair of thick and thin lines. To select a point near to the required intersection, the user clicks on the ‘Set Point(s)’ button in Figure A.8 and then moves the mouse to click on the appropriate intersection. The coordinates of the point selected are displayed in the box at the bottom right of the screen. More than one point may be selected if desired, in which case all the resulting eigenvalues will be returned. Once the initial value has been identified, the user clicks on the right mouse button and then on ‘Exit’ which closes this screen and returns to the solving process.

#### A.3.4 Presentation of results

Once the solution process is complete, the tool returns a ‘Results’ screen from which the user can select to display the governing equations, the equations derived from the boundary and interface conditions, the characteristic equation and the eigenvalue(s). Selection of the options in the ‘Results of Back Substitution’ frame provides a text descrip-

tion of the equations defining the eigenfunction field for stress or displacement components associated with the eigenvalue with smallest real part and a contour plot of the same fields.

## A.4 VALIDATION

To demonstrate the usefulness of the tool and to evaluate its robustness, we tested it by comparison with the results for (i) the single wedge solution of Williams (1952), (ii) the bonded dissimilar wedge problem of Bogy (1971) and (iii) the frictional contact problem of Gdoutos and Theocaris (1975). In each case, the lowest eigenvalues obtained agreed exactly with those given by the original authors (including the imaginary part of the eigenvalue in cases where this is complex).

For example, we used the tool to determine the eigenvalues for the system of Figure A.2. Following Bogy (1971), we present the results in Figure A.9 as a contour plot of the real and imaginary parts of the dominant eigenvalue as functions of the Dundurs' parameters.

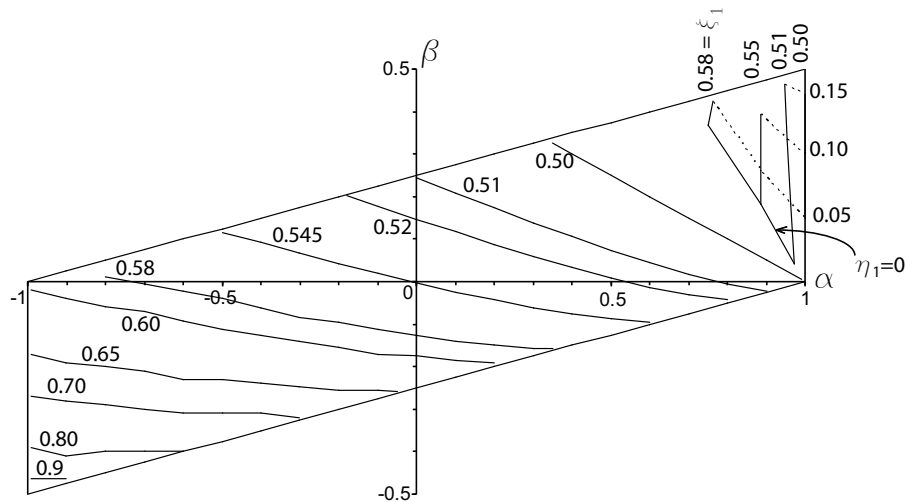


Figure A.9: Contour plot of eigenvalues for the problem of Figure A.2.

## A.5 CONCLUSIONS

We have developed an analytical tool within MATLAB for solving the asymptotic problem for a fairly general class of singular point in linear elasticity. The tool does not require any specialist knowledge of asymptotic analysis and it provides as output the power of the dominant singular term (the eigenfunction) and the form of the resulting stress and displacement fields. The tool has been tested against previously published asymptotic solutions and in all cases it gives reliable and accurate results. It should also be remarked that most of these previous solutions resort to an inverse method for determining the eigenvalues. In other words, they specify the eigenvalue and solve for the corresponding material properties. The present solution is direct, which is more likely to be useful in particular applications. The results are potentially useful for the development of special finite elements or other efficient numerical strategies for problems involving singular points. The source code is given in the Appendix, or alternatively it can be downloaded from the website <http://www-personal.engin.umich.edu/~jbarber/asymptotics/intro.html>

## BIBLIOGRAPHY

- [1] H. G. Allen. *Analysis and Design of Structural Sandwich Panels*. Pergamon, New York, 1969.
- [2] J. R. Anderson, D. T. Chiu, R. J. Jackman, O. Cherniavskaya, J. C. McDonald, H. Wu, S. H. Whitesides, and G. M. Whitesides. Fabrication of topologically complex three-dimensional microfluidics systems in pdms by rapid prototyping. *Anal. Chem.*, 72:3158–3164, 2000.
- [3] G. Bar, L. Delineau, A. Hafele, and M. . Whangbo. Investigation of the stiffness change in, the indentation force and the hydrophobic recovery of plasma-oxidized polydimethylsiloxane surfaces by tapping mode atomic force microscopy. *Polymer*, 42:3527–3632, 2001.
- [4] J. R. Barber. *Elasticity*. Elasticity. Kluwer, Dordrecht, 2nd edition, 2002.
- [5] A. K. Bhattacharya and W. D. Nix. Analysis of elastic and plastic deformation associated with indentation testing of thin films on substrates. *International Journal of Solids and Structures*, 24(12):1287, 1988.
- [6] A. K. Bhattacharya and W. D. Nix. Finite element simulation of indentation experiments. *International Journal of Solids and Structures*, 24(9):881, 1988.
- [7] M. A. Biot. Bending of an infinite beam on an elastic foundation. *Journal of Applied Mechanics*, 4:A-1–A-7, 1937.
- [8] P. Bodö and J. . Sundgren. Titanium deposition onto ion-bombarded and plasma-treated polydimethylsiloxane: Surface modification, interface and adhesion. *Thin Solid Films*, 136(1):147, 1986.
- [9] D. B. Bogy. Edge-bonded dissimilar orthogonal elastic wedges under normal and shear loading. *ASME J.Appl.Mech.*, 35:460–466, 1968.
- [10] D. B. Bogy. Two edge-bonded elastic wedges of different materials and wedge angles under surface tractions. *ASME*, 38:377–386, 1971.
- [11] D. B. Bogy and K. C. Wang. Stress singularities at interface corners in bonded dissimilar isotropic elastic materials. *Int.J.Solids Structures*, 7:993–1005, 1971.

- [12] A. Bolshakov, W. C. Oliver, and G. M. Pharr. Influences of stress on the measurement of mechanical properties using nanoindentation: Part ii. finite element simulations. *J. Mater. Res.*, 11(3):760–768, 1996.
- [13] J. Boussinesq. *Application des Potentials, a l'Etude de L'Equilibre et du Mouvement des Solids Elastiques*. Gauthier-Villars, Paris, 1885.
- [14] N. Bowden, S. Brittain, A. G. Evans, J. W. Hutchinson, and G. M. Whitesides. Spontaneous formation of ordered structures in thin films of metals supported on an elastomeric polymer. *Nature*, 393:146–149, 1998.
- [15] N. Bowden, W. T. S. Huck, K. E. Paul, and G. M. Whitesides. The controlled formation of ordered, sinusoidal structures by plasma oxidation of an elastomeric polymer. *Applied Physics Letters*, 75(17):2557, 1999.
- [16] C. Brun, P. Delobelle, M. Fromm, F. Berger, A. Chambaudet, and F. Jaffiol. Mechanical properties determined by nanoindentation tests of polypropylene modified by  $he^+$  particle implantation. *Materials Science and Engineering A*, 315:63–69, 2001.
- [17] B. Budiansky. Theory of buckling and postbuckling behavior of elastic structures. *Adv. Appl. Mech.*, 14:1–65, 1974.
- [18] D. M. Burmister. The general theory of stresses and displacements in layered soil systems. ii. *Journal of Applied Physics*, 16(3):126, 1945.
- [19] D. M. Burmister. The general theory of stresses and displacements in layered soil systems. iii. *Journal of Applied Physics*, 16(5):296, 1945.
- [20] D. M. Burmister. The general theory of stresses and displacements in layered systems. i. *Journal of Applied Physics*, 16(2):89, 1945.
- [21] C. R. Calladine and J. A. Greenwood. Line and point loads on a non-homogeneous incompressible elastic half-space. *Q.J. Mech. appl. Math.*, xxxi(4):507–529, 1978.
- [22] H. Carslaw and J. C. Jaeger. *The Conduction of Heat in Solids*. Clarendon Press, Oxford, second ed. edition, 1959.
- [23] E. Cerda and L. Mahadevan. Geometry and physics of wrinkling. *Physical Review Letters*, 90(7):074302, 02/19/ 2003.
- [24] M-C Chen and K. Y. Sze. A novel finite element analysis of bimaterial wedge problems. *Eng.Fract.Mech.*, 68:1463–1476, 2001.
- [25] W. Chen and P. Engel. Impact and contact stress analysis in multilayer media. *International Journal of Solids and Structures*, 8(11):1257, 1972.
- [26] X. Chen and J. W. Hutchinson. Herringbone buckling patterns of compressed thin films on compliant substrates. *Journal of Applied Mechanics*, 71(5):597–603, 2004.

- [27] X. Chen and J. J. Vlassak. Numerical study on the measurement of thin film mechanical properties by means of nanoindentation. *J. Mater. Res.*, 16(10):2974–2982, 2001.
- [28] A. T. Chien, T. Felter, J. D. LeMay, and M. Balooch. Nanoscale mechanical properties of polymer composites: Changes in elastic modulus and measurement of ion penetration depth due to  $\alpha$ -radiation. *J. Mater. Res.*, 15(4):838–841, 2000.
- [29] S. Chowdhury and M. T. Laugier. Non-contact afm with a nanoindentation technique for measuring the mechanical properties of thin films. *Nanotechnology*, 15:1017–1022, 2004.
- [30] D. B. H. Chua, H. T. Ng, and S. F. Y. Li. Spontaneous formation of complex and ordered structures on oxygen-plasma-treated elastomeric polydimethylsiloxane. *Applied Physics Letters*, 76(6):721–723, February 7, 2000 2000.
- [31] C. Churchman, A. Mugadu, and D. A. Hills. Asymptotic results for slipping complete frictional contacts. *ur.J.Mech A/Solids*, 22:793–800, 2003.
- [32] M. Comninou. Stress singularity at a sharp edge in contact problems with friction. *Z.angew.Math.Physz.*, 27:493–499, 1976.
- [33] W. J. Cousins, R. W. Armstrong, and W. H. Robinson. Young’s modulus of lignin from a continuous indentation test. *J. Mat. Sci.*, 10:1655–1658, 1975.
- [34] M. F. Doerner and W. D. Nix. A method for interpreting the data from depth-sensing indentation instruments. *Journal of Materials Research*, 1(4):601–609, 1986.
- [35] J. Dundurs. Discussion on edge bonded dissimilar orthogonal elastic wedges under normal and shear loading. *ASME J.Appl.Mech.*, 36:650–652, 1969.
- [36] J. Dundurs and M. S. Lee. Stress concentration at a sharp edge in contact problems. *J. Elasticity*, 2:109–112, 1972.
- [37] M. L. Dunn. Fracture initiation at geometric and material discontinuities: Criteria based on critical stress intensities of linear elasticity. *Chinese J Mech A*, 19:15–29, 2003.
- [38] K. Efimenko, M. Rackaitis, E. Manias, A. Vaziri, L. Mahadevan, and J. Genzer. Nested self-similar wrinkling patterns in skins. *Nature materials*, 4(4):293–297, Apr 2005.
- [39] K. Efimenko, W. E. Wallace, and J. Genzer. Surface modification of sylgard-184 poly(dimethyl siloxane) networks by ultraviolet and ultraviolet/ozone treatment. *Journal of Colloid and Interface Science*, 254(2):306–315, 10/15 2002.
- [40] A. W. Feinberg and A. B. Brennan. Effect of argon plasma treatment on pdms elastomer investigated by afm., 2003.

- [41] T. Fujii. Pdms-based microfluidic devices for biomedical applications. *Microelectronic Engineering*, 61-62(1-3):907–914, 2002.
- [42] E. E. Gdoutos and P. S. Theocaris. Stress concentrations at the apex of a plane indenter acting on an elastic half plane. *ASME J.Appl.Mech.*, 42:688–692, 1975.
- [43] J. Genzer and J. Groenewold. Soft matter with hard skin: From skin wrinkles to templating and material characterization. *Soft Matter*, 2(4):310–323, 2006.
- [44] A. E. Giannakopoulos, P. Larsson, and R. Vestergaard. Analysis of vickers indentation. *International Journal of Solids and Structures*, 31(19):2679–2708, 1994.
- [45] A. E. Giannakopoulos, T. C. Lindley, and S. Suresh. Aspects of equivalence between contact mechanics and fracturemechanics: theoretical connections and a life-prediction methodology for fretting-fatigue. *International Journal of Solids and Structures*, 46:2955–2968, 1998.
- [46] A. E. Giannakopoulos and S. Suresh. Indentation of solids with gradients in elastic properties: Part i. point force. *International Journal of Solids and Structures*, 34(19):2393–2428, 7 1997.
- [47] A. E. Giannakopoulos and S. Suresh. Indentation of solids with gradients in elastic properties: Part ii. axisymmetric indentors. *International Journal of Solids and Structures*, 34(19):2393, 1997.
- [48] R. D. Gregory. Green’s functions, bi-linear forms and completeness of the eigenfunctions for the elastostatic strip and wedge. *J.Elasticity*, 9:283–309, 1979.
- [49] Groenewold. Wrinkling of plates coupled with soft elastic media. *Physica A Statistical Mechanics and its Applications*, 298(1-2):32, 2001.
- [50] R. H. Hansen, J. V. Pascale, T. De Benedictis, and P. M. Rentzepis. Effect of atomic oxygen on polymers. *J. Polym. Sci. A*, 3(6):2205–2214, 1965.
- [51] C. Harrison, C. M. Stafford, W. Xhang, and A. Karim. Sinusoidal phase grating created by a tunably buckled surface. *App. Phy. Lett*, 85(18):4016–4018, 2004.
- [52] J. L. He and S. Veprek. Finite element modeling of indentation into superhard coatings. *Surface and Coatings Technology*, 163-164:374–379, 2003.
- [53] H. Hertz. Über die berührung fester elastischer köper. *J. reine und angewandle Mathematik*, 92:156–171, 1882. English translation in *Miscellaneous Papers by H. Hertz*, Eds. Jones and Schott, Macmilan, London, 1896.
- [54] H. Hillborg, J. F. Ankner, U. W. Gedde, G. D. Smith, H. K. Yasuda, and K. Wikstrm. Crosslinked polydimethylsiloxane exposed to oxygen plasma studied by neutron reflectometry and other surface specific techniques. *Polymer*, 41(18):6851–6863, 8 2000.

- [55] H. Hillborg and U. W. Gedde. Hydrophobicity recovery of polydimethylsiloxane after exposure to corona discharges. *Polymer*, 39(10):1991, 1998.
- [56] H. Hillborg and U. W. Gedde. Hydrophobicity changes in silicone rubbers. *IEEE Transactions on Dielectrics and Electrical Insulation*, 6(5):703–717, 1999.
- [57] H. Hillborg, N. Tomczak, A. Olah, H. Schonherr, and G. J. Vancso. Nanoscale hydrophobic recovery: A chemical force microscopy study of uv/ozone-treated cross-linked poly(dimethylsiloxane). *Langmuir*, 20(3):785–794, 2004.
- [58] J. R. Hollahan and G. L. Carlson. Hydroxylation of polymethylsiloxane surfaces by oxidizing plasmas. *J. Appl. Polym. Sci.*, 14(10):2499–2508, 1970.
- [59] X. Huang and A. Pelegri. Mechanical characterization of thin film materials with nanoindentation measurements and fe analysis. *Journal of Composite Materials*, 39(14):1261–1281, 2005.
- [60] Z. Huang, W. Hong, and Z. Suo. Evolution of wrinkles in hard films on soft substrates. *Physical Review E*, 70(3):030601–1–030601–4, 2004.
- [61] Z. Y. Huang, W. Hong, and Z. Suo. Nonlinear analyses of wrinkles in a film bonded to a compliant substrate. *Journal of the Mechanics and Physics of Solids*, 53(9):2101–2118, 2005.
- [62] W. T. S. Huck, N. Bowden, P. Onck, T. Pardoën, J. W. Hutchinson, and G. M. Whitesides. Ordering of spontaneously formed buckles on planar surfaces. *Langmuir*, 16:3497–3501, 2000.
- [63] B. H. Jo, L.M. val Lerberghe, K.L. Mootsegood, and D. J. Beebe. Three-dimensional micro-channel fabrication in polydimethylsiloxane (pdms) elastomer. *J. Microelectromechanical Sys.*, 9:76–81, 2000.
- [64] R. B. King. Elastic analysis of some punch problems for a layered medium. *International Journal of Solids and Structures*, 23(12):1657, 1987.
- [65] J. A. Knapp. Finite-element modeling of nanoindentation for determining the mechanical properties of implanted layers and thin films. *Nuclear Instruments and Methods in Physics Research Section B Beam Interactions with Materials and Atoms*, 127-128:935, 1997.
- [66] J. A. Knapp, D. M. Follstaedt, S. M. Myers, J. C. Barbour, T. A. Friedmann, J. W. Ager, O. R. Monteiro, and I. G. Brown. Finite-element modeling of nanoindentation for evaluating mechanical properties of mems materials. *Surface and Coatings Technology*, 103-104(1-2):268, 1998.
- [67] W. T. Koiter. On the stability of elastic equilibrium. *Delft University Thesis in Dutch, NASA Technical Translation in 1967*, TT F10:833, 1945.

- [68] K. Komvopoulos. Finite element analysis of a layered elastic solid in normal contact with a rigid surface. *Journal of Tribology*, 110:477–485, 1988.
- [69] E. R. Kral, K. Komvopoulos, and D. B. Bogy. Finite element analysis of repeated indentation of an elastic-plastic layered medium by a rigid sphere, part i: Surface results. *Journal of Applied Mechanics*, 62(1):20–28, 1995.
- [70] S. P. Lacour, J. Jones, Z. Suo, and S. Wagner. Design and performance of thin metal film interconnects for skin-like electronic circuits. *IEEE Electron Device Letters*, 25(4):179–181, 2004.
- [71] F. C. Larché and J. W. Cahn. The effect of self-stress on diffusion in solids. *Acta Metall.*, 30:1835–1845, 1982.
- [72] P. . Larsson and I. R. M. Peterson. Evaluation of sharp indentation testing of thin films and ribbons on hard substrates. *Journal of Testing and Evaluation*, 30(1):64–73, 2002.
- [73] T. A. Laursen and J. C. Simo. A study of the mechanics of microindentation using finite elements. *Journal of Materials Research*, 7(3):618–626, 1992.
- [74] P. Lazzarin, T. Lassen, and P. Livieri. A notch stress intensity approach applied to fatigue life predictions of welded joints with different local toe geometry. *Fatigue Fract Engng Matls Struct.*, 26:49–58, 2003.
- [75] D. Leguillon. Strength or toughness? a criterion for crack onset at a notch. *Eur.J.Mech A/Solids*, 21:61–72, 2002.
- [76] V. Lin and P. Tong. Singular finite elements for the fracture analysis of v-notched plate. *Int.J.Num.Meth.Eng.*, 15:1343–1354, 1980.
- [77] C. H. Liu and C. Huang. Oscillatory crack tip triangular elements for finite element analysis of interface cracks. *Int.J.Num.Meth.Eng.*, 58:1765–1783, 2003.
- [78] Y. . Loo, T. Someya, K. W. Baldwin, Z. Bao, P. Ho, A. Dodabalapur, H. E. Katz, and J. A. Rogers. Soft, conformable electrical contacts for organic semiconductors: High-resolution plastic circuits by lamination. *PNAS*, 99(16):10252–10256, 2002.
- [79] O. Lourie, D. M. Cox, and H. D. Wagner. Buckling and collapse of embedded carbon nanotubes. *Physical Review Letters*, 81(8):1638, 08/24/ 1998.
- [80] S. N. Magonov, V. Elings, and M. . Whangbo. Phase imaging and stiffness in tapping-mode atomic force microscopy. *Surface Science*, 375(2-3):L385–L391, 1997.
- [81] K. L. Mills, X. Zhu, S. Takayama, and M. D. Thouless. The mechanical properties of a surface-modified layer on poly(dimethylsiloxane). *JMR*, 2007.

- [82] M. W. Moon, S. H. Lee, J. Y. Sun, K. H. Oh, A. Vaziri, and J. W. Hutchinson. Wrinkled hard skins on polymers created by focused ion beam. *Proceedings of the National Academy of Sciences of the United States of America*, 104(4):1130–1133, Jan 23 2007.
- [83] M. Morra, E. Occhiello, R. Marola, F. Garbassi, P. Humphrey, and D. Johnson. On the aging of oxygen plasma-treated polydimethylsiloxane surfaces. *Journal of Colloid and Interface Science*, 137(1):11–24, 6 1990.
- [84] K. Niu and R. Talreja. Modeling of wrinkling in sandwich panels under compression. *Journal of Engineering Mechanics*, 125(8):875–883, 1999.
- [85] T. Ohzono and M. Shimomura. Ordering of microwrinkle patterns by compressive strain. *Physical Review B*, 69:133202–1–133202–4, 2004.
- [86] W. C. Oliver and G. M. Pharr. An improved technique for determining hardness and elastic modulus using load and displacement sensing indentation experiments. *Journal of Materials Research*, 7(6):1564, 1992.
- [87] V. P. Ol’shanskii. Green’s function for the bending of a plate on an elastic half-body. *PMM U.S.S.R*, 51(5):681–683, 1987.
- [88] M. Ouyang, C. Yuan, R. J. Muisener, A. Boulares, and J. T. Koberstein. Conversion of some siloxane polymers to silicon oxide by uv/ozone photochemical processes. *Chemistry of Materials*, 12(6):1591–1596, 2000.
- [89] J. B. Pethica, R. Hutchings, and W. C. Oliver. Hardness measurement at penetration depths as small as 20 nm. *Philosophical Magazine A*, 48(4):593, 1983.
- [90] W. H. Robinson and S. D. Truman. Stress-strain curve for aluminium from a continuous indentation test. *J. Mat. Sci.*, 12:1961–1965, 1977.
- [91] A. Seweryn. Modeling of singular stress fields using finite element method. *Int.J.Solids Struct.*, 39:4787–4804, 2002.
- [92] G. B. Sinclair, N. G. Cormier, J. H. Griffi, and G. Meda. Contact stresses in dovetail attachments: Finite element modeling. *ASME J.Eng.Gas Turb.Power*, 124:182–189, 2002.
- [93] I. N. Sneddon. The relation between load and penetration in the axisymmetric boussinesq problem for a punch of arbitrary profile. *Int. J. Engng Sci.*, 3:47–57, 1965.
- [94] C. M. Stafford, C. Harrison, K. L. Beers, A. Karim, E. J. Amis, M. R. VanLandingham, H. C. Kim, W. Volksen, R. D. Miller, and E. E. Simonyi. A buckling-based metrology for measuring the elastic moduli of polymeric thin films. *Nature materials*, 3(8):545–550, Aug 2004.

- [95] S. Suresh and A. E. Giannakopoulos. A new method for estimating residual stresses by instrumented sharp indentation. *Acta Materialia*, 46(16):5755–5767, 1998.
- [96] J. G. Swandener, B. Taljat, and G. M. Pharr. Measurement of residual stress by load and depth sensing indentation with spherical indenters. *J. Mater. Res.*, 16(7):2091–2102, 2001.
- [97] A. I. Teixeira, G. A. Abrams, P. J. Bertics, C. J. Murphy, and P. F. Nealey. Epithelial contact guidance on well-defined micro- and nanostructured substrates. *Journal of cell science*, 116(Pt 10):1881–1892, May 15 2003.
- [98] S. Timoshenko and S. Woinowsky-Krieger. *Theory of plates and shells*. McGraw-Hill, New York, second edition, 1959.
- [99] N. Triantafyllidis and R. Peek. On the stability and the worst imperfection shape in solids with nearly simultaneous eigenmodes. *Int. J. Solids Struct.*, 29:2281–2299, 1992.
- [100] T. Y. Tsui, W. C. Oliver, and G. M. Pharr. Influences of stress on the measurement of mechanical properties using nanoindentation: Part i. experiemental studies in an aluminum alloy. *J. Mater. Res.*, 11(3):752–759, 1996.
- [101] M. Tur, J. Fuenmayor, A. Mugadu, and D. A. Hills. On the analysis of singular stress fields, part 1: finite element formulation and application to notches. *J. Strain Anal.*, 37:437–444, 2002.
- [102] S. van der Zwaag and J. E. Field. Indentation and liquid impact studies on coated germanium. *Philos.Mag.A*, 48(5):767–777, 1983.
- [103] M. R. VanLandingham, S. H. McKnight, G. R. Palmese, R. F. Eduljee, J. W. Gillespie, and R. L. McCullough. Relating polymer indentation behavior to elastic modulus using atomic force microscopy. *J. Mat. Sci. Lett.*, 16:117–119, 1997.
- [104] R. P. Vinci and J. C. Bravman. Mechanical testing of thin films. *TRANSDUCERS '91: 1991 International Conference on Solid-State Sensors and Actuators. Digest of Technical Papers [0-87942-585-7]*, pages 943–948, 1991.
- [105] A. L. Volynskii, S. Bazhenov, O. V. Lebedeva, and N. F. Bakeev. Mechanical buckling instability of thin coatings deposited on soft polymer substrates. *Journal of Materials Science*, 35(3):547–554, 02/01/ 2000.
- [106] M. Watanabe. Striped-pattern formation of a thin gold film deposited onto a stretched elastic silicone substrate. *J Polym Sci Part B: Polym Phys*, 43:1532–1537, 2005.
- [107] E. A. Wilder, s. Guo, S. Lin-Gibson, M. J. Fasolka, and C. M. Stafford. Measuring the modulus of soft polymer networks via a buckling-based metrology (vol 39, pg 4138, 2006). *Macromolecules*, 39(17):5956, 2006.

- [108] M. L. Williams. Stress singularities from various boundary conditions in angular corners of plates in extension. *ASME J.Appl.Mech.*, 19:526–528, 1952.
- [109] J. Xu, J. Hooker, I. Adhietty, P. Padmanabhan, and W. Chen. Characterization of mechanical properties of thin polymer films using scanning probe microscopy. *Mat. Res. Soc. Symp. Proc.*, 552:217–223, 1998.
- [110] C. . Yeo and A. A. Polycarpou. A correction to the nanoindentation technique for ultrashallow indenting depths. *Journal of Materials Research*, 22(9):2359–2362, 2007.
- [111] P. J. You, K. Y. Suh, S. Y. Park, and H. H. Lee. Physical self-assembly of microstructures by anisotropic buckling. *Adv. Mater.*, 14(19):1383–1387, 2002.
- [112] X. Zhu, K. L. Mills, P. R. Peters, J. H. Bahng, E. H. Liu, J. Shim, K. Naruse, M. E. Csete, M. D. Thouless, and S. Takayama. Fabrication of reconfigurable protein matrices by cracking. *Nature materials*, 4(5):403–406, May 2005.